28 nm CMOS Array of Strips for Pedestrian Detection

MASTER OF SCIENCE THESIS

For the degree of Master of Science in Electrical Engineering at Delft University of Technology

Bart van den Bogert, 4215192

July 5, 2018

28 nm CMOS Array of Strips for Pedestrian Detection

Bart van den Bogert

supervised by:
Prof. dr. ing. A. Neto and Prof. dr. ing. N. Llombart

co-supervised by:
dr. D. Cavallo and ir. S. L. van Berkel

Terahertz Sensing Group
Faculty of Electrical Engineering, Mathematics and Computer Science
Delft University of Technology

DELFT UNIVERSITY OF TECHNOLOGY
DEPARTMENT OF
MICROELECTRONICS

The undersigned hereby certify that they have read and recommend to the Faculty of Electrical Engineering, Mathematics and Computer Science for acceptance a thesis entitled **"28 nm CMOS Array of Strips for Pedestrian Detection"** by **Bart van den Bogert** in partial fulfillment of the requirements for the degree of Master of Science.

Dated: 06-07-2017

Chairman:

prof. dr. A. Neto

Advisors:

prof. dr. A. Neto

dr. D. Cavallo

Committee Members:

dr. D. Cavallo

dr. M. Spirito

Abstract

Due to technology trends such as autonomous driving, the need for robust safety in the automotive industry increases. The safety comes from sensors that are able to image the environment and systems that use this information to avoid incidents and retain maximum safety. Detection of pedestrian has high importance since a missed detection can be lethal. Current solutions for pedestrian detection are based on infrared and optical cameras. With these solutions it can be challenging to detect pedestrians under conditions such as cold/foggy conditions, especially during nighttime. In this scenario through clothes penetration of infrared radiation is poor. Instead, terahertz radiation penetrates better through clothes, making terahertz imagers a viable solution to increase safety in the framework of autonomous driving.

The focus on automotive sensors requires that the solution needs to be low-cost, low power and compact. Traditional passive terahertz detectors are based on cryogenically cooling or active illumination of the target to maximize the sensitivity, since this is not applicable in automotive designs we design an array that can be combined with direct detectors to increases the sensitivity by maximizing the effective bandwidth. The sensor needs to have sufficient resolution to detect the pedestrians at distances up to 10 meters combined with sufficient sensitivity to also perform in weather conditions such as fog.

The design in this is thesis is a terahertz imager with a connected array of dipoles as receiving antenna. By connecting the elements in the array, the dipoles behave broadband and can be densely placed on a focal plane. The array of elements is placed under a silicon lens to sample the far field. The prototype proposed is a limited size version of the full array, which contains less pixels to make it less expensive to manufacture. The design is able to detect pedestrians with sub-Kelvin sensitivity on hot days while also achieve an spatial resolution of 15 cm at maximum distance. With this result the prototype shows that it is a suitable solution to extrapolate further into a full array design. It shows it is an addition to the existing sensors and it fills a gap in pedestrian detection.

This thesis is submitted in partial fulfillment of the requirements for the degree of Master of Science n Electrical Engineering at Delft University of Technology.

Bart van den Bogert

Acknowledgements

First of all, I would like to thank Prof. dr. Andrea Neto for giving me the opportunity to do my master thesis at the Terahertz Sensing Group. You were very encouraging, thank you for your support.

Secondly, I would like to thank Prof. dr. Nuria Llombart for the enthusiasm she was able to activate within me to get me interested in Electromagnetics.

Thirdly, I would like to specially thank ir. Sven van Berkel for supervising me through the whole period of my thesis. His great input and support combined with big patience from time to time made his guidance a tower of strength to me. I learned a lot from you.

Furthermore, I would like to thank Harshitha, Diego, Zhengzheng, Huasheng, Stefan and Ahmed for being my office roommates during my thesis. I enjoyed the ambiance we were able to create in our office.

Furthermore, I would like to thank all the other members of the Terahertz Sensing Group, I look back on this period as a valuable period where I learned a lot in a pleasant environment.

I would like to thank Declan, Franck and Jorden for the periodical distraction visiting Feyenoord together. I will pay you some drinks during the matches while you are still students.

I also would like to thank my friends from college Apollo, although my presence during my thesis was rare, I really enjoyed the years I have been a member, Tsjoch!

Diamonds are made under pressure.

Contents

List of Figures

List of Tables

Chapter 1

Introduction

This chapter contains the introduction to the research done, clarifying the background and the application considered. First, the background in pedestrian detection will be introduced, followed by the solution proposed in this thesis. The last section of the chapter gives an overview of the outline of the thesis.

1.1 Pedestrian Detection

With the evolution of the automotive industry as we know, the demands on what a car is able to detect change [1]. Traffic flow is affected by human driving involving reaction time, delays and human error which can be removed in autonomous cars by replacing the human driver with a computer controlled systems and sensors [2]. When looking at the overview of the present systems on a car, a large variety of sensors are found, having various functionalities such as temperature and pressure monitoring, locating the cars position on the road and pedestrian detection [3]. With the development of autonomous vehicles, economic benefits can be made, but this asks for determining appropriate standards for liability and security [4].

One of the most important and challenging application that is considered here is the detection of other road users. Especially pedestrians are hard to observe, due to their small size compared to cars and their possible unpredictable movements and locations [5]. Since the result of a missed detection can be fatal, a high demand on safety performance is required in pedestrian detection [6].

Currently, different kinds of sensors for pedestrian detection are used such as Radar [7], near-infrared [8], far-infrared [9] and optical cameras [10]. All different types of sensors

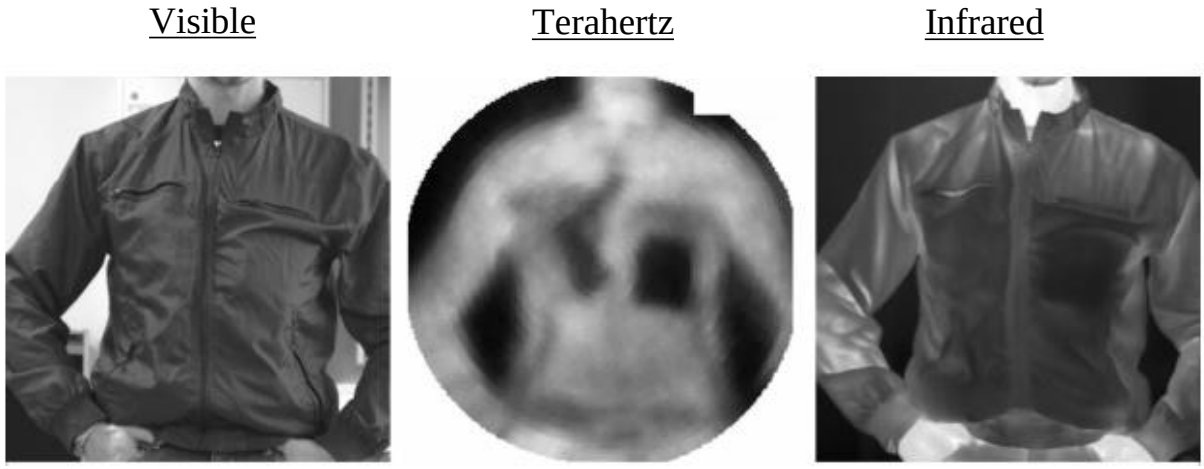

Figure 1.1: Image resolved from visible, terahertz and infrared light in left, middle and right respectively. A limited performance in terms of penetrability of clothing occurs for visible and infrared light, while terahertz radiation is able to penetrate through the clothing [13].

have their own strengths and limitations, so a combination of them is needed to design a robust system [11]. Radar sensors use active illumination, but will be relatively big compared to the other sensors. Optical cameras depend on optical light illuminating the target, which can cause problems during nighttime. Near-infrared sensors are also based on active sources which are relatively expensive. Far-infrared (FIR) are thermal cameras receiving the thermal radiation described by Planck's law. The FIR sensors cost less but are also limited in performance for two important reasons. First, the infrared radiation is attenuated strongly in atmospheric conditions such as fog and rain [12]. Second, FIR sensors can be limited in the penetration through clothing (Fig. 1.1), making it harder to detect a person. Fig. 1.1 shows that, in detecting pedestrians, a big portion of the radiation is blocked due to the clothing the pedestrians wear. Fig. 1.1 is from the work [13], that focuses on security imaging where the radiation is required to penetrate through the clothing in order to detect concealed weapons. However, Fig. 1.1 also illustrates the fact that a pedestrian will be a more distributed source of radiation in the terahertz (THz) regime w.r.t. the infrared regime. This holds especially in the scenario when it is cold, foggy and at night, where a pedestrian is likely to wear multiple layers of clothing, blocking most of the infrared radiation. For this reason, a THz imager will be able to complement current infrared and optical systems, increasing the reliability of current pedestrian detection systems.

As indicated in Fig. 1.2, the thesis discribes sensors that operate in the THz regime. Which is at lower frequency than present solutions based on infrared (IR) and optical cam-

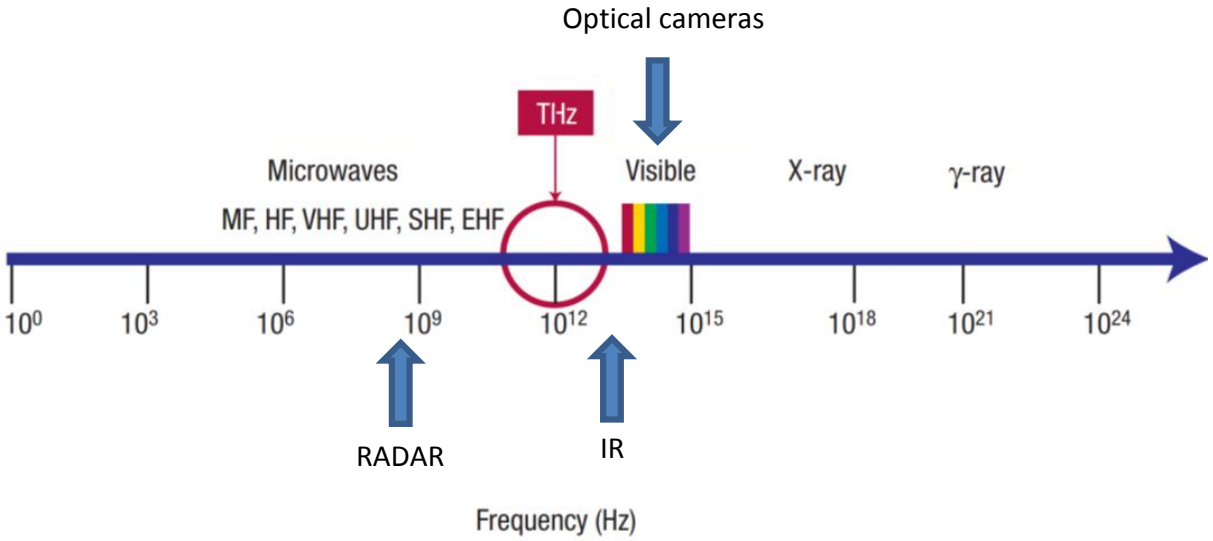

Figure 1.2: Electromagnetic spectrum and indicated are the positions of RADAR, terahertz (THz), infrared (IR) and optical cameras [14].

eras, but at higher frequencies than RADAR.

1.2 Solution proposed in this Thesis

Microwave frequencies up to 600 GHz are characterized by low atmospheric attenuation and the ability to penetrate through clothing. These features show that a THz imager can complement current existing images for the purpose of pedestrian detection. Best image quality can be achieved in an active scenario, where both THz sources and detectors are being used. However, the development of circuitry in microwave and millimeter wave applications is still considered to be a challenging task [15]. THz sources are bulky and power hungry, making them unsuitable for integration in a car. For this reason, the need arises to develop passive THz cameras, i.e. radiometers. Similar to FIR cameras, a passive THz camera will detect the thermal radiation that can be described by Planck's law.

Over the past decades, looking into the development of circuitry in microwave and millimeter applications has taken a flight, while in the THz regime (from 300 GHz to 3 THz) the solutions have proven themselves to be challenging [15]. The usage of this part of the electromagnetic (EM) spectrum is limited in terms of tunable sources and efficient amplifiers for the use of large arrays. Without the availability of efficient coherent mixers that can be integrated in large arrays, incoherent detection (i.e. direct detection)

architectures are preferred at submillimeter-wave frequencies. The use of direct detectors comes with some benefits compared to other detectors. The first advantage is the easy read-out circuitry that is needed, since the signal is received incoherently i.e. no mixers are needed; for this a detector-integrator combination is used. The second advantage of using direct detectors is that they consume less power than coherent detectors, since no oscillators, mixers and amplifiers are used. The third advantage is that because of the simple read-out circuitry, large focal plane arrays (FPA) can be manufactured. When using integrated technologies such as CMOS, low-cost imaging applications are enabled, suitable for commercial applications like the automotive industry. A quasi-optical system containing elements such as lenses or reflectors is combined with the FPA to create a large field of view (FoV).

The current state-of-the-art uncooled passive submillimeter-wave imagers [16] are insufficiently sensitive to operate without actively illuminating the source of interest [17]. The sensitivity of a direct detector imager is expressed as the Noise Equivalent Temperature Difference (NETD), which is the temperature resolution of the system. The NETD is the temperature sensitivity which is the minimal temperature difference from the source of interest that can be distinguished form the noise fluctuation in the image. It is shown in [17] the NETD can be expressed as:

$$\Delta T = NETD = \frac{NEP}{k_B \bar{\eta}_{sys} \Delta f_{rf}} \frac{1}{\sqrt{2\tau_{int}}} \tag{1.1}$$

with k_B the Boltzman constant ($1.38 \times 10^{-23}\ m^2 kgs^{-2}K^{-1}$), $\bar{\eta}_{sys}$ the average system efficiency, Δf_{rf} the operational bandwidth of the feed (the product of $\bar{\eta}_{sys}\Delta f_{rf}$ is referred to as the effective bandwidth Δf_{rf}^{eff}) and τ_{int} the integration time of the integrator. This equation will be explained further in chapter 2.

Eq. (1.1) can be rewritten as a function for the imaging speed, defined as $s = \frac{1}{\tau_{int}}$. In Fig. 1.3 the imaging speed s is shown as a function of NEP and effective bandwidth when a temperature sensitivity of 1 K is required. Fig. 1.3 illustrates the focus area of the imager, where the solution will be based on in this thesis. The NEP of the whole system is depending on the read-out circuitry and the environment the system is placed in. The performance of direct detectors can be increased by cooling the system to cryogenic temperatures to increase their performance in terms of sensitivity [18] [20]. When uncooled detectors are used, NEPs of 12 $nW/\sqrt{Hz}$ are achieved in [16] or even as low as 0.48 $pW/\sqrt{Hz}$ [19]. This can be improved further by cryogenically cooling the system to achieve NEPs of $3 \times 10^{-19}\ W/\sqrt{Hz}$ [20]. The ultimate limit one can achieve by cooling is that the noise received is not limited by the noise introduced by the detector, but by the

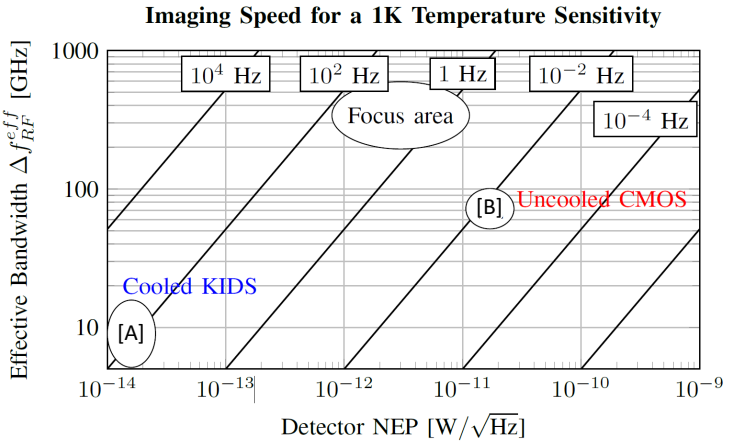

Figure 1.3: The focus area (from [17]) of the passive imager used in this thesis, also showing: [A] cooled KIDS as in [18] and [B] uncooled CMOS as in [16] .

erratic fluctuations of the signal itself. However, cooling will not be applicable here, since this will introduce a bulky power consuming cooling installation that is unaffordable for usage in the automotive industry. To compensate in the lag of sensitivity of the uncooled system, one can increase the bandwidth of the system to increase the power received (from Eq. (1.1)).

The design developed in this thesis is a THz imager that utilizes a broad portion of the THz spectrum efficiently such that it, combined with a detector with a NEP in the order of $pW/\sqrt{Hz}$, is able to achieve real-time refresh-rates with sub-Kelvin temperature sensitivity. This thesis is part of the Tera-hertz silicon-Integrated CAMera (TICAM) project, which is a passive imager for the detection of pedestrian in an automotive application.

1.3 Outline of the Thesis

This thesis is organized in 6 more chapters: Chapter 2 is on a further analysis of passive terahertz imaging, deriving the figures of merit. Chapter 3 is the analysis of the application focused on pedestrian detection and how this sets the requirements for the design of the imagers. In chapter 4, possible solutions for the design are evaluated and a quasi-analytical model for connected arrays of elements is derived. Chapter 5 contains the aspects that are taken into account in the optimization to determine the final design for the array. Then the final design is evaluated in chapter 6 to find the realized performance.

Conclusions and future work prospects are given in chapter 7.

Chapter 2

Passive Terahertz Imaging

This chapter explains the figures of merit used in THz imaging. An overview of the system can be found in Fig. 2.1, where an instrument box is looking at an incoherent source of temperature T_s radiating power. In the instrument box, the FPA of detectors with feed period d_f is placed under optics with diameter D and focal distance F. The source solid angle is defined as Ω_s and the optics solid angle is Ω_O.

2.1 Back-Body Radiation

The main purpose of a radiometer is to detect the spectral brightness distribution of a source $B(f, \Omega)$ with temperature T_s over a source solid angle Ω_s. The spectral brightness of an incoherent source, which is also referred to as black-body radiation, can be described by Planck's law as [21]:

$$B(f,\Omega) = \frac{f^2}{c^2} \frac{2hf}{e^{\frac{hf}{k_B T_s(\Omega_s)}} - 1} \left[\frac{W}{m^2 SrHz}\right] \tag{2.1}$$

where f is the frequency, c is the speed of light ($2.99 \times 10^8\ m/s$), h is Planck's constant ($6.626 \times 10^{-34}\ m^2 kgs^{-1}$) and k_B is Boltzman's constant ($1.38 \times 10^{-23}\ m^2 kgs^{-2}K^{-1}$). Planck's law describes the spectrum that is emitted as a function of the source temperature, there are two limits in this expression:

The first limit is called the Rayleigh-Jeans limit and is valid when $hf \ll k_B T_s$, which is the case for pedestrian detection. In this limit, the spectral brightness becomes:

$$B(f,\Omega)|_{hf \ll k_B T_s} \approx B^{RJ}(f,\Omega) = \frac{f^2}{c^2} 2k_B T_s(\Omega)\,. \tag{2.2}$$

When the sources have a higher temperature than 270 K and looking at frequencies lower than 1 THz, the error due to the difference between Planck's law and the Rayleigh-Jeans

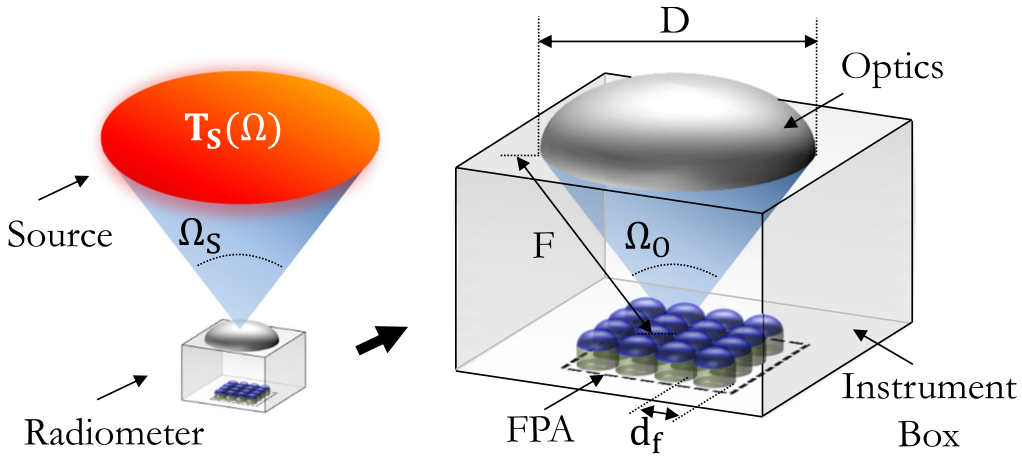

Figure 2.1: System under investigation, left: Instrument box (radiometer) placed under an incoherent source of temperature T_s with source solid angle Ω_s. Right: the instrument box containing a square focal plane array (FPA), antenna diameter d_f, of detectors placed under optics with diameter D and at focal distance F over solid angle Ω_O. [17]

limit is less than 10 %.

The other limit is the Wien's limit, valid for $hf \gg k_B T_s$ which is described as:

$$B(f,\Omega)|_{hf \gg k_B T_s} \approx B^{Wien}(f,\Omega) = \left(e^{\frac{hf}{k_B T_s(\Omega)}} - 1\right)^{-1} \approx e^{-\frac{hf}{k_B T_s(\Omega)}} . \tag{2.3}$$

In this equation it can be seen that the brightness decreases exponentially as a function of the frequency; the lower frequency will have the strongest contribution in the emitted radiation. Due to this decrease in spectral power, increasing the bandwidth of the system is not beneficial in this limit. For this thesis is assumed the sources of interest are in the Rayleigh-Jeans limit, thus Eq. (2.2) will be used in the further analysis.

2.2 Received Power

The purpose of a direct detector is to convert the incident black-body radiation, as described by Planck's law, to a signal that can be read-out by low frequency circuitry. A schematic overview of the antenna-detector combination can be found in Fig. 2.2. This consists of three main components: an antenna with effective bandwidth Δf_{rf}^{eff} receiving an erratic THz signal; the detector (with noise equivalent power NEP) that transforms the incident terahertz power to a DC voltage at the output of the detector (possibly modulated

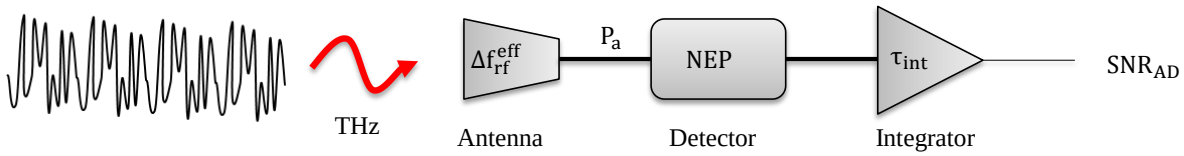

Figure 2.2: Schematic overview of the a direct detector. A terahertz EM radiation signal is received by the antenna with effective bandwidth $\Delta f_{rf}^{eff} = \bar{\eta}_{sys}\Delta f_{rf}$; the energy is summed up incoherently in the detector with Noise Equivalent Power NEP. The detector gets read-out by the integrator every τ_{int} seconds, resulting in a signal to noise ratio after detection of SNR_{AD}.

signal to avoid flicker noise contributions). The low frequency signal at the output of the detector is then integrated for a integration time τ_{int} in order to reduce noise fluctuations introduced by the detector. The signal to noise ratio (SNR) after detection is denoted as SNR_{AD}.

For direct detector schemes the SNR can be expressed as [23]:

$$SNR = \frac{P_a}{NEP}\sqrt{2\tau_{int}} \tag{2.4}$$

where P_a is the average received power accepted by the detector during the integration time τ_{int}. The NEP is the noise equivalent power from the detector, which is the power that is needed to get unit SNR after 0.5 seconds of integration.

The expression for the average received power P_a^n of the n^{th} detector-antenna combination from a incoherent source, is equal to the integration of the targets brightness distribution (following Eq. (2.1)) over the operational bandwidth, Δf_{rf},over the source solid angle, Ω_s, weighted by the effective area of the quasi optical system, A_{eff}^O:

$$P_a^n = \frac{1}{2}\int_{\Delta f_{rf}}\int_{\Omega_s} A_{eff}^O\left(f, \Omega - \Omega_n\right) B\left(f, \Omega\right) d\Omega df\,. \tag{2.5}$$

The factor $\frac{1}{2}$ before the integrals is due to the fact of only a single polarization is received. The effective area of the quasi optical system related to the directivity of the antenna, $D^O(f,\Omega)$, as: $A_{eff}^O = \frac{c^2}{f^2}\frac{1}{4\pi}\eta_{sys}(f)D^O(f,\Omega)$, where η_{sys} is the system efficiency of the feed; this will be defined further.

2.2.1 System Efficiencies

This part describes the efficiencies that are taken into account to calculate the system efficiency, η_{sys}, as:

$$\eta_{sys}(f) = \eta_{so}(f)\eta_{mc}(f)\eta_{ohm}(f)\eta_{imp}(f)\eta_{f2b}(f)\eta_{refl}(f)\,. \tag{2.6}$$

In Eq. (2.6), η_{so} is the spillover efficiency, η_{mc} is the mutual coupling efficiency, η_{ohm} is ohmic efficiency, η_{imp} is the matching efficiency, η_{f2b} is the front-to-back ratio efficiency and η_{refl} is the reflection efficiency. All these efficiencies will now be clarified further.

Reciprocity theorem shows that an antenna can be modeled as a receiver or a transmitter to evaluate the patterns and efficiencies. This thesis derives a quasi-analytical model of an antenna array as if it were used in transmission. Also the final array optimization will be performed in transmission using CST Microwave Studio [24]. The following efficiency terms will also be explained in transmission. However, do note that the array will be used in a passive scenario, i.e. only in reception.

Spillover Efficiency

The first efficiency term that is taken into account is the spillover efficiency. Since this FPA will be using a lens to focus the beams in the FoV, some spillover will be introduced. While some of the radiated power is captured by the aperture of the lens (Ω_O), some is radiated to angles wider than the truncation angle of the lens θ_0. The power that is not radiated on the lens aperture is assumed to be lost.

This can be expressed mathematically as:

$$\eta_{so}(f) = \frac{\int_{\Omega_O} D^f(f,\Omega) d\Omega}{4\pi} \tag{2.7}$$

where Ω_O is the solid angle where the lens aperture is present, D^f is the directivity pattern of the antenna feed used.

Mutual Coupling Efficiency

When an element is radiating power, some power is captured by the neighboring elements. In an imaging array, where each antenna corresponds to a pixel in the imaging plane, power that is dissipated in neighboring elements is assumed the be lost.

Considering that the influence of mutual coupling is stronger when elements are placed closer to each other, mutual coupling is seen as the fundamental limit for closely spaced arrays of elements [25].

The power radiated by the fed unit is P_{rad} and the power dissipated in the neighboring elements is P_{mc}. The mutual coupling efficiency is calculated as the ratio P_{rad} and the total

power $P_{tot} = P_{rad} + P_{mc}$:

$$\eta_{mc} = \frac{P_{rad}}{P_{tot}} \,. \tag{2.8}$$

For the simulation in CST, one pixel is excited, which radiates P_{rad}, the neighboring delta gaps are modeled as resistive elements with impedance Z_g to calculate the amount of power absorbed in these elements.

Ohmic Efficiency

The chip design is based on the use of CMOS technology (appendix (A)) placed under a silicon lens. When CMOS technologies are used, ohmic loss are introduced due to the finite conductivity of the metal layers and dielectric losses in the low-resistive silicon of the technology. The bulk silicon considered here is characterized by a conductivity of 10 S/m. CST provides an efficiency which contains both contributions of ohmic losses and mutual coupling.

Matching Efficiency

Impedance mismatch between the antenna and the detector determines the matching efficiency. Maximum power transfer between a port or detector with impedance Z_g and the antenna with impedance Z_{in} is when the impedances are conjugately matched. When the impedances are not conjugately matched, not all power generated by the port is radiated by the antenna, but reflected back into the port. In this work, the detector impedance Z_g is unknown. The optimization of the input impedance is performed using a constant and real generator impedance over the frequency band. Final optimization must be performed together with dimensioning the detector in order to obtain maximum power transfer.

The reflection coefficient, Γ, is calculated as:

$$\Gamma = \frac{Z_{in} - Z_g}{Z_{in} + Z_g} \,. \tag{2.9}$$

The matching efficiency is found as:

$$\eta_{imp}(f) = 1 - |\Gamma(f)|^2 \tag{2.10}$$

as a function of frequency, since the impedance can generally not be assumed constant for wideband systems. The impedance of the detector is approximated here as real and constant over the whole frequency spectrum.

Front-to-Back Efficiency

In the imager the lens is placed on one side of the antenna. Since the antenna radiates in both hemispheres, some power is radiated back, away from the lens. This power is assumed to be lost, defining the front-to-back efficiency as:

$$\eta_{f2b}(f) = \frac{\int_{\Omega_{front}} D^f(f,\Omega)d\Omega}{4\pi} \tag{2.11}$$

where D^f is the feed directivity and Ω_{front} is the front hemisphere (where the lens is present).

Reflection Efficiency

Using the lens, reflections as in Fig. 2.3 will occur. The difference in characteristic impedance between the air and the silicon introduces reflections with reflection coefficient:

$$\Gamma_{refl} = \frac{Z_{air} - Z_{sil}}{Z_{air} + Z_{sil}} \tag{2.12}$$

where Z_{air} is the characteristic impedance of air and Z_{sil} is the characteristic impedance of silicon. The reflection efficiency η_{refl} is then calculated as:

$$\eta_{refl} = 1 - |\Gamma_{refl}|^2 \ . \tag{2.13}$$

At the top of the lens the rays are mostly transmitted, but at the sides of the lens the rays are reflected back inside the lens. To minimize the reflections, a matching layer can be used to match the silicon lens with the air, but the bandwidth is limited.

2.3 Effective Bandwidth and Effective Gain Pattern

From the system efficiency the effective bandwidth of the system can be calculated as:

$$\Delta f_{rf}^{eff} = \Delta f_{rf} \bar{\eta}_{sys} \tag{2.14}$$

where $\bar{\eta}_{sys}$ is the average system efficiency as $\bar{\eta}_{sys} = \frac{1}{\Delta f_{rf}} \int_{\Delta f_{rf}} \eta_{sys}(f)df$.
Also the system efficiency can be used to calculated the effective gain pattern:

$$G_{eff}(\Omega) = \int_{\Delta f_{rf}} \eta_{sys}(f) D^O(f,\Omega)df \tag{2.15}$$

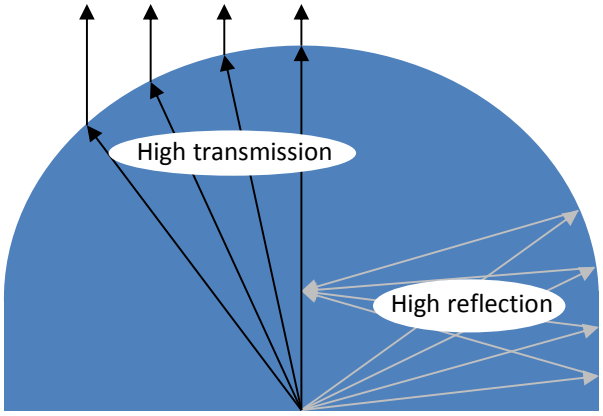

Figure 2.3: Rays picture in a silicon lens. At broadside the rays are mostly transmitted in the air, while at the side of the lens most of the rays are reflected back inward the lens.

which is the spectral directivity weighted by the system efficiency and integrated over the operational bandwidth, also referred to as radiometric pattern. The radiometric pattern represent the incoherent integration of power of the detector and illustrates where the radiometer integrates its power angularly.

Assuming the source of interest is operating in the Rayleigh-Jeans limit, the received power from Eq. (2.5) substituting Eq. (2.2) into (2.15) gives:

$$P_a^n = \frac{k_B}{4\pi} \int_{\Delta f_{rf}} T(\Omega) G_{eff}(\Omega) d\Omega \,. \tag{2.16}$$

Assuming that the source is distributed (large compared to the radiation pattern) and uniform in terms of temperature, the integration over the source solid angle of the effective gain pattern is approximated as 4π, the average received power $\bar{P}_a$ of each feed is then written as:

$$\bar{P}_a = k_B \bar{T}_s \bar{\eta}_{sys} \Delta f_{rf} \tag{2.17}$$

where $\bar{T}_s$ is the average source temperature.

2.4 Temperature Sensitivity and Imaging Speed

To find the temperature sensitivity of the imager, we first consider an incoherent source of average temperature $\bar{T}_s$ resulting in a received power at the detector $\bar{P}_a$. A difference in source temperature ΔT will result in a difference in received power as ΔP. From Eq. (2.17) it follows:

$$\Delta P = k_B \Delta T \bar{\eta}_{sys} \Delta f_{rf} \,. \tag{2.18}$$

Substituting this in Eq. (2.4) and setting the SNR to unit gives the Noise Equivalent Temperature Difference (NETD), which is the minimal difference in temperature that can be distinguished from the noise fluctuations, i.e. the temperature resolution:

$$\Delta T = NETD = \frac{NEP}{k_B \bar{\eta}_{sys} \Delta f_{rf}} \frac{1}{\sqrt{2\tau_{int}}} \,. \tag{2.19}$$

By rearranging the terms in this equation, one finds an expression for the imaging speed s:

$$s = \frac{1}{\tau_{int}} = 2 \left(\frac{NETD \cdot k_B \bar{\eta}_{sys} \Delta f_{rf}}{NEP} \right)^2 \,. \tag{2.20}$$

In Fig. 1.3, it can be seen that the design in this thesis will be broadband. It will use a broad bandwidth to achieve a real-time imaging speed with sub-Kelvin sensitivity.

2.5 Resolution and Focal Plane Architectures

Resolution in an imager system is referred to the ability to distinguish multiple sources from each other in its focal plane. The resolution is influenced by the sampling configuration as a displacement from a feed $\Delta\rho$ in the focal plane leads to a scanning angle $\Delta\theta$ off broadside. For systems with large $F_\#$ this can be expressed as $\Delta\rho = F\Delta\theta$, where F is the focal length. To illustrate the principle of focal resolution one can look at Fig. 2.4.

If two point sources are angularly separated in the far field by $\Delta\theta$ (Fig. 2.4), two Airy patterns will coherently sum in the focal plane with the maxima separated by $\Delta\rho = F\Delta\theta$. Similar to the Nyquist rule, in order to be able to distinguish the two peaks, one not only needs to sample the peaks itself, but also in between. This implies that the required sampling is $d_f = \frac{\Delta\rho}{2} = 0.5 F_\# \Delta\theta$, relating the angular resolution and the feed size to each other as:

$$\Delta\theta = 2\frac{d_f}{F} \,. \tag{2.21}$$

Denser sampling of the feeds will thus create also a denser sampling in the far field. Although this implies that any angular resolution can be achieved, it is limited by the diffraction of the two Airy patterns with the optics to still see one peak in the focal plane. This peak is approximated by the -3 dB bandwidth of the intensity pattern to find the minimal angular resolution $\Delta\theta^{lim}$ needed as [26]:

$$\Delta\theta^{lim} \approx \frac{\lambda_c}{D} \,. \tag{2.22}$$

This is used in Eq. (2.21) to find the minimal sampling of the feeds as:

$$d_f^{lim} = 0.5 F_\# \lambda_c \,. \tag{2.23}$$

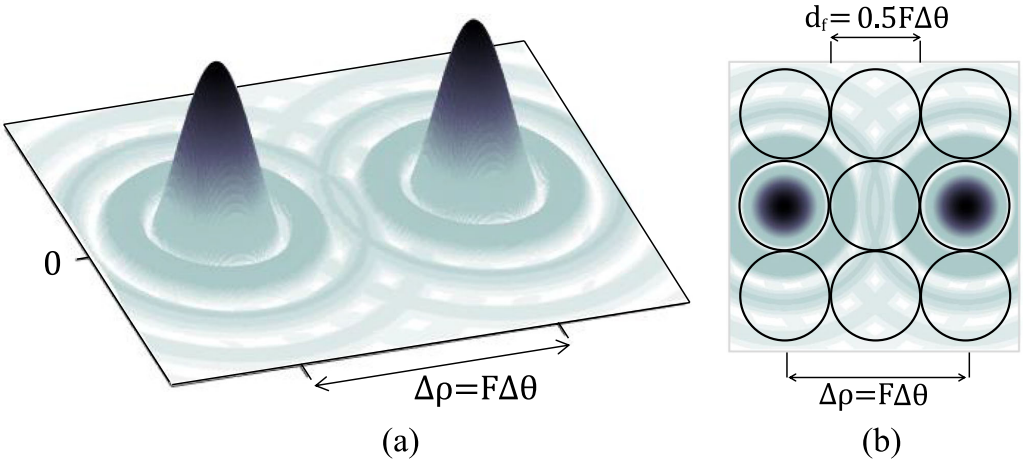

Figure 2.4: Overview of angular resolution for focal systems:(a) Two Airy disc patterns due to two point-sources are placed in the focal plane separated by $\Delta\rho = F\Delta\theta$; the related displacement is then $\Delta\rho = F\Delta\theta$, where F is the focal length. (b) Shows that to sample the focal plane and to resolve the two point sources, one must sample in the focal plane as $\frac{1}{2}F_{\#}\lambda_c$ [17].

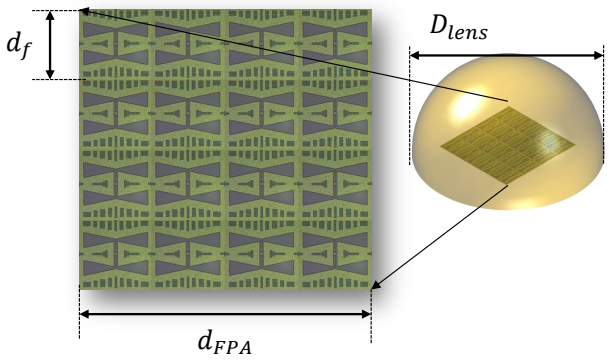

Figure 2.5: Combination of the silicon lens and the FPA placed under it. The feed period is d_f; the total diameter of the FPA is d_{FPA}.

When the feed array is sampled according to this rule, it is referred to as fully sampled. Denser sampling is limited by the diameter of the quasi-optical system. Sparser sampling will result in less spillover loss (Fig. 2.7) at the cost of lower angular resolution and thus it depends on the application which sampling is applicable.

To sample the FoV of the system, a FPA is placed under a silicon lens, as shown in Fig. 2.5. One of the parameters of interest is the period of the feeds d_f. Given the focal number of the lens, $F_{\#}$, the center frequency wavelength, λ_c, the sampling length is

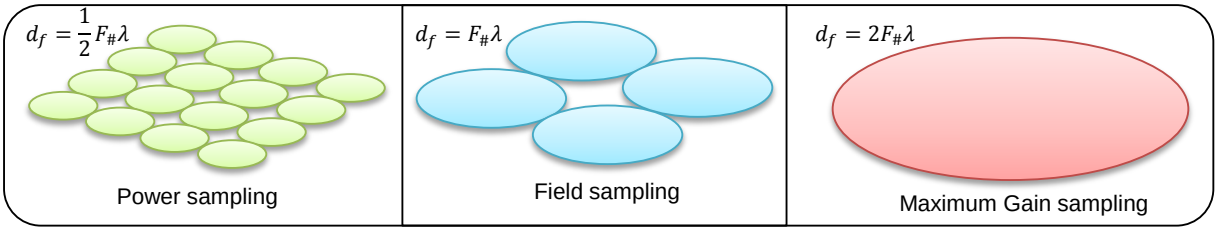

Figure 2.6: Overview of typical sampling lengths: power sampling, field sampling and maximum gain sampling.

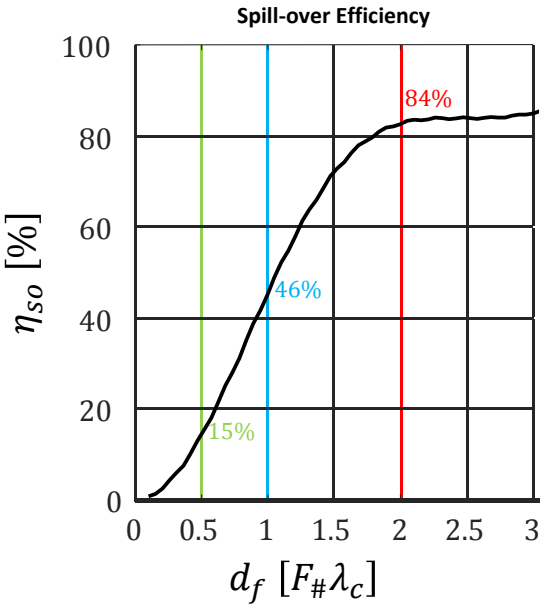

Figure 2.7: Spillover efficiency as function of the sampling length for high $F_{\#}$ systems. Highlighted in the figure are power, field and maximum gain sampling, ($0.5F_{\#}\lambda_c$,$1F_{\#}\lambda_c$ and $2F_{\#}\lambda_c$ respectively). F is the focal number of the optics and λ_c is the wavelength at the center frequency f_c

expressed in terms of $F_{\#}\lambda_c$. Typical sampling choices for feed periods are power sampling, field sampling and maximum gain sampling ($\frac{1}{2}F_{\#}\lambda_c$, $1F_{\#}\lambda_c$ and $2F_{\#}\lambda_c$ respectively; Fig. 2.6). When the size of the feed gets bigger, the directivity of the feed increases resulting in a higher spillover efficiency of the feed to the lens. The spillover efficiency as a function of the feed size is show in Fig. 2.7, this curve is typical for high $F_{\#}$ systems.

Equation (2.21) shows that a displacement in the position of the feeds is also translated in a scan from broadside of the radiation pattern. Since the FPA the feeds are displaced according to the sampling, the sampling also determines what the angular resolution is. In Fig. 2.8 the angular resolution is shown in terms of directivity patterns for the center frequency f_c. Denser sampling means larger overlaps between beams and crossing

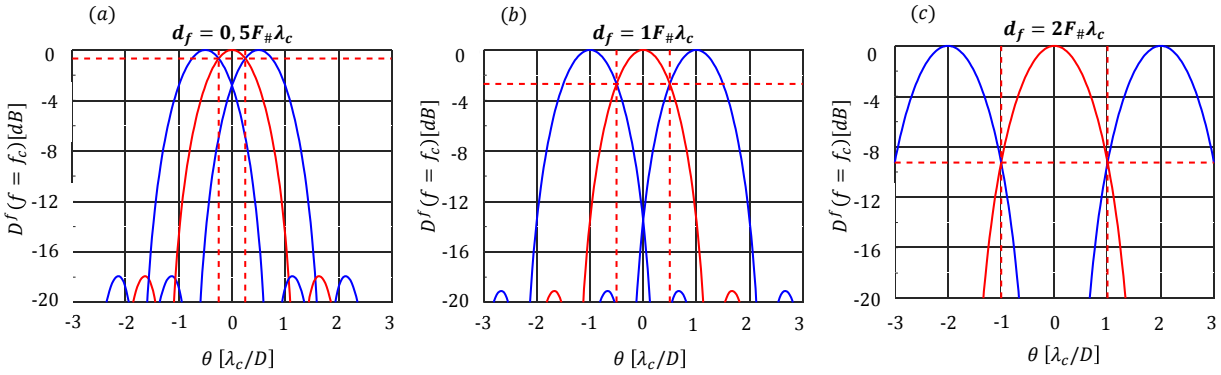

Figure 2.8: Overlap of the directivities of 3 unit cells for power sampling (a), field sampling (b) and maximum gain sampling (c). The red dotted lines indicate the crossing points of the centered patterns with its neighbors.

at higher pattern levels.

An overview of the angular resolution and the spillover efficiency per sampling is found in Table 2.1. This shows that it is not possible to maximize the angular resolution and the spillover efficiency at the same time; it will be a tradeoff between the two parameters.

In order to achieve a fully sampled FoV with a sparsely sampled array, one can also rotate mechanically the FPA (also known as jiggling) to let it scan across the sources of interest. This has been proven to be applicable in [27]. Moving the FPA will result in scan time loss (time the detector is not observing). Additionally, the instrumentation for rotation can be relatively bulky and not suitable for automotive sensors.

Sampling	Feed period d_f	Ang. resolution (Fig. 2.8)	Spillover eff. (Fig. 2.7)
Power	$\frac{1}{2}F_\#\lambda_c$	$\lambda_c/2D$	15%
Field	$1F_\#\lambda_c$	λ_c/D	46%
Max. Gain	$2F_\#\lambda_c$	$2\lambda_c/2D$	84%

Table 2.1: Relevant parameters for typical types of sampling.

Chapter 3

Pedestrian Detection

This chapter describes an analysis of the application at hand. First the scenario is described, then the effect of the focal plane array on the architecture is investigated. The predicted sensitivity is analyzed, and based on these considerations a proposal of an array design is reported.

3.1 Scenario Description

The scenario under investigation considers to use the imager in an automotive application to detect pedestrians at distances between 1 and 10 meters. The imager is envisioned to be used in urban areas, where many pedestrians will be on short-range from the car. A schematic overview of the situation is given in Fig. 3.1. The pedestrian is placed on 1, 5 and 10 meters from the car.

The radiated power is attenuated due to conditions as fog, that can be calculated by ITU-models [12]. L_{at} is the atmospheric loss in dB through transmission, which is corresponding to the atmospheric efficiency η_{at} as $\eta_{at} = 10^{\frac{L_{at}}{10}}$. The atmospheric efficiency for transmission through 10 meters of fog is shown in Fig. 3.2; it can be observed that the atmospheric losses are significant for these frequencies.

As it has been explained in the previous chapters, the overall goal is to maximize the effective bandwidth. For this reason one would like to operate at frequencies as high as possible, so that the same relative bandwidth corresponds to a larger absolute bandwidth. Operating at higher frequencies also implies a reduction in the size of the optics and chip area and improved resolution. However, the operational bandwidth should be used as efficiently as possible. In chapter 4 it will be shown that a relative bandwidth of 1:3 is feasible in a CMOS stratification. Considering these factors, the frequency band of 200 GHz to

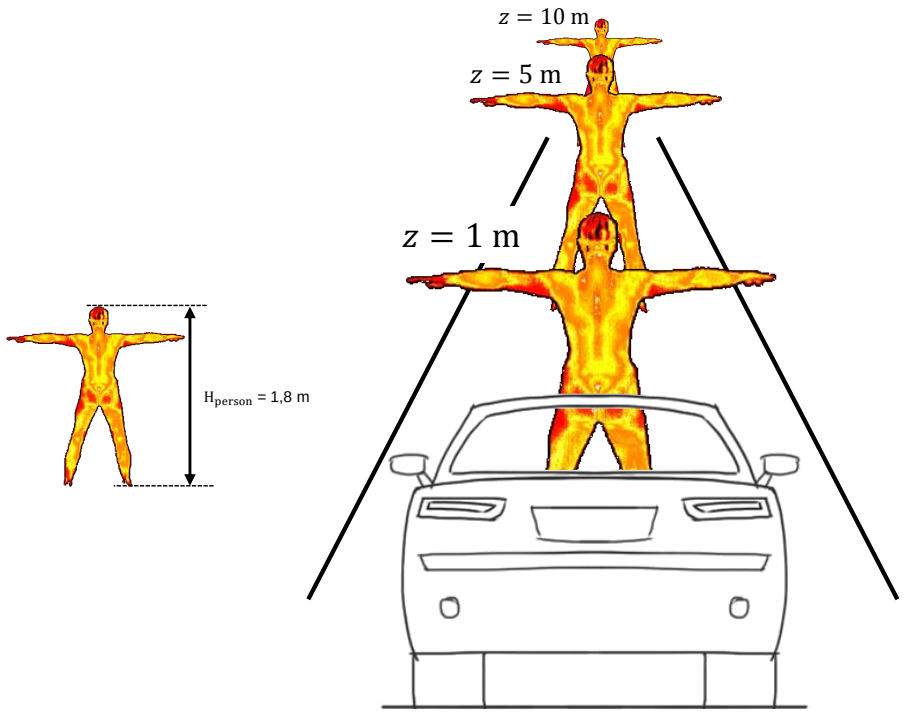

Figure 3.1: Overview of the considered scenario to evaluated the performance, where the pedestrian is placed at 1, 5 and 10 meters from the car.

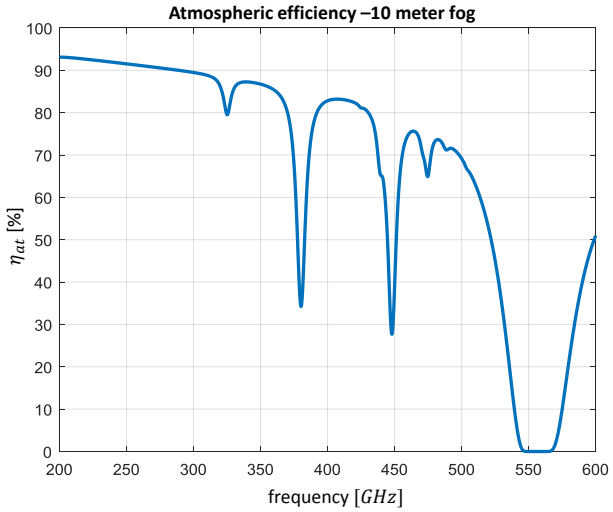

Figure 3.2: Atmospheric efficiency due to the attenuation from the fog (water density 2.5 g/m^3 and temperature of 23°C) for a transmission over 10 meters.

600 GHz is chosen as operational region.

The average atmospheric efficiency η_{at} from 200 GHz to 600 GHz due to fog and

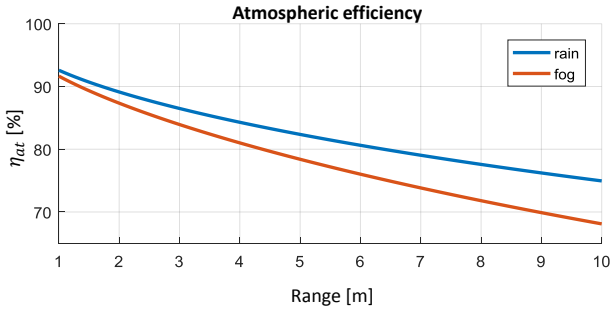

Figure 3.3: Average atmospheric efficiency over the bandwidth 200 GHz - 600 GHz as a function of range under rain and fog conditions. Rain parameters: rainfall rate 2.5 mm/h; fog parameters: temperature 23°C; water density 2.5 g/m^3.

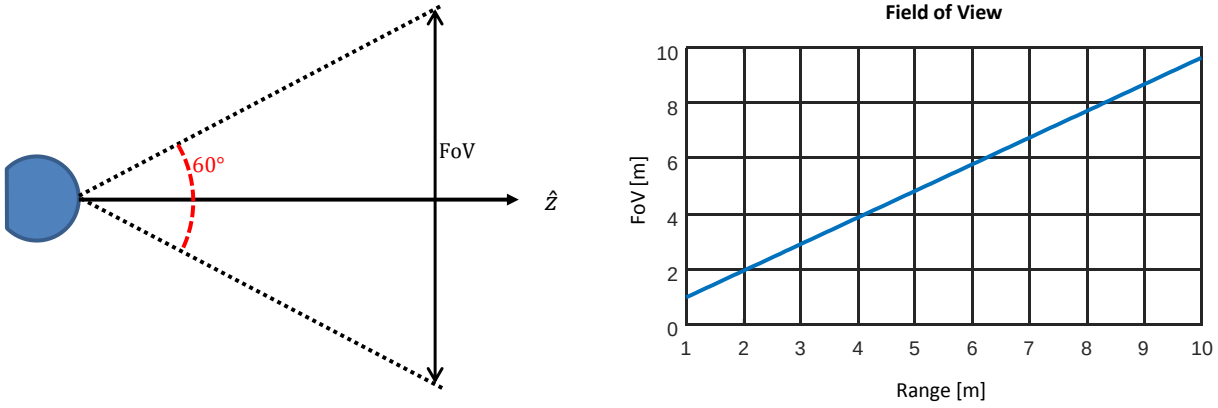

Figure 3.4: Field of view as a function of range for a scanning angle of 30°.

rain conditions is shown in Fig. 3.3. It shows that the atmospheric efficiency decreases with larger ranges.

To make to imager compact and suitable for integration in a car, the maximum diameter of the lens is set to be 5 cm with a typical focal number of approximately 0.67 (i.e. lens height 3 cm). The maximum scanning angle is ±30 degrees. It is assumed that within 30 degrees scanning angle there is limited degradation in scanning performance, without need to design advanced optical systems. The available FoV for the distance range can be found in Fig. 3.4, which shows a FoV of almost 10 meters at maximum distance.

The imager detects the difference in temperature between the pedestrian and the background. Therefore, the sensitivity that is required depends on the contrast in temperature between the pedestrian and the background. When the pedestrian is 30°C and the background air is 27°C, it requires a sensitivity of at least 3 K to distinguish the pedes-

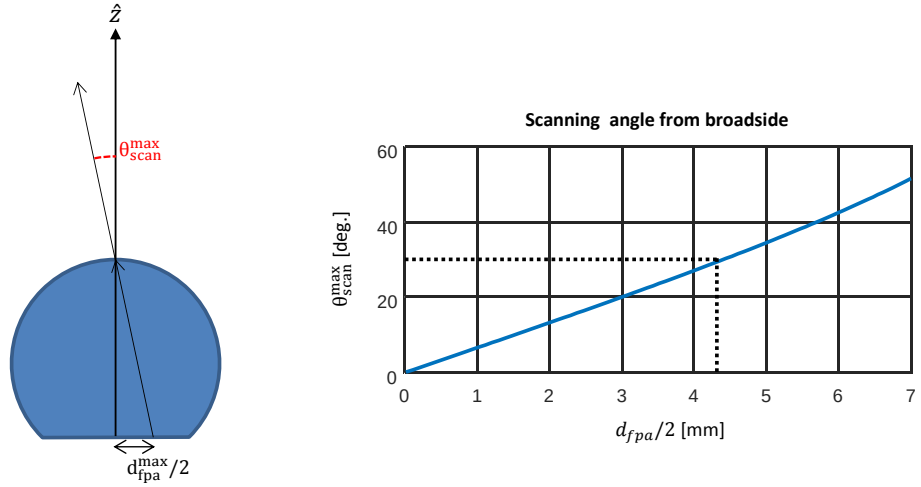

Figure 3.5: Scanning angle for a silicon lens. Left: Schematic side-view of the maximum scanning angle at the lens θ_{scan}^{max} and the corresponding maximal feed displacement d_{fpa}^{max}. Right: The maximum scanning angle as a function of the maximum feed displacement, for a maximum scanning angle of 30° the maximal size of the FPA is 8.9 mm.

trian. This implies that when the temperature contrast is bigger (i.e. on colder days), the required sensitivity is lower, making the pedestrian easier to be detected.

To analyze the influence of the temperature of the background two scenarios are defined. First a cold day where the air is 20 K colder than the pedestrian and then a hot day where the air is only 3 K colder then the pedestrian. This difference in temperature between the background and the pedestrian is also referred to as contrast.

3.2 Focal Plane Architecture

In Fig. 3.6 the scanning angle is shown as a function of the feed displacement, using Snell's law for the silicon lens ($\epsilon_r = 11.9$) to calculate the scanning angle. The lens has a diameter of 5 cm and a height of 3 cm. The maximal scanning angle is 30° and the corresponding maximal size of the FPA d_{fpa} is 8.9 mm.

The sampling of the FPA determines the feed size, the maximum number of feeds and the angular resolution, as shown in Table 3.1. Here it can be seen that for power, field en maximum gain sampling, the resolution becomes 0.43°, 0.86° and 1.72°, respectively. The FoV per pixel and the spatial resolution for all samplings can be seen in Fig. 3.6.

The spatial resolution on the pedestrian and the FoV for different distances is shown

Sampling	Feed period [μm]	Max. number of feeds	Ang. resolution
Power	65.86	135×135	0.43°
Field	131.73	67×67	0.86°
Max. Gain	263.46	33×33	1.72°

Table 3.1: Feed size, maximum number of feeds and resolution for different types of sampling.

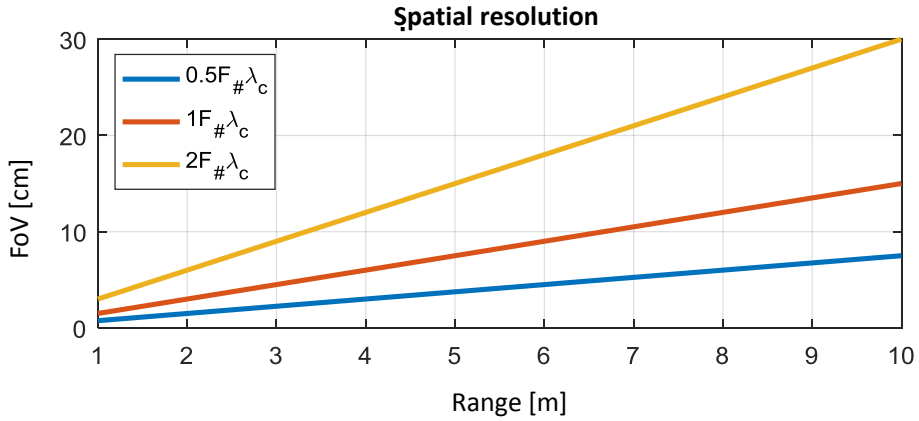

Figure 3.6: Spatial resolution for power, field and maximum gain sampling as a function of range.

in Fig. 3.7. It can be observed that the spatial resolution is related to the physical size of the pedestrian. For maximum gain sampling the spatial resolution is 30 *cm* at 10 meters which is relatively big compared to an arm or a leg. With the field sampling, a decent resolution of 15 *cm* at 10 meters is achieved, which is enough to see the arms and legs of the pedestrian.

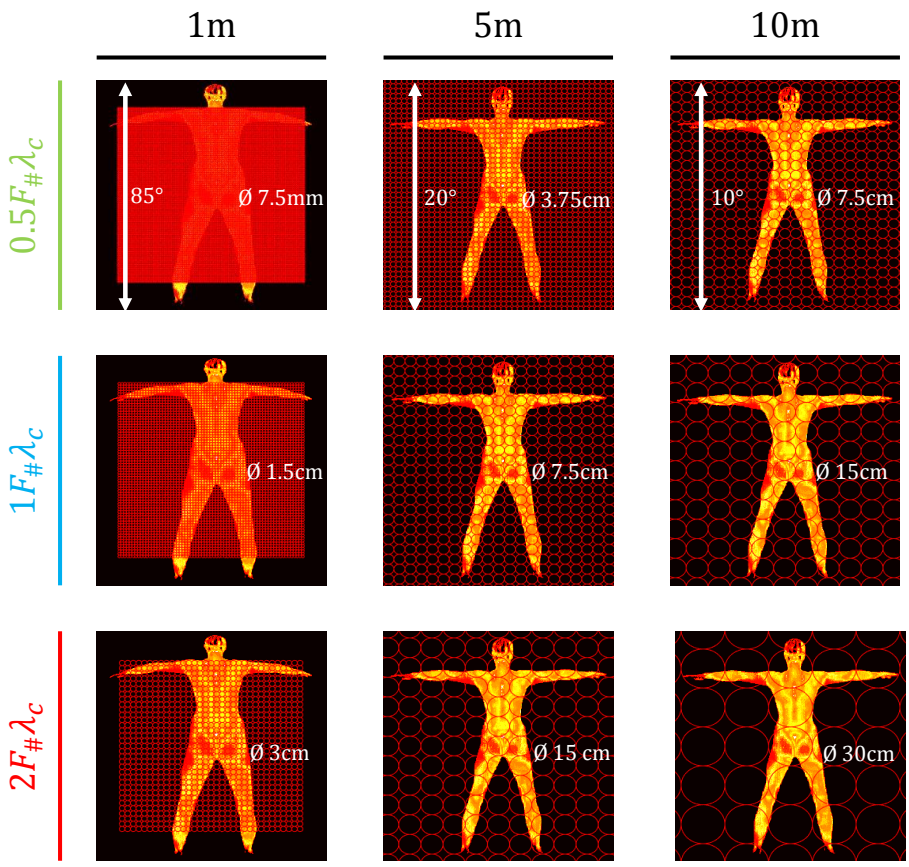

Figure 3.7: Spatial resolution for power, field and maximum gain sampling a pedestrian at 1, 5 and 10 meters.

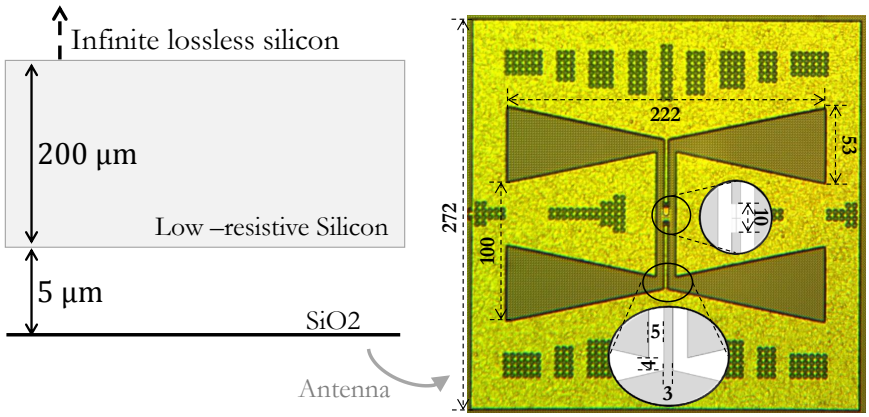

Figure 3.8: Overview TICAM single-pixel prototype: Left: Schematic side-view of the used CMOS stratification for the TICAM. Right: Schematic overview of the double-bowtie slot antenna [36]; the units are in μm, the holes made in the metal ground plane are present to meet the metal density rules of the technology [28].

3.3 Temperature Sensitivity

The NETD of the system is found as:

$$NETD = \frac{NEP}{k_B \bar{\eta}_{sys} \bar{\eta}_{atm}(R) \Delta f_{rf}} \frac{1}{\sqrt{2\tau_{int}}} \tag{3.1}$$

where $\bar{\eta}_{sys}$ is the average system efficiency, $\bar{\eta}_{atm}$ is the average atmospheric efficiency and R is the range.

In the analysis of the performance it is assumed that the TICAM single-pixel model from [28] is used. In April 2018 the TICAM research reached a special milestone by completing their first single-pixel prototype [29]. This prototype uses the stratification and antenna from Fig. 3.8. The most important simulated parameters of this prototype can be found in Table 3.2.

In Fig. 3.9 the specifications of the single pixel model (Table 3.2) are used, under fog condition with water density 2.5 g/m^3. In this figure, the NETD for power sampling ($0.5F_{\#}\lambda_c$) is too high for the required sensitivity. On the contrary, for field and maximum gain sampling, the NETD is around 1 K for the entire range of distances.

Up to now the sources of interest are assumed to be distributed, being much larger compared to the radiation pattern of the imager. In this case the maximum power is received by the imager, following Eq. (2.19). When pedestrians are close to the imager this condition applies, but when the pedestrian is further away the pixels will not only detect the source but also the background. This makes that the sensitivity differ per pixel,

Value	Parameter[μm]
Bandwidth	200 GHz-600 GHz
Used technology	28 nm CMOS (Fig. 3.8 left)
average system eff.	44 %
Noise Equivalent Power	0.62 $pW/\sqrt{Hz}$
Sensitivity	sub-Kelvin at real-time refresh rate

Table 3.2: Parameters of the single-pixel prototype of the TICAM passive imager in [28], the values are based on simulations.

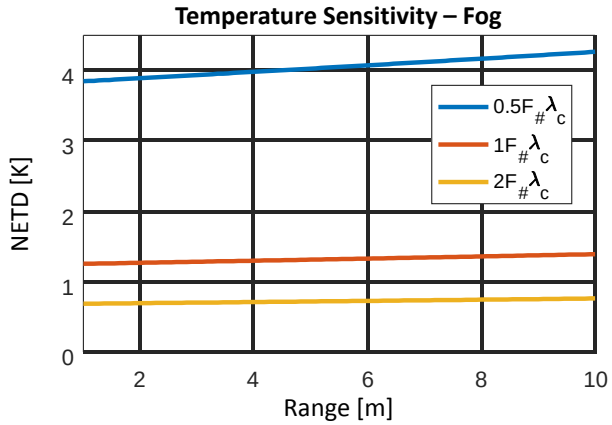

Figure 3.9: Sensitivity of the single-pixel model from table 3.2 as a function of distance for a distributed source under fog conditions (density 2.5 g/m^3).

due to the coupling between the radiation pattern and the presence of the pedestrian. This coupling affects the received power per pixel. The coupling efficiency for feed n is expressed as:

$$\eta_{co}^{n}(f,\Omega_n) = \frac{1}{4\pi}\int_{\Omega_s} D^f\left(f,\Omega-\Omega_n\right)d\Omega \tag{3.2}$$

with directivity $D^f\left(f,\Omega_n\right)$, where the source solid angle Ω_s defines the angular dimension of the pedestrian. In order to simplify the analysis, the coupling efficiency is calculated at the center frequency of 400 GHz and the directivity D^f is calculated assuming uniform illuminated circular feeds.

An illustration of the source coupling efficiency can be found in Fig. 3.10. As expected, it can be seen that the central pixel focused on the source have almost unit coupling efficiency, while the pixels at the background have no coupling. When the coupling is small, the received power is less, resulting in a lower sensitivity of the pixel to the temperature change of the pedestrian.

The coupling efficiency for the scenario from Fig. 3.1 is found in Fig. 3.11. It shows that

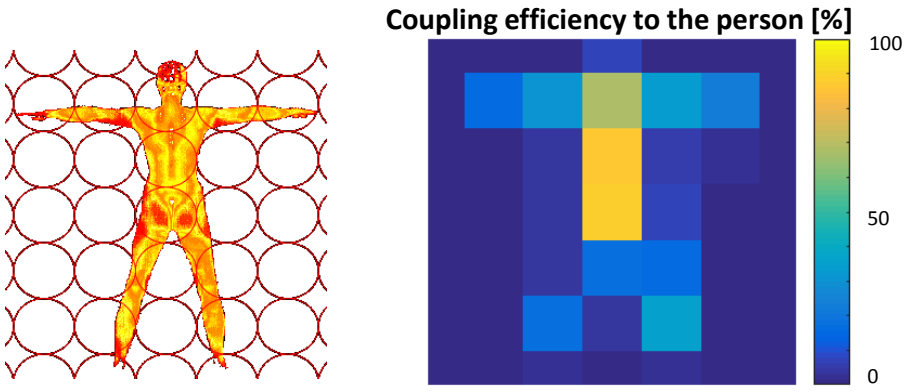

Figure 3.10: Overview of the coupling efficiency at 10 meters. Left: pedestrian of interest, every red circle is a sampled pixel. Right: Coupling efficiency of every pixel to the source of interest.

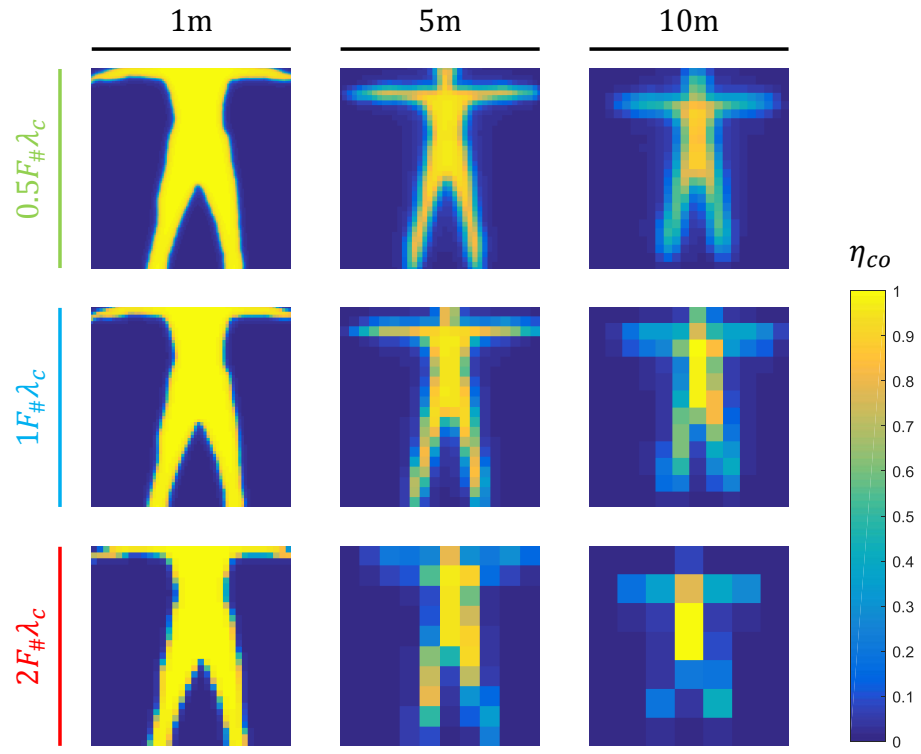

Figure 3.11: Overview of the coupling efficiency for different sampling configurations and distances to the pedestrian.

lower coupling occurs when the pedestrian is further away, since the pedestrian couples poorly with each pixel.

The atmospheric efficiency and the coupling efficiency are included in the sensitivity

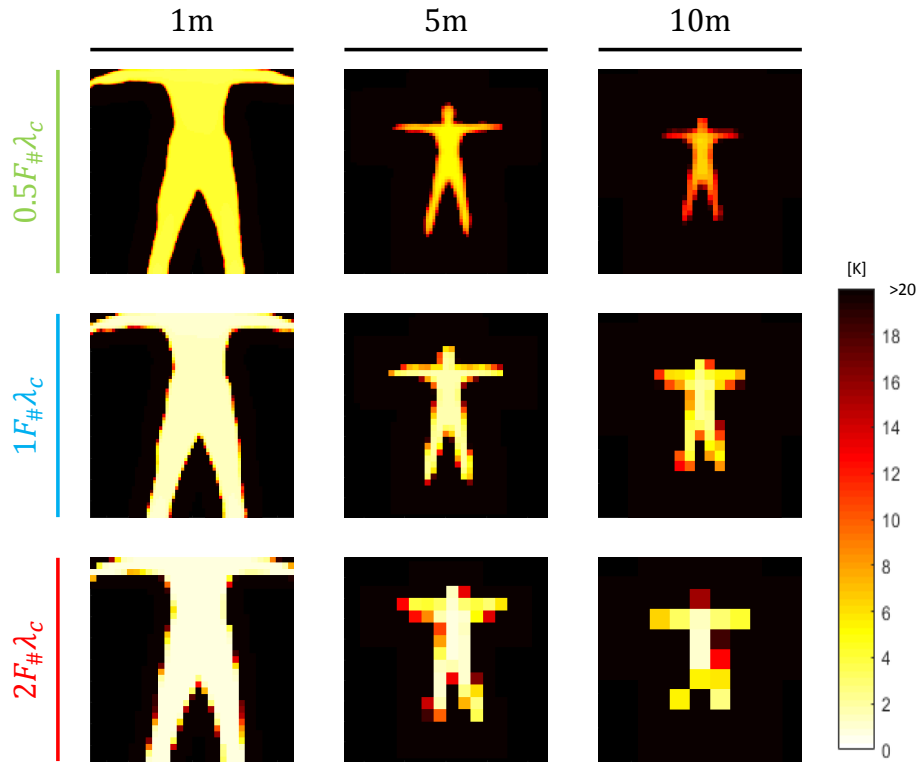

Figure 3.12: Sensitivity of for a pedestrian for power, field and maximum gain sampling for different ranges 1, 5 and 10 meter. Since it is cold, the NETD resolution scale is set on 20 K.

under Rayleigh-Jeans conditions as:

$$NETD^n = \frac{NEP}{k_B \bar{\eta}_{co}^n \bar{\eta}_{sys} \eta_{at} \bar{(R)} \Delta f_{rf}} \frac{1}{\sqrt{\tau_{int}}} \tag{3.3}$$

where $NETD^n$ is the NETD of the n-th feed to the source, $\bar{\eta}_{co}^n$ is the average coupling efficiency over the used bandwidth of n-th feed to the source, $\bar{\eta}_{at}$ is the average atmospheric efficiency over the bandwidth and the average system efficiency is $\bar{\eta}_{sys}(R) = \frac{1}{\Delta f_{rf}} \int_{\Delta f_{rf}} \eta_{sys}(f) df$.

First for cold days, the sensitivity is calculated in Fig. 3.12. Here the sensitivity scale is set on 20 K, as the contrast between the pedestrian and the air can be more than 20 K on cold days. The results show that the pedestrian is distinguishable for all configuration at all distances.

The sensitivity for hot days are found in Fig. 3.13. The sensitivity scale is set to 3 K to represent a hot day where the air temperature is almost as warm as the pedestrian temperature. The results show that for power sampling ($0.5F_{\#}\lambda_c$) the pedestrian is not seen at all; the imager is useless in this configuration. For maximum gain sampling ($2F_{\#}\lambda_c$) the

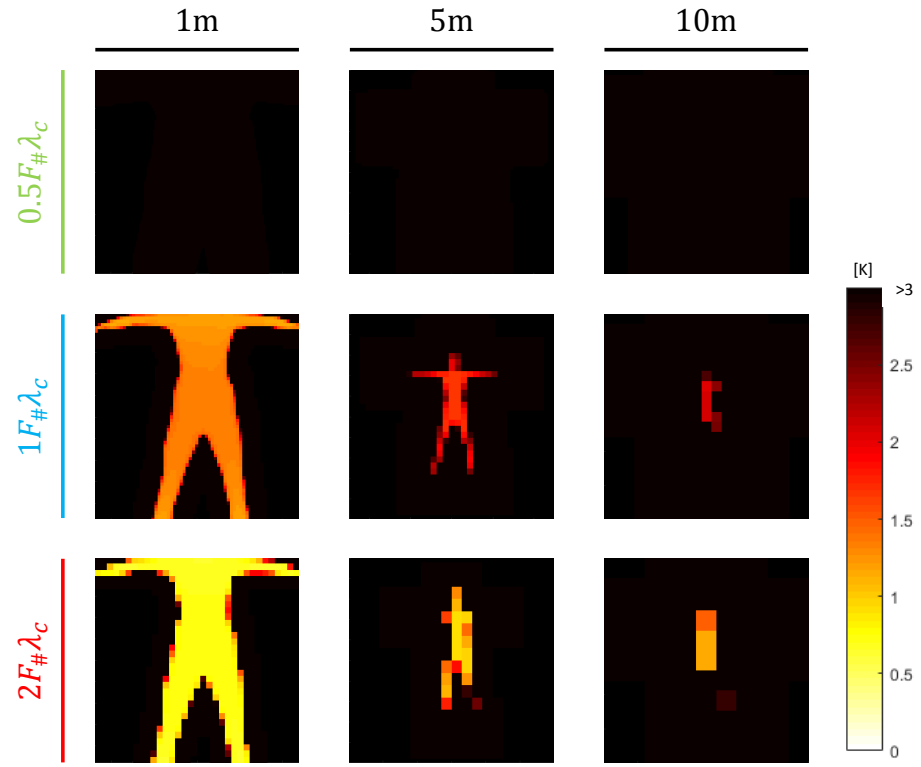

Figure 3.13: Sensitivity of for a pedestrian for power, field and maximum gain sampling for different ranges 1, 5 and 10 meter. Since it is hot, the NETD resolution scale is set on 3 K.

pedestrian is distinguishable, but the angular resolution is really poor for larger distances. This makes that field sampling ($1F_{\#}\lambda_c$) is the best trade-off between angular resolution and distinguishably of the pedestrians.

From Eq. (3.3) it can be found that the average system efficiency needed to achieve sub-kelvin sensitivity at real-time refresh rates is 25.1 %.

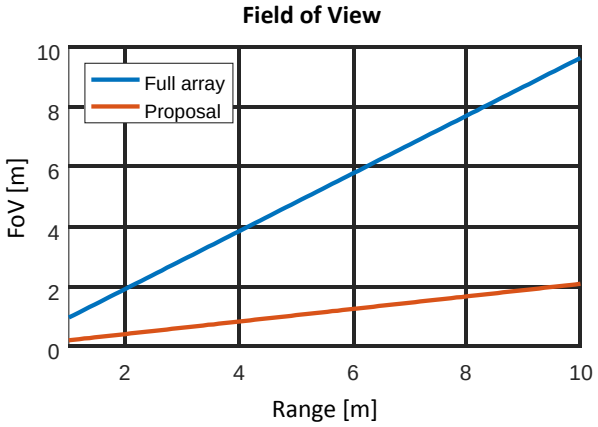

Figure 3.14: Overview of the FoV of the full array compared with the proposed prototype.

3.4 Array Proposal

For the proposal of the array first the sampling has to be determined. As seen in Fig. 3.13, for power sampling ($0.5F_{\#}\lambda_c$) the sensitivity is too low to detect the pedestrian on hot days, the minimal NETD is above 4 degrees which make it impossible for the imager to detect the pedestrians on hot days.

With maximum gain sampling ($2F_{\#}\lambda_c$) the resolution is limited when the pedestrian is at large distances (Fig. 3.6), the resolution can be up to 30 cm which is large compared to a pedestrian. The field sampling ($1F_{\#}\lambda_c$) is a good tradeoff between spatial resolution and sensitivity, which makes it suitable for this application on both cold and hot days. Using the field sampling would mean that 67 by 67 elements can be used to fill the FPA area of 8.9 mm (Table 3.1) for the proposed lens (Diameter 5 cm, $F_{\#} \approx 0.67$). To realize a large array of 67 by 67 elements would be too expensive for a prototype, thus an array of 7 by 7 elements will be designed to give an indication of the expected performance. The performance of the small array can be extrapolated to predict the behavior of the full array.

Since the array is limited in size, the FoV is smaller compared to the full array. The full-array would result in a FoV of 30°, while the prototype will have a FoV of 6.02°. The FoV as function of distance can be found in Fig. 3.14 and the observed contrast and the NETD can be found in Fig. 3.15 and 3.16 respectively.

A summary of the parameters of this array is found in table 3.3. The required performance is to get sub-Kelvin resolution at real-time refresh rate ($\tau_{int} = 0.1\ s$)

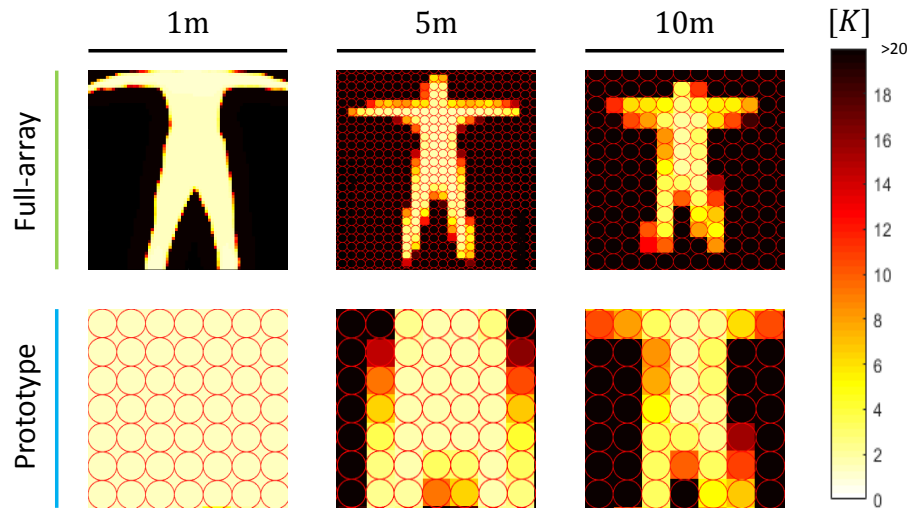

Figure 3.15: Overview of the contrast that is seen by the full array compared to the contrast of the proposed prototype.

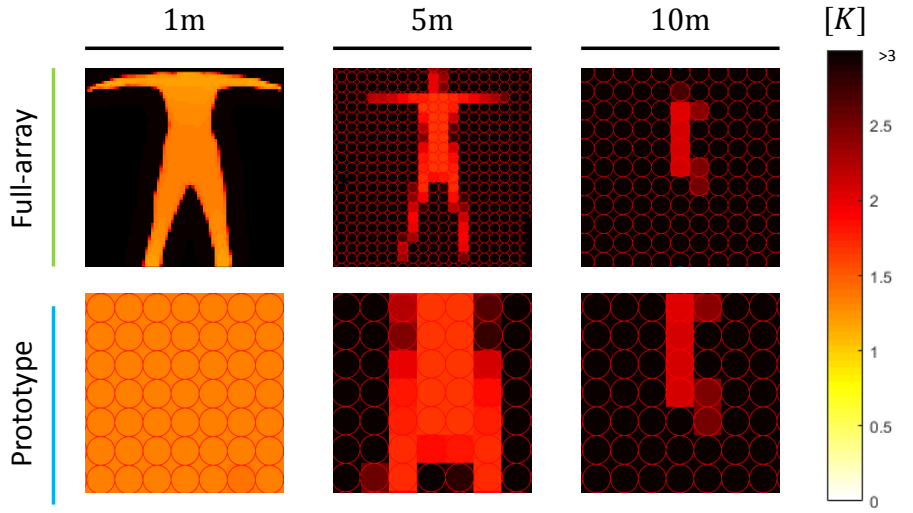

Figure 3.16: Overview of the sensitivity that is seen by the full array compared to the sensitivity of the proposed prototype.

Parameter	Prototype	Full-array
Sampling	$1F_{\#}\lambda_c$	$1F_{\#}\lambda_c$
Number of elements	7×7	67×67
Feed size	132 μm	132 μm
Array size	924 μm $\times$ 924 μm	8844 μm $\times$ 8844 μm
Angular resolution	0.86°	0.86°
Field of View	6.02°	60°
min. $\bar{\eta}_{sys}$	25.1 %	25.1 %

Table 3.3: This table contains the array parameters proposed in this design.

Chapter 4

Quasi-Analytical Model for Array Optimization

This chapter contains an introduction with different existing antenna solutions. Connected arrays are presented as the choice for the antenna. Then an analysis for connected dipoles will be made to conclude with verification of the results.

4.1 Possible Array Architectures

There are different solutions for designing a broadband planar antenna. This section will give some examples and elaborate on their benefits and limitation. For reference, the required relative bandwidth of the system is 1:3 (200 GHz - 600 GHz). All antenna solutions are assumed to be used in combination with dielectric lenses in order to achieve scanning capabilities in an array configuration and to maximize radiation efficiency. Without dielectric lens antennas, surface-waves inside the bulk silicon would introduce unacceptably high losses.

The first possible solution is the spiral [30] or the sinuous antennas [31], found in Fig. 4.1 and 4.2 respectively. Both antennas have a relative bandwidth of 1:6 or even larger. Also their non-directive patterns inside the dielectric lens results in a poor illumination efficiency of the lens due to the high reflections that occur.

Another solution that received a lot of attention is the enhanced leaky-wave solution (Fig. 4.3), having a relative bandwidth of 1:5, examples of those antennas are shown in [32] and [33]. These enhanced leaky-wave solutions are based on implementing an air gap between the antenna and the high permittivity silicon. This introduces an enhanced leaky wave along along the structure that illuminates a dielectric lens much more efficiently

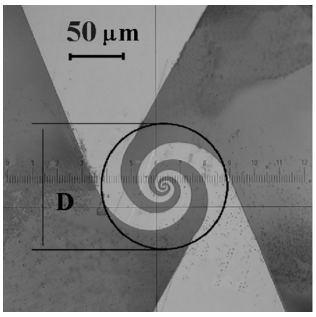

Figure 4.1: SP2 log-spiral antenna, the dark color represents the substrate [30].

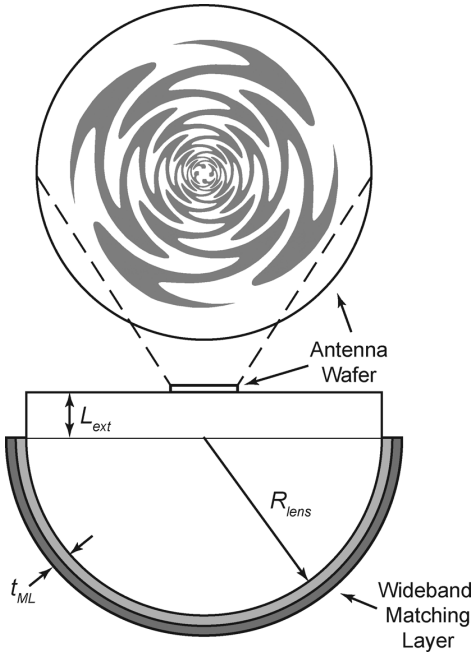

Figure 4.2: Dual-polarized sinuous antenna placed on an extended hemispherical dielectric lens with a wideband match layer; the dark color represents the metal of the antenna [31].

towards the top part of the lens over a very large bandwidth [34]. The CMOS stratification used (Appendix A) shows that it is not possible to use an air gap here. However, there is a layer SiO_2 available, which has a lower permittivity than silicon, inducing a slight enhanced leaky-wave behavior. Since the permittivity of SiO_2 (i.e. $\epsilon_r = 4.2$) is higher than air, an efficient illumination of the lens over a relative bandwidth of 1:5 cannot be reached in this CMOS stratification.

It has been shown that also double-slot type configurations can be used to make a relatively bandwidth of 1:2 [35] or 1:3 [36] (see also Fig. 4.4).

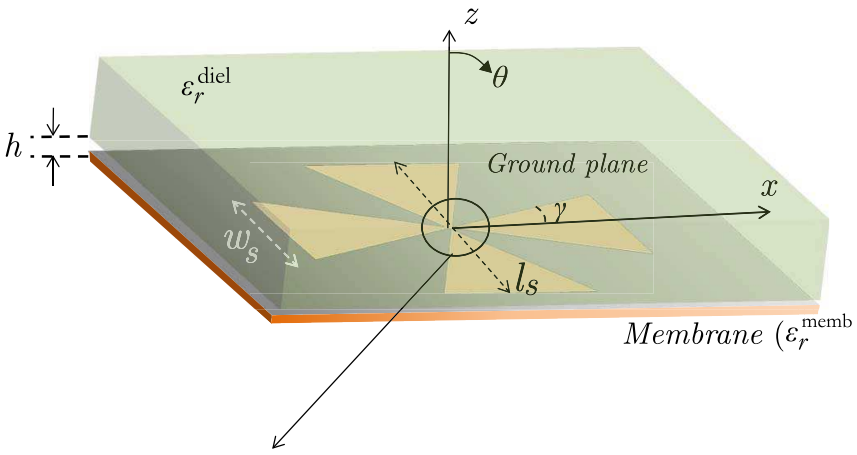

Figure 4.3: Schematic overview of a dual-polarized leaky lens antenna. The antenna is placed under a silicon dielectric separated by an air gap of height h from the antenna plane [32].

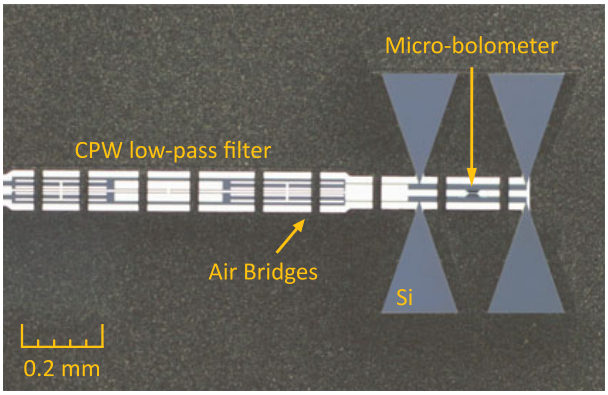

Figure 4.4: Schematic overview of the double bow-tie slot antenna with a coplanar waveguide low-pass filter [36].

From chapter 3, field sampling ($d_f = 1F_{\#}\lambda_c$) was identified as the best tradeoff. For this reason, leaky-lens antenna and the double slot antenna are not viable solutions, as they are both too large for this sampling with a $F_{\#}$ of 0.67.
Connected arrays were introduced in [37], having the objective to increase the bandwidth of dipole arrays. After this, arrays of connected elements are investigated further in literature, for example in [38], [39] and [40]. Connected arrays are promising on their performance in terms of bandwidth, low cross polarization due to planar currents, wide-scanning application. In this thesis, especially the broadband behavior is of interest, phased scanning is not needed since a FPA in combination with optics will sample the FoV of interest.

In [41] it is seen that an array of connected elements is excited coherently to form a

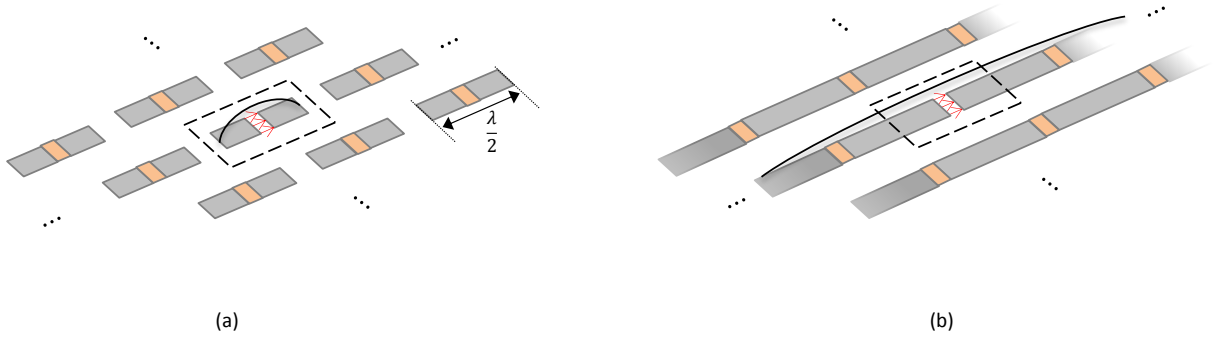

Figure 4.5: Current distribution along the structures. The current distribution along the dipole is indicated by the black lines; only the centered unit cell (dashed square) is excited and the other gaps are indicated with orange: (a) Half-wavelength dipole array, here the current distribution that is supported is a resonant sinusoidal distribution along the dipole. (b) Array of connected dipoles, here the supported current distribution is approximately flat along the dipole.

single radiation beam outside the lens. Unlike the coherent connected array in [41], in the design that is considered here the elements are not fed in phase and are independent from each other. This configuration corresponds to the case where each element is associated with a radiation beam in an imaging array configuration [33].

Figure 4.5 depicts the concept on which connected arrays are based on. In an imaging array, only the element under consideration is active, while the neighboring elements are terminated on passive resistors. The current distribution on a resonant dipole, as shown in Fig. 4.5(a), is sinusoidal and frequency dependent. When connecting the elements as in Fig. 4.5(b), the current is allowed to flow from the active element to the adjacent one and is attenuated due dissipation in the passive element loads. This effectively results in a less resonant current profile that is associated to wideband behavior.

It can be seen that for the connected array the current flows along the whole dipole. This creates a broadband behavior to make it more directive than the resonant element array. More power will be captured by the neighboring elements, decreasing the mutual coupling efficiency. The design will be a trade-off between directivity and mutual coupling between the elements.

A model is derived to analyze connected elements (both dipoles and slots) for the performance in terms of mutual coupling and radiated far field.

Since the array of elements is placed under a lens, the focal number of the lens has influence on both performance parameters. Consider two lenses, one with a low focal number and one with a higher focal number, Fig. 4.6 (a) and (b) respectively. For lenses with small focal numbers the truncation angle is high ($\theta_0 = \sin^{-1}\left(\frac{1}{2F_\#}\right)$), which gives a low spillover

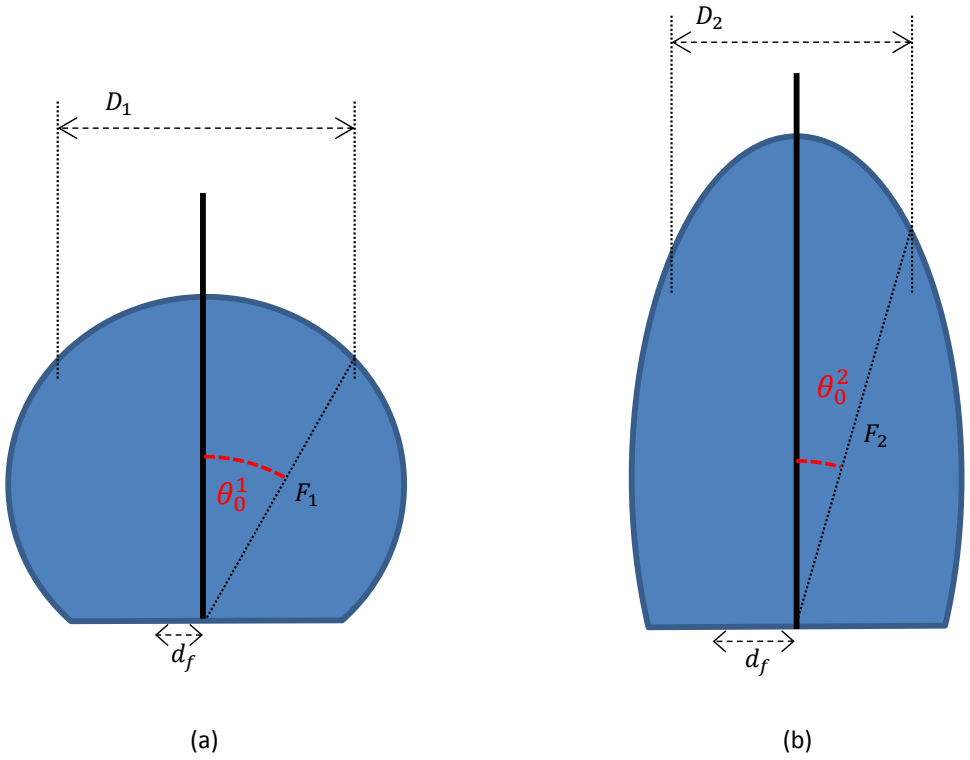

Figure 4.6: Geometry lenses with different focal number.Two configurations of lenses with different focal numbers (F/D). (a): A lens with a low focal number, having a large truncation angle θ_0^1 and a dense spacing between elements d_f. (b) A lens with a higher focal number, having a smaller truncation angle θ_0^2 and a sparser spacing between elements.

of radiated power. Also the elements are spaced more dense here ($d_f = F_{\#}\lambda_c$), causing the mutual coupling between the element to be stronger. When the focal number is higher, the truncation angle is smaller, which results in more spillover of radiated power. Moreover, the elements are more spaced from each other, reducing the mutual coupling. Both term cannot be optimized at the same time and thus a tradeoff has to be made between the two configurations to find an optimum.

To find this optimum a model is derived for a single connected dipole element per pixel and for 2 by 2 connected dipole subarray of elements per pixel, as it can be seen in Fig. 4.7 and in Fig. 4.8, respectively. To analysis the performance, both the radiation from a single element and the 2 by 2 elements are evaluated using the connected array spectral domain methods [42].

To find an optimal configuration for the pixel radiating element, a single dipole array, double dipole array, single slot array and double slot array are considered in Fig. 4.7, 4.8, 4.9 and 4.10, respectively. The initial situation considers 7 by 7 pixels. For the first

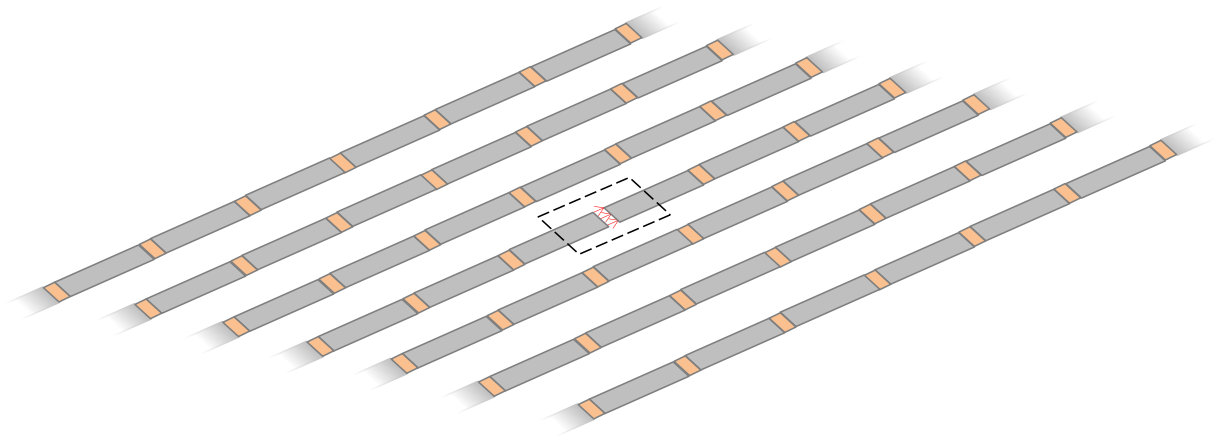

Figure 4.7: Schematic overview of an 7 by 7 array of connected dipoles using a single row. A fed pixel cell is indicated by the black square in the center of the array, the rest of the gaps are indicated with orange.

analysis of the arrays, only one row of the mentioned pixels will be considered. This can influence the total efficiency due to mutual coupling, but this aspect will be investigated later. First the Electric Field Integral Equations (EFIE) are solved for the dipoles and the Magnetic Field Integral Equations (MFIE) are solved for slots. In the next section, a connected array of dipoles is analyzed.

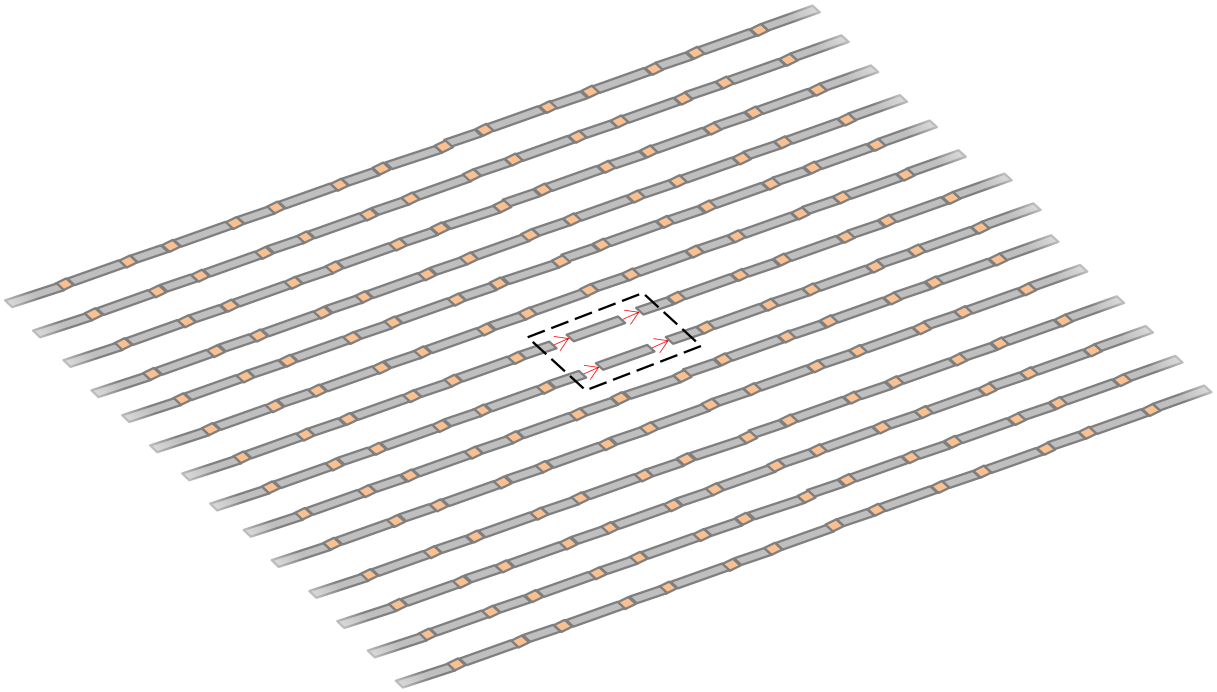

Figure 4.8: Schematic overview of an 7 by 7 array of connected dipoles using double rows. A fed pixel cell is indicated by the black square in the center of the array, the rest of the gaps are indicated with orange.

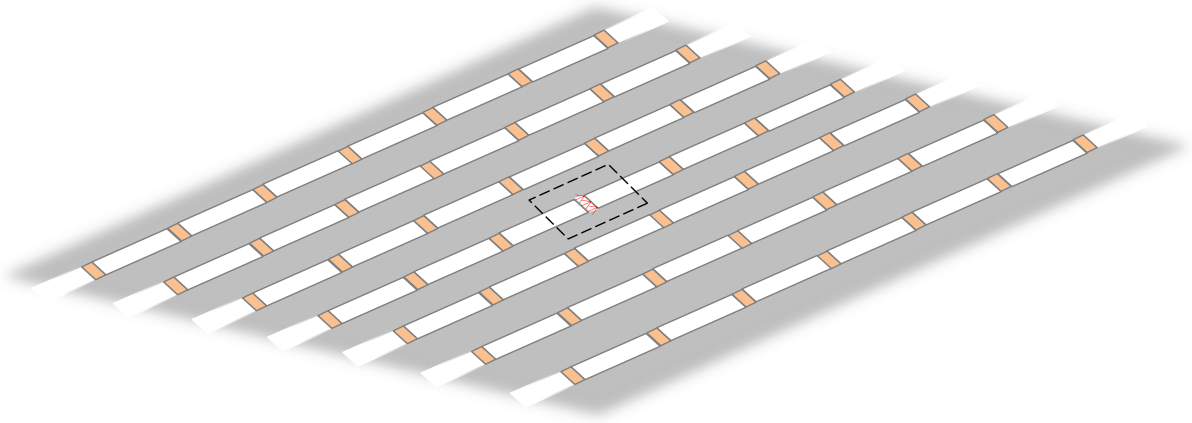

Figure 4.9: Schematic overview of an 7 by 7 array of connected slots using a single row. A fed pixel cell is indicated by the black square in the center of the array, the rest of the gaps are indicated with orange.

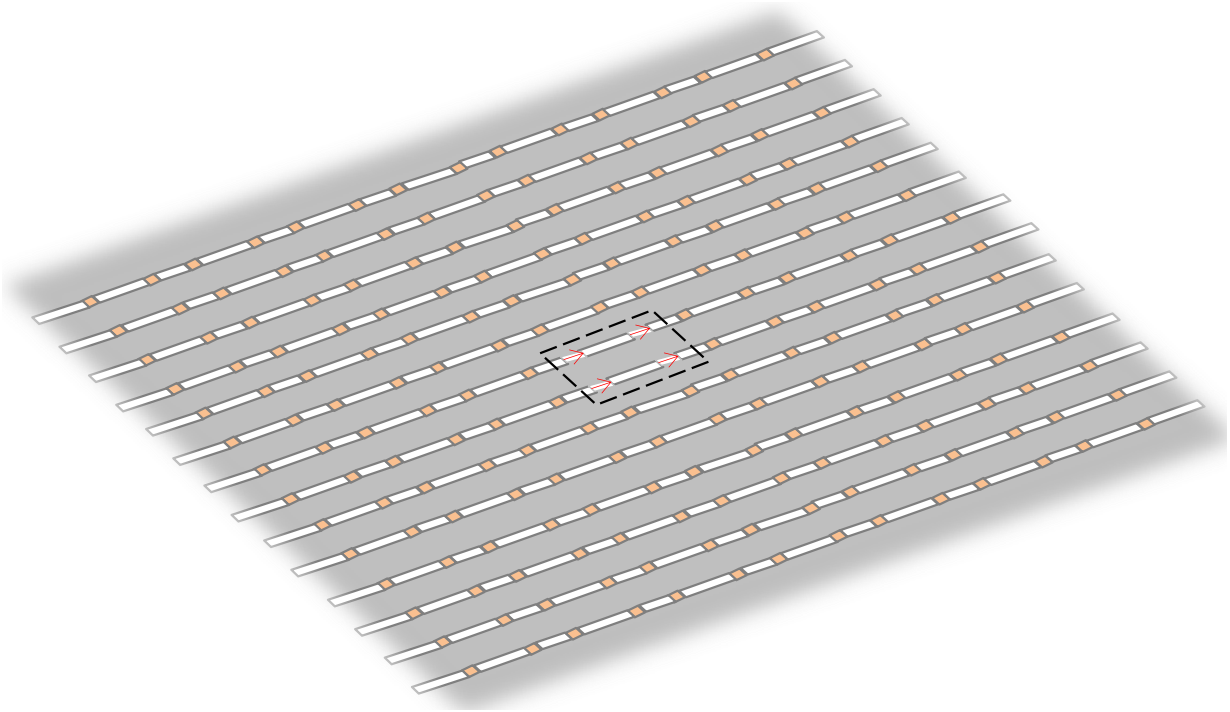

Figure 4.10: Schematic overview of an 7 by 7 array of connected slots using double rows. A fed pixel cell is indicated by the black square in the center of the array, the rest of the gaps are indicated with orange.

4.2 Array of Connected Dipoles

In this section, an analysis of connected dipoles is presented. Expressions for the current distribution, the input impedances and far field are derived. Such formulas can be used to evaluate the performance of the array in terms of efficiency, mutual coupling and radiation characteristics.

4.2.1 Surface Currents

Before being able to solve the EFIE for a dipole, we have to use the equivalence principle that defines a problem with equivalent surface currents that flow on the dipole. For this analysis, the topology from Fig. 4.11 is used. Figure 4.11(a) depicts the dipole fed in two locations. Using the equivalence theorem for the surface around the dipole, S, electric and magnetic surface currents can be defined (Fig. 4.11 (b)). Image theorem can then be used to remove the metal of the dipole and remain with equivalent surface currents in free space (Fig. 4.11 (c)).

To find out which surface currents are present on the surface on the dipole S, the equivalent electric and magnetic currents are expressed as respectively:

$$\vec{j}_s = \hat{n} \times \vec{h} \tag{4.1}$$

$$\vec{m}_s = -\hat{n} \times \vec{e} \tag{4.2}$$

where $\hat{n}$ is the normal on the surface S; $\vec{e}$ and $\vec{h}$ are the total electric field and total magnetic field present on the location of the surface.

On the metal of the dipole, the metal is a perfect electric conductor (PEC), which makes the present electric field zero; no present magnetic surface currents.

Observing *on the gaps* sees that the electric field is continuous through the gaps; the equivalent magnetic surface currents on the upside and downside are equal but in opposite direction (Eq. (4.2)), which makes them cancel out. To conclude, no magnetic current are observed.

For the electric currents, following Eq. (4.1) to find the electric current on the upside of S as $\vec{j}_s(z = 0^+) = \hat{z} \times \vec{H}(z = 0^+)$ and for the current on the downside of S as $\vec{j}_s(z = 0^-) = -\hat{z} \times \vec{H}(z = 0^-)$. For thin dipoles, taking the total current as $\vec{j} = \vec{j}_s(z = 0^+) + \vec{j}_s(z = 0^-)$.

Now the analysis for the single and double dipole will be made.

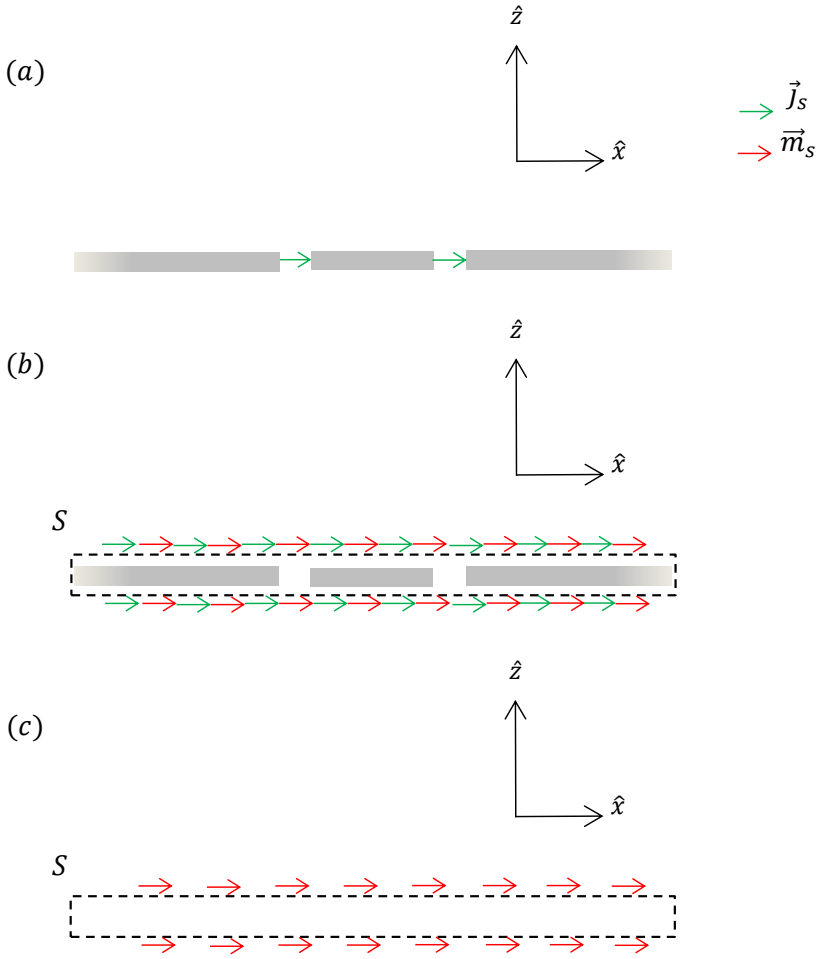

Figure 4.11: Schematic overview of a double fed dipole with equivalent surface currents. (a) Initial situation of a dipole, fed at two location by an electric field. (b) Defined equivalent surface, S, along the dipole, with equivalent electric and magnetic surface currents. (c) Equivalent surface, S, equivalent electric and magnetic surface currents in free space.

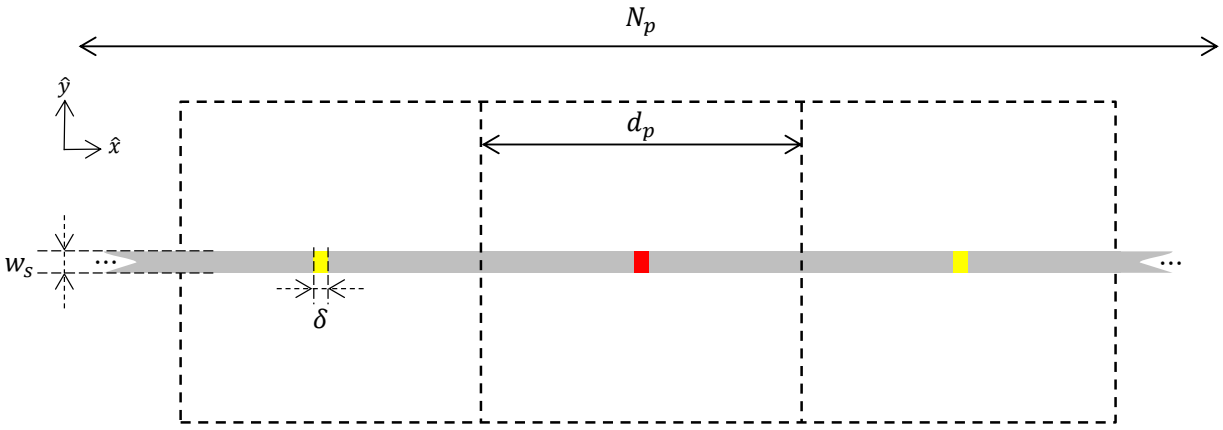

Figure 4.12: Geometric configuration of the single dipole with 1 delta-gap per unit cell. The distance d_p denotes the unit cell length, N_p is the total number of unit cells (odd), w_s is the width of the dipole and δ is the width of the delta-gap feed.

4.2.2 Single Dipole Analysis

The analysis of the single fed dipole follows the geometry given by Fig. 4.12, were N_p is chosen to be odd, this way the focal plane array has a pixel cell in middle of the array and in the focus of the lens. For this dipole the Electic Field Integral Equation is:

$$\vec{e}_{tot}(x,y,z) = \vec{e}_{scat}(x,y,z) + \vec{e}_{inc}(x,y,z) \tag{4.3}$$

where $\vec{e}_{tot}$ is the total electric field; $\vec{e}_{scat}$ is the scattered electric field and $\vec{e}_{inc}$ is the incident electric field. It is assumed that the dipole is infinitely thin and observed at the z-location of the dipole ($z = 0$), which makes Eq. (4.3) become:

$$\vec{e}_{tot}(x,y) = \vec{e}_{scat}(x,y) + \vec{e}_{inc}(x,y)\,. \tag{4.4}$$

Assuming the dipole is electrically narrow, the only relevant component of the electric field is along the dipole (x-direction). The incident field observed on the dipole ($y = 0$) can be written as:

$$\vec{e}_{inc}(x) = \frac{V_0}{\delta}\mathrm{rect}_\delta(x)\hat{x} \tag{4.5}$$

where V_0 is the feeding voltage. The total electric field is the product between the surface impedance (Z_l on the gaps and zero everywhere else) and the spatial surface current on the dipole surface:

$$\vec{e}_{tot}(x) = \frac{Z_l}{\delta}\sum_{n_p=-(N_p-1)/2}^{(N_p-1)/2} i_{\delta,n_p}\mathrm{rect}_\delta(x - n_p d_p) \tag{4.6}$$

with i_{δ,n_p} is the average electric current on delta gap with index n_p. The scattered electric field is equal to the convolution of the spatial electric current distribution $j_x(x',y')$ (which is only along $\hat{x}$) and the spatial Green's Function (EJ), g_{xx}^{EJ} , as:

$$\vec{e}_{scat}(x) = \int_{-\infty}^{\infty}\int_{-\infty}^{\infty} g_{xx}^{EJ}(x-x',y-y')j_x(x',y')dx'dy' \,. \tag{4.7}$$

The spatial electric current distribution is assumed to be the product of the longitudinal distribution, $i(x')$, and the transverse edge-singular distribution, $j_t(y')$, to find ,by the steps from Appendix B.1, the longitudinal spectral Green's function as:

$$D(k_x) = \frac{1}{2\pi}\int_{-\infty}^{\infty} G_{xx}^{EJ}(k_x,k_y)J_0\left(\frac{k_y w_s}{2}\right)dk_y \,. \tag{4.8}$$

The calculation of the spectral Green's Functions for stratified media is explained in Appendix C. Using the identity:

$$\frac{\mathrm{rect}_\delta(x-\alpha)}{\delta} = \frac{1}{2\pi}\int_{-\infty}^{\infty}\mathrm{sinc}\left(\frac{k_x\delta}{2}\right)e^{-jk_x(x-\alpha)}dk_x \tag{4.9}$$

we can write the EFIE from Eq. (4.4) as:

$$\int_{-\infty}^{\infty} I(k_x)D(k_x)e^{-jk_x x}dk_x = \int_{-\infty}^{\infty}\left(\mathrm{sinc}\left(\frac{k_x\delta}{2}\right)\left(-V_0 + Z_l\sum_{n_p=-(N_p-1)/2}^{(N_p-1)/2} i_{\delta,n_p}e^{jk_x n_p d_p}\right)\right)e^{-jk_x x}dk_x \tag{4.10}$$

where $I(k_x)$ is the current spectrum. Since this equation must be valid for every position x along the dipole, the integrands have to be equal, to write the current spectrum as:

$$I(k_x) = \frac{\mathrm{sinc}\left(\frac{k_x\delta}{2}\right)}{D(k_x)}\left(-V_0 + Z_l\sum_{n_p=-(N_p-1)/2}^{(N_p-1)/2} i_{\delta,n_p}e^{jk_x n_p d_p}\right) . \tag{4.11}$$

By taking the inverse Fourier transform from this spectrum, the average current along the gap n_p' can be found as:

$$i_{\delta,n_p'} = \frac{1}{\delta}\int_{n_p' d_p-\delta/2}^{n_p' d_p+\delta/2} i(x)dx = \frac{1}{\delta}\int_{n_p' d_p-\delta/2}^{n_p' d_p+\delta/2}\frac{1}{2\pi}\int_{-\infty}^{\infty} I(k_x)e^{-jk_x x}dk_x dx \tag{4.12}$$

and

$$i_{\delta,n_p'} = \frac{1}{2\pi}\int_{-\infty}^{\infty}\frac{\mathrm{sinc}^2\left(\frac{k_x\delta}{2}\right)}{D(k_x)}\left(-V_0 + Z_l\sum_{n_p=-(N_p-1)/2}^{(N_p-1)/2} i_{\delta,n_p}e^{jk_x n_p d_p}\right)e^{-jk_x n_p' d_p}dk_x \,. \tag{4.13}$$

Defining the mutual admittance between unit cell n_p and n'_p as:

$$Y_{n_p,n'_p} = -\frac{1}{2\pi}\int_{-\infty}^{\infty} \frac{\operatorname{sinc}^2\left(\frac{k_x\delta}{2}\right)}{D(k_x)} e^{-jk_x\left(n_p-n'_p\right)d_p} \tag{4.14}$$

and substituting it in Eq. (4.13), we obtain:

$$i_{\delta,n'_p} = V_0 Y_{0,n'_p} - Z_l \sum_{n_p=-(N_p-1)/2}^{(N_p-1)/2} i_{\delta,n_p} Y_{n_p,n'_p}\,. \tag{4.15}$$

This can be written as a system of equations, calculating the current in each gap as:

$$\boldsymbol{I}\boldsymbol{i}_\delta = \boldsymbol{Y}\boldsymbol{v} - Z_l\boldsymbol{Y}\boldsymbol{i}_\delta \tag{4.16}$$

where $\boldsymbol{I}$ is an identity matrix of order N_p; $\boldsymbol{i}_\delta$ is the current vector; $\boldsymbol{Y}$ is the admittance matrix and $\boldsymbol{v}$ is the voltage vector (feeding), defined as:

$$\boldsymbol{i_\delta} = \begin{bmatrix} i_{\delta,-\frac{(N_p-1)}{2}} \\ \vdots \\ i_{\delta,\frac{(N_p-1)}{2}} \end{bmatrix} \tag{4.17}$$

$$\boldsymbol{Y} = \begin{bmatrix} Y_{-\frac{N_p-1}{2},-\frac{N_p-1}{2}} & \dots & Y_{-\frac{N_p-1}{2},\frac{N_p-1}{2}} \\ \vdots & \ddots & \vdots \\ Y_{\frac{N_p-1}{2},-\frac{N_p-1}{2}} & \dots & Y_{\frac{N_p-1}{2},\frac{N_p-1}{2}} \end{bmatrix} \tag{4.18}$$

$$\boldsymbol{v} = \begin{bmatrix} 0 \\ \vdots \\ V_0 \\ \vdots \\ 0 \end{bmatrix}\,. \tag{4.19}$$

This system of equations can be solved for $\boldsymbol{i}_\delta$ as:

$$\boldsymbol{i}_\delta = [\boldsymbol{Y}^{-1} + Z_l\boldsymbol{I}]^{-1}\boldsymbol{v}\,. \tag{4.20}$$

The active input impedance of the port n_p is then defined as:

$$Z_{in,active} = \frac{v_{n_p}}{i_{\delta,n_p}} - Z_l\,. \tag{4.21}$$

The mutual coupling efficiency, η_{mc} , is the ratio between the power radiated by the fed unit cell, P_{rad}, and the total power P_{tot} (P_{rad} plus the power induced in all other present unit cells, P_{mc}):

$$\eta_{mc} = \frac{P_{rad}}{P_{rad}+P_{mc}}\,. \tag{4.22}$$

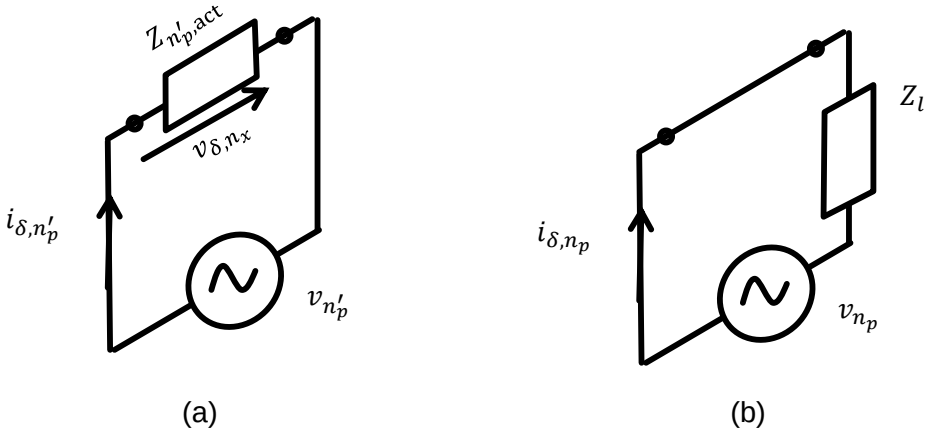

Figure 4.13: Circuits that are used for the calculation of the power in the gaps of the dipole: (a) The equivalent circuit for the fed delta-gap. (b) The equivalent circuit used for all non-fed delta-gaps.

To calculated the power in all elements, the equivalent circuit of Fig. 4.13 is used. In Eq. (4.22) the total power is defined as:

$$P_{tot} = \frac{|i_{\delta,0}|^2}{2} Re\{Z_{0,act}\} \tag{4.23}$$

and the induced power as:

$$P_{mc} = Re\{Z_l\} \sum_{\substack{n_p = -\frac{N_p-1}{2} \\ n_p \neq 0}}^{(N_p-1)/2} \frac{|i_{\delta,n_p}|^2}{2} . \tag{4.24}$$

To complete this analysis, the same steps are performed for a double fed dipole.

4.2.3 Double Dipole Analysis

The analysis of the double fed double dipole follows the geometry given by Fig. 4.14, were N_p is chosen to be odd, this way the focal plane array has a unit cell in middle of the array and in the focus of the lens. The distance between the dipoles d_s and the distance between the delta gaps on the same dipole of the same unit cell d_δ are set to be equal.

For this configurations the EFIE is the same as for the single dipole (Eq. (4.3)). It is assumed that the dipoles are infinitely thin and observed at the z-location of the dipoles ($z = 0$), then the EFIE is equal to the one in Eq. (4.4).

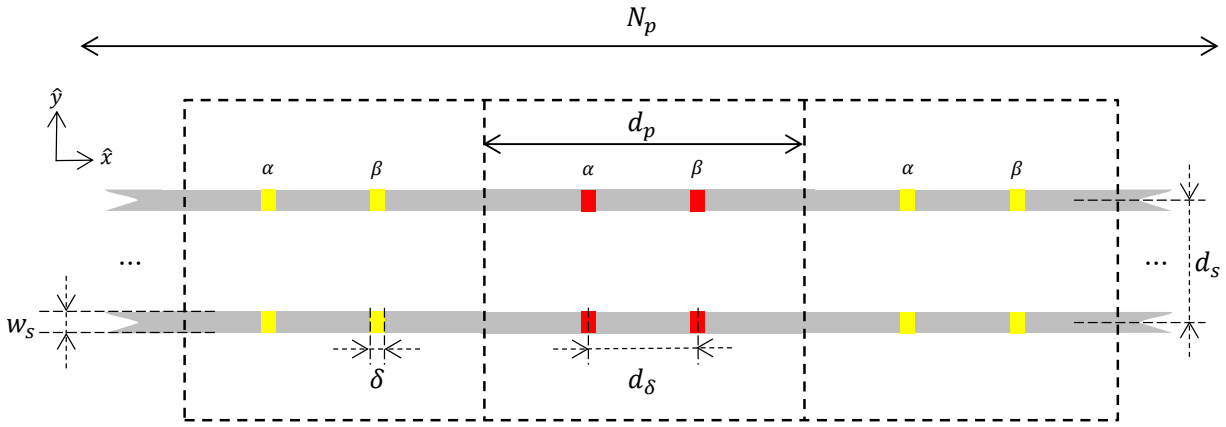

Figure 4.14: Geometric configuration of the double dipole with 2 delta-gap per unit cell per dipole. The distance d_p denotes the unit cell length, N_p is the total number of unit cells (odd), w_s is the width of the dipoles and δ is the width of the delta-gap feeds, d_s is the distance between the dipoles and d_δ is the distance between the delta gaps on the same dipole of the same unit cell.

Assuming the dipoles are electrically narrow, the only relevant component of the electric field is along the dipoles (x-direction), the incident field observed on the dipoles can be written as:

$$\vec{e}_{inc}(x,y) = \frac{V_0}{\delta} \underbrace{\sum_{n_\delta \in \{-1,1\}} \text{rect}_\delta\left(x + n_\delta \frac{d_\delta}{2}\right)}_{\text{double gap}} \underbrace{\sum_{n_s \in \{-1,1\}} \text{rect}_{w_s}\left(y - n_s \frac{d_s}{2}\right)}_{\text{double dipole}} \hat{x} \tag{4.25}$$

where V_0 is the feeding voltage. The total electric field is the product between the surface impedance (Z_l on the gaps and zero everywhere else) and the spatial surface current on the dipoles:

$$\vec{e}_{tot}(x) = \frac{Z_l}{\delta} \sum_{n_p=-(N_p-1)/2}^{(N_p-1)/2} \left[i^\alpha_{\delta,n_p} \text{rect}_\delta\left(x - n_p d_p + \frac{d_\delta}{2}\right) + i^\beta_{\delta,n_p} \text{rect}_\delta\left(x - n_p d_p - \frac{d_\delta}{2}\right) \right] \sum_{n_s \in \{-1,1\}} \text{rect}_{w_s}\left(y - n_s \frac{d_\delta}{2}\right) \tag{4.26}$$

with i^α_{δ,n_p} and i^β_{δ,n_p} is the average electric current in unit cell n_p of gap α and β respectively. The currents are excited in phase and since only two dipoles are present, the currents do not depend on the dipole on which they are observed on, but do depend on the unit cell.

The scattered electric field is equal to the convolution of the spatial electric current distribution $j_x(x',y')$ (which is only along $\hat{x}$) and the spatial Green's Function (EJ), g^{EJ}_{xx} ,

from both dipoles as:

$$\vec{e}_{scat}(x) = \sum_{n_s \in \{-1,1\}} \int_{-\infty}^{\infty} \int_{-\infty}^{\infty} g_{xx}^{EJ}(x-x', y-y') j_x(x', y' - n_s \frac{d_s}{2}) dx' dy' \,. \tag{4.27}$$

The spatial electric current distribution is assumed to be the product of the longitudinal distribution, $i(x')$, and the transverse edge-singular distribution, $j_t(y')$, to find, by following the steps from Appendix B.2, the longitudinal spectral Green's function as:

$$D(k_x) = \frac{1}{2\pi} \int_{-\infty}^{\infty} G_{xx}^{EJ}(k_x, k_y) J_0\left(\frac{k_y w_s}{2}\right) \left[1 + e^{-jk_y d_s}\right] dk_y \,. \tag{4.28}$$

where we assume the observation is at $y = \frac{d_s}{2}$.

The method to calculated the spectral Green's functions for stratified media is found in Appendix C. To write the EFIE from Eq. (4.4) with Eq. (4.25), (4.26) and (4.27) and using the identity from Eq. (4.9) as:

$$\begin{aligned} \int_{-\infty}^{\infty} I(k_x) D(k_x) e^{-jk_x x} dk_x = \\ \int_{-\infty}^{\infty} \operatorname{sinc}\left(\frac{k_x \delta}{2}\right) \Bigg(- V_0 \left[e^{-jk_x d_\delta} + e^{jk_x d_\delta}\right] \\ + Z_l \sum_{n_p=-(N_p-1)/2}^{(N_p-1)/2} \left[i_{\delta,n_p}^{\alpha} e^{-\frac{jk_x d_\delta}{2}} + i_{\delta,n_p}^{\beta} e^{\frac{jk_x d_\delta}{2}}\right] e^{jk_x n_p d_p} \Bigg) e^{-jk_x x} dk_x \end{aligned} \tag{4.29}$$

where $I(k_x)$ is the current spectrum. This integral must be valid for every position x along the dipoles, the integrands must be equal this gives the current spectrum as:

$$I(k_x) = \frac{\operatorname{sinc}\left(\frac{k_x \delta}{2}\right)}{D(k_x)} \left(-2V_0 \cos\left(k_x d_\delta\right) + Z_l \sum_{n_p=-(N_p-1)/2}^{(N_p-1)/2} \left[i_{\delta,n_p}^{\alpha} e^{-\frac{jk_x d_\delta}{2}} + i_{\delta,n_p}^{\beta} e^{\frac{jk_x d_\delta}{2}}\right] e^{jk_x n_p d_p} \right) \tag{4.30}$$

By taking the inverse Fourier transform from this spectrum, the average current along α and β of gap with index n_p' can be found as:

$$i_{\delta,n_p'}^{\alpha} = \frac{1}{\delta} \int_{n_p' d_p - \frac{d_\delta}{2} - \delta/2}^{n_p' d_p - \frac{d_\delta}{2} + \delta/2} i(x) dx = \frac{1}{\delta} \int_{n_p' d_p - \frac{d_\delta}{2} - \delta/2}^{n_p' d_p - \frac{d_\delta}{2} + \delta/2} \frac{1}{2\pi} \int_{-\infty}^{\infty} I(k_x) e^{-jk_x x} dk_x dx \tag{4.31}$$

and

$$i_{\delta,n_p'}^{\beta} = \frac{1}{\delta} \int_{n_p' d_p + \frac{d_\delta}{2} - \delta/2}^{n_p' d_p + \frac{d_\delta}{2} + \delta/2} i(x) dx = \frac{1}{\delta} \int_{n_p' d_p + \frac{d_\delta}{2} - \delta/2}^{n_p' d_p + \frac{d_\delta}{2} + \delta/2} \frac{1}{2\pi} \int_{-\infty}^{\infty} I(k_x) e^{-jk_x x} dk_x dx \,. \tag{4.32}$$

The construction of the admittance matrix is found in Appendix B.3. Using the equations found, a set systems of equations can be made:

$$\boldsymbol{I}\boldsymbol{i}_\delta = \boldsymbol{Y}\boldsymbol{v} - Z_l\boldsymbol{Y}\boldsymbol{i}_\delta \tag{4.33}$$

where $\boldsymbol{I}$ is an identity matrix of order $2N_p$; $\boldsymbol{i}_\delta$ is the current vector; $\boldsymbol{Y}$ is the admittance matrix and $\boldsymbol{v}$ is the voltage vector (feeding), as:

$$\boldsymbol{i_\delta} = \begin{bmatrix} \boldsymbol{i}_{\delta,\alpha} \\ \boldsymbol{i}_{\delta,\beta} \end{bmatrix} \text{ with } \quad \boldsymbol{i}_{\delta,\alpha} = \begin{bmatrix} i^{\alpha}_{\delta,-\frac{N_p-1}{2}} \\ \vdots \\ i^{\alpha}_{\delta,\frac{N_p-1}{2}} \end{bmatrix} \text{ and } \quad \boldsymbol{i}_{\delta,\beta} = \begin{bmatrix} i^{\beta}_{\delta,-\frac{N_p-1}{2}} \\ \vdots \\ i^{\beta}_{\delta,\frac{N_p-1}{2}} \end{bmatrix} \tag{4.34}$$

$$\boldsymbol{Y} = \begin{bmatrix} \boldsymbol{Y}^{\alpha\alpha} & \boldsymbol{Y}^{\alpha\beta} \\ \boldsymbol{Y}^{\beta\alpha} & \boldsymbol{Y}^{\beta\beta} \end{bmatrix} \text{ with } \quad \boldsymbol{Y}^{i,j} = \begin{bmatrix} Y^{ij}_{-\frac{N_p-1}{2},-\frac{N_p-1}{2}} & \cdots & Y^{ij}_{-\frac{N_p-1}{2},\frac{N_p-1}{2}} \\ \vdots & \ddots & \vdots \\ Y^{ij}_{\frac{N_p-1}{2},-\frac{N_p-1}{2}} & \cdots & Y^{ij}_{\frac{N_p-1}{2},\frac{N_p-1}{2}} \end{bmatrix} \tag{4.35}$$

$$\boldsymbol{v} = \begin{bmatrix} \boldsymbol{v}^{\alpha} \\ \boldsymbol{v}^{\beta} \end{bmatrix} \text{ with} \boldsymbol{v}^{\alpha} = \boldsymbol{v}^{\beta} \begin{bmatrix} 0 \\ \vdots \\ V_0 \\ \vdots \\ 0 \end{bmatrix} \tag{4.36}$$

This system of equations can be solved for $\boldsymbol{i}_\delta$ as:

$$\boldsymbol{i}_\delta = [\boldsymbol{Y}^{-1} + Z_l\boldsymbol{I}]^{-1}\boldsymbol{v}\,. \tag{4.37}$$

The active input impedance of the port n_p is then defined as:

$$Z_{in,active} = \frac{v_{n_p}}{i_{\delta,n_p}} - Z_l\,. \tag{4.38}$$

The mutual coupling efficiency, η_{mc} , is the ratio between the power radiated by the fed unit cell, P_{rad}, and the total power P_{tot}(P_{rad} plus the power induced in all other present unit cells, P_{mc}):

$$\eta_{mc} = \frac{P_{rad}}{P_{rad} + P_{mc}}\,. \tag{4.39}$$

In Eq. (4.39) the total power is defined as:

$$P_{tot} = \frac{\left(|i^{\alpha}_{\delta,0}|^2 + |i^{\beta}_{\delta,0}|^2\right)}{2} Re\{Z_{in,active}\} \tag{4.40}$$

And the induced power as:

$$P_{mc} = Re\{Z_l\} \sum_{\substack{n_p = -\frac{N_p-1}{2} \\ n_p \neq 0}}^{(N_p-1)/2} \frac{\left(|i^{\alpha}_{\delta,n_p}|^2 + |i^{\beta}_{\delta,n_p}|^2\right)}{2}. \tag{4.41}$$

4.2.4 Far Field of Dipole Structures

To find the electric far field radiated by a dipole structure, the asymptotic evaluation is used:

$$\vec{E}_{far}\left(\vec{r}_{obs}\right) = jk_{zs} \begin{bmatrix} G^{EJ}_{xx}\left(k_{xs}, k_{ys}, z_{obs}, z'\right) \\ G^{EJ}_{yx}\left(k_{xs}, k_{ys}, z_{obs}, z'\right) \\ G^{EJ}_{zx}\left(k_{xs}, k_{ys}, z_{obs}, z'\right) \end{bmatrix} I(k_{xs}) J_t(k_{ys}) e^{jk_{zs}|z_{obs}-z|} AF \frac{e^{-jkr}}{2\pi r} \tag{4.42}$$

where $\vec{r}_{obs}$ is the location of observation; $I(k_{xs})$ is the current spectrum (Eq. (4.11) for a single dipole and Eq. (4.30) for a double dipole); $J_t(k_{ys})$ is the transverse spectrum from the transverse edge-singular current distribution ($FT\{j_t(k_{ys})\} = J_0\left(\frac{k_{ys}w_s}{2}\right)$) and AF is the array factoralong y (1 if a single dipole is used; $2\cos\left(\frac{k_y d_s}{2}\right)$ when a double dipole is used).
These steps are also done for slots; they can be found in Appendix D.

4.3 Validation

To verify the results found from the integral equations a comparison is made with the results from CST [24]. The results for both methods were close to each other, for all structures. To be complete, the results from the verification of a double dipole structure with $F_{\#} = 0.8$; $w_s = 20\ \mu m$; $\delta = 15\ \mu m$; $d_\delta = d_s = 110\ \mu m$ and $Z_l = 100\ \Omega$ using the stratification from Appendix A.2 are show in Fig. 4.15, 4.16 and 4.17 for respectively the far field, the active input impedance and the mutual coupling. For this simulation only one row of pixel is considered.

The validation for the other structures is found in Appendix E.

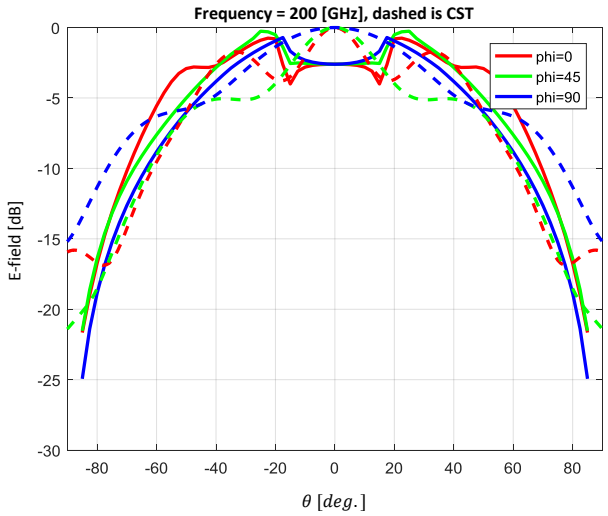

Figure 4.15: Comparison between the integral equations and CST (the dashed lines) for the far field of a double dipole with $F_{\#} = 0.8$; $w_s = 20\ \mu m$; $\delta = 15\ \mu m$; $d_\delta = d_s = 110\ \mu m$ and $Z_l = 100\ \Omega$ using the stratification from Appendix A.2.

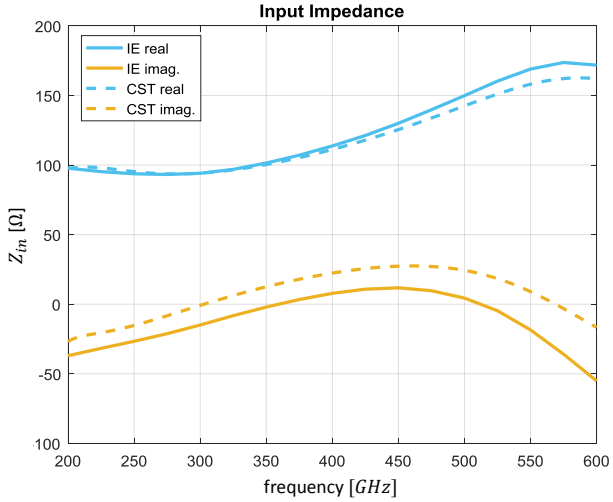

Figure 4.16: Comparison between the integral equations and CST (the dashed lines) for the active input impedance of a double dipole with $F_{\#} = 0.8$; $w_s = 20\ \mu m$; $\delta = 15\ \mu m$; $d_\delta = d_s = 110\ \mu m$ and $Z_l = 100\ \Omega$ using the stratification from Appendix A.2.

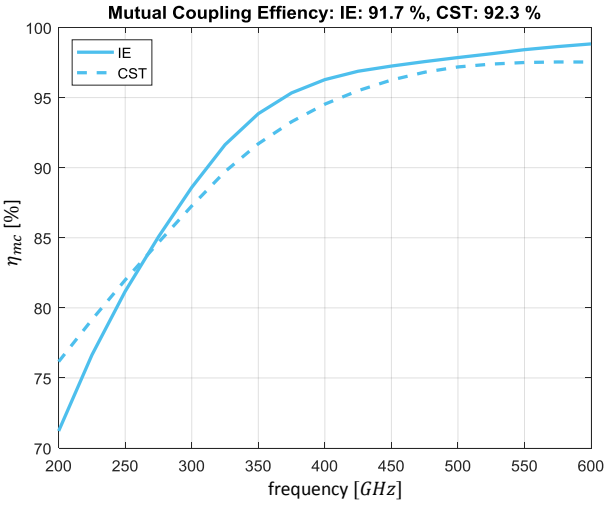

Figure 4.17: Comparison between the integral equations and CST (the dashed lines) for the mutual coupling efficiency of a double dipole with $F_{\#} = 0.8$; $w_s = 20\ \mu m$; $\delta = 15\ \mu m$; $d_\delta = d_s = 110\ \mu m$ and $Z_l = 100\ \Omega$ using the stratification from Appendix A.2. The average mutual coupling over the bandwidth is found as 91.7 % from the integral equations (IE) and 92.3 %, which are also shown in the title.

Chapter 5

Optimization

This chapter shows the results of the optimization done. First the criterias that were optimized and what is taken into account are explained in the optimization function. Then the results are shown from the analytical optimization, followed by a further optimization in a numerical optimization.

5.1 Optimization Function

The optimization is done for every structure: the single dipole, single slot, double dipole and double slot. The optimization is done in two parameters the spillover efficiency and the mutual coupling efficiency.

The spillover efficiency is influenced by the truncation angle of the used lens. The truncation angle of the lens θ_0 is calculated from the focal number of the elliptical lens $F_\#$ as $\theta_0 = \sin^{-1}\left(\frac{1}{2F_\#}\right)$. For low focal numbers the truncation angle is large, which makes the spillover efficiency high, where for low focal numbers the truncation angle is small which makes the spillover efficiency low.

The mutual coupling between the elements is influenced by the distance between the elements as $d_f = F_\#\lambda_c$. This makes that for low focal numbers the elements are spaced closer to each other, which results in a lower mutual coupling efficiency. While for higher focal numbers the elements are spaced more apart from each other which results in a higher mutual coupling efficiency.

Both efficiencies cannot be optimized at the same time, so the optimization is to find the optimal combination of the two efficiencies.

Another point that has to be taken into account is that the impedance in the delta gaps needs to be matchable over the whole frequency band. The requirement is set that using a

constant resistive load to the antenna gives a mismatch efficiency of minimal -10 dB. The impedance of the antenna is mainly influenced by the width of the dipole (or slot) and the size of the delta gaps used. The influence on the far field by tuning the impedance is minimal.

An other thing that is taken into account is the position of the side lobes. In the design the side lobes are not allowed to enter the lens aperture, which requires the side lobes to be positioned wider than the truncation angle. When the side lobes are outside the aperture the spillover efficiency will be lower, but the aperture is more directive. The side lobes are shifted in phase by 180 degrees which destructively interference the field at the lens aperture. This results in lower directive beam patterns after the lens.

When the double elements are considered, the distance between the dipoles (or slots) is set to be equal to the distance between the delta gaps ($d_s = d_\delta$ in Fig. 4.14 and D.4). By changing these parameters the array factor in the E and H-plane is changed. When the two parameters are set to be equal the array factor in both direction is approximately equal, which makes the radiation pattern more omnidirectional.

The stratification that is used for the optimization is the simplified layering from appendix A.2, inducing some enhanced leaky-wave behavior.

The first part of the optimization is done in MATLAB, where the theory from chapter 4 and appendix D is implemented. In this theory it is assumed that only one row of 7 pixels is present.

The decision of which structure is chosen and what are the optimal parameters is based on the possible efficiency that can be achieved. When the optimal parameters for each structure are found, also the implementation of the structure is taken into account.

5.2 Quasi-Analytical Optimization

Now each structure is analyzed individually, first the single elements, then the double elements.

5.2.1 Single Dipole

The single dipole is optimized as a function of the lens focal number. The average efficiencies over the bandwidth (200 GHz - 600 GHz) are shown in Fig. 5.1, with $w_s = 20$ $\mu m; \delta = 15$ μm; $N_p = 7$; $Z_l = 100$ Ω.

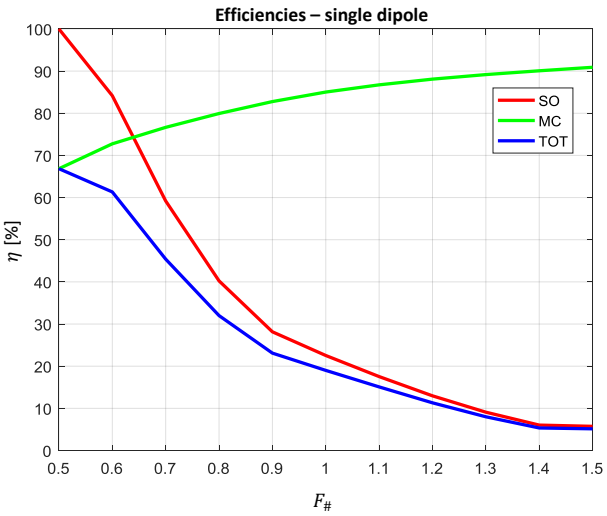

Figure 5.1: Overview of the efficiency for the single dipole ($w_s = 20\ \mu m$; $\delta = 15\ \mu m$; $N_p = 7$; $Z_l = 100\ \Omega$) over the bandwidth 200 GHz - 600 GHz. The spillover (SO), mutual coupling (MC) and total (TOT) efficiency are shown.

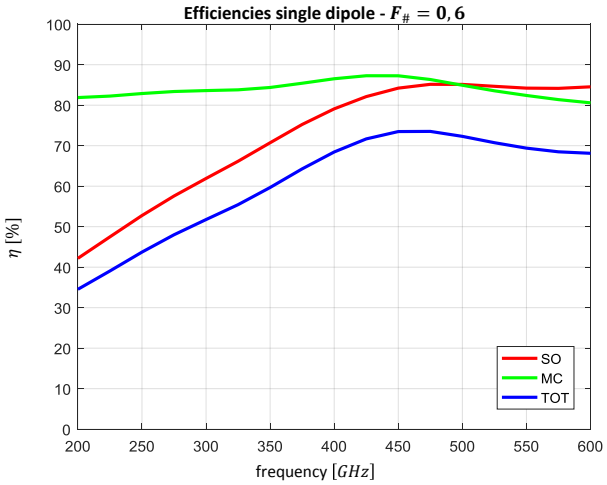

Figure 5.2: Overview of the efficiencies for the single dipole ($F_\# = 0.6$; $w_s = 20\ \mu m$; $\delta = 15\ \mu m$; $N_p = 7$; $Z_l = 100\ \Omega$) over the bandwidth 200 GHz - 600 GHz. The spillover (SO), mutual coupling (MC) and total (TOT) efficiency are shown.

In this figure it can be seen that the highest total efficiency is achieved for a focal number of 0.5. The critical angle for a silicon-air interface is approximately 56° degrees, this corresponds with a focal number of 0.6, this is set to be the optimal focal number, efficiencies for this configuration over the spectrum are shown in Fig. 5.2.

The far field for this configuration can be found in Fig. 5.3. Here the truncation angle is indicated by the black dashed line. It is clear that the main beam is completely

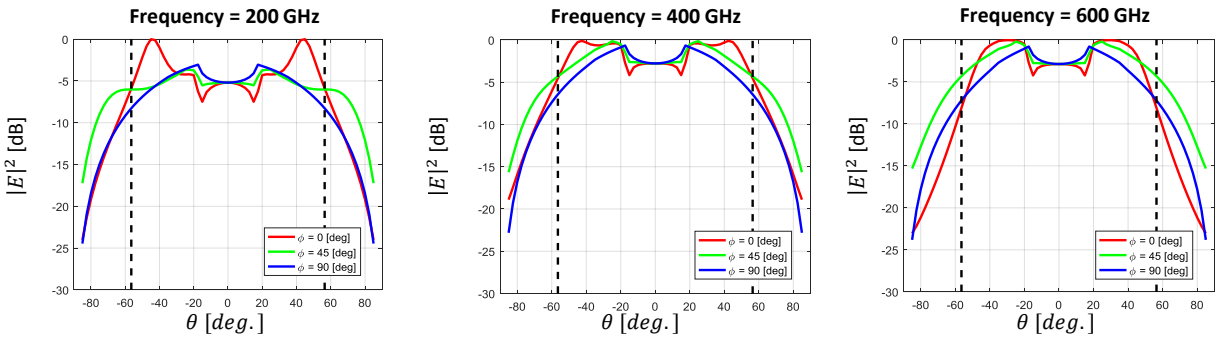

Figure 5.3: Overview of the far fields for the single dipole ($F_{\#} = 0.6$; $w_s = 20\ \mu m$; $\delta = 15\ \mu m$; $N_p = 7$; $Z_l = 100\ \Omega$) for 200 GHz, 400 GHz and 600 GHz. The truncation angle is indicated by the black dashed lines.

within the lens aperture while the crossing points at the truncation angle are below -3 dB.

For the optimal single dipole the average spillover efficiency is 84.5 %, the average mutual coupling efficiency is 73.5 % and the total average efficiency is 60.5 %.

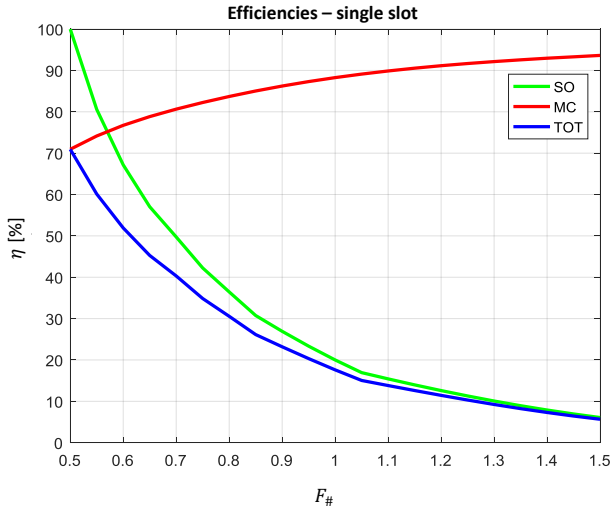

Figure 5.4: Overview of the average efficiency for the single slot ($w_s = 20\ \mu m$; $\delta = 15\ \mu m$; $N_p = 7$; $Z_l = 100\ \Omega$) over the bandwidth 200 GHz - 600 GHz. The spillover (SO), mutual coupling (MC) and total (TOT) efficiency are shown.

5.2.2 Single Slot

The single slot is also optimized as a function of the lens focal number. The average efficiencies over the bandwidth (200 GHz - 600 GHz) are shown in Fig. 5.4, with $w_s = 20$ μm; $\delta = 15\ \mu m$; $N_p = 7$; $Z_l = 100\ \Omega$.

In this figure it can be seen that the highest total efficiency is achieved for a focal number of 0.5. But the same restriction holds for the focal number as for the single dipole, so the optimal focal number becomes 0.6, efficiencies for this configuration over the spectrum are shown in Fig. 5.5.

The far field for this configuration can be found in Fig. 5.6. Here the truncation angle is indicated by the black dashed line. It is clear that the main beam is completely within the lens aperture while the crossing points at the truncation angle are below -4 dB.

For the optimal single slot the average spillover efficiency is 68.0 %, the average mutual coupling efficiency is 77.7 % and the total average efficiency is 53.3 %.

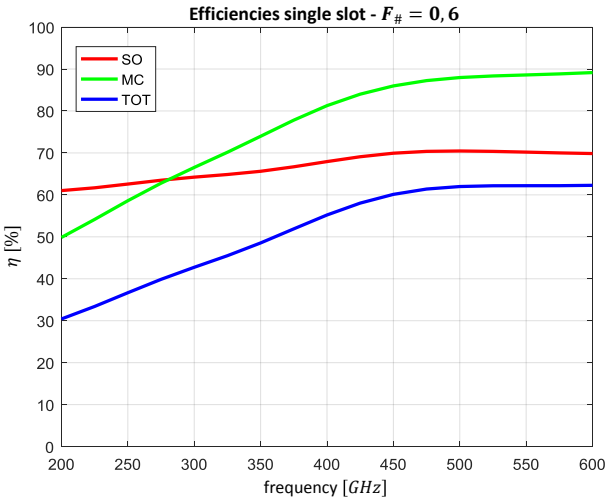

Figure 5.5: Overview of the efficiencies for the single slot ($F_{\#} = 0.6$; $w_s = 20\ \mu m$; $\delta = 15\ \mu m$; $N_p = 7$; $Z_l = 100\ \Omega$) over the bandwidth 200 GHz - 600 GHz. The spillover (SO), mutual coupling (MC) and total (TOT) efficiency are shown.

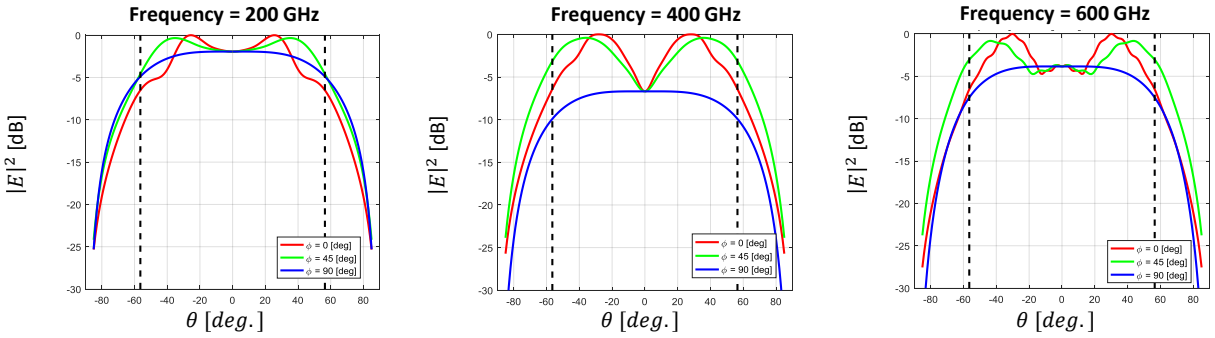

Figure 5.6: Overview of the far fields for the single slot ($F_{\#} = 0.6$; $w_s = 20\ \mu m$; $\delta = 15\ \mu m$; $N_p = 7$; $Z_l = 100\ \Omega$) for 200 GHz, 400 GHz and 600 GHz. The truncation angle is indicated by the black dashed lines.

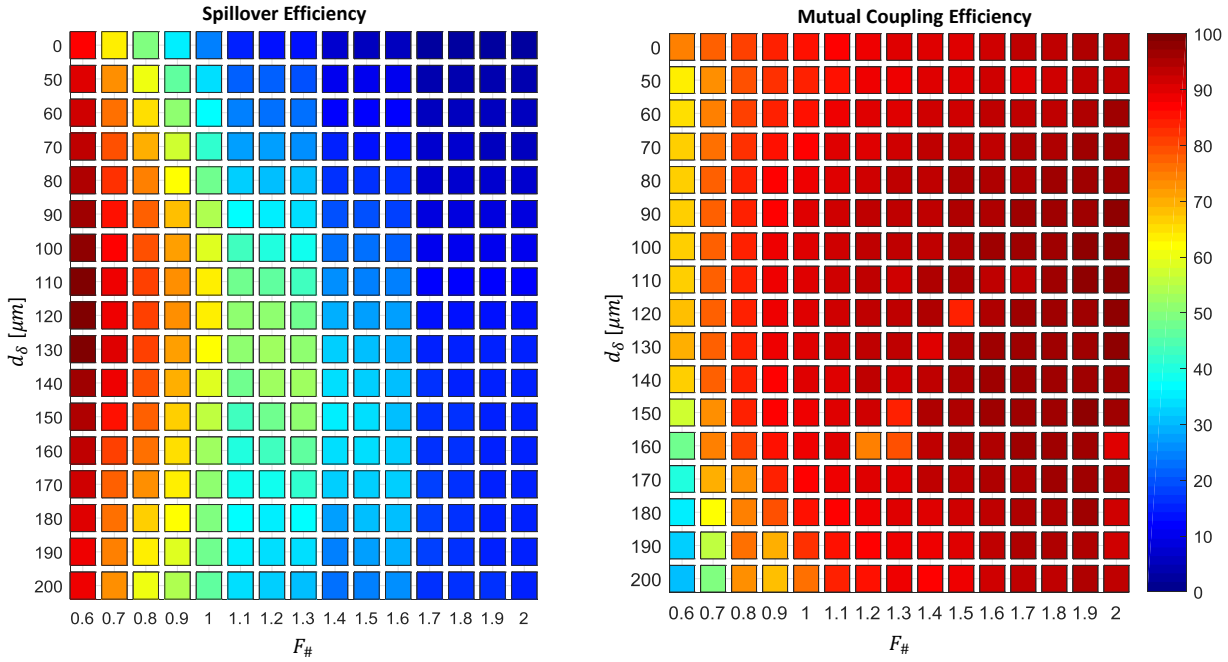

Figure 5.7: Overview of the average spillover and mutual coupling efficiency of a double dipole ($w_s = 20$ μm; $\delta = 15$ μm; $N_p = 7$; $Z_l = 100$ Ω) over the bandwidth 200 GHz - 600 GHz. It is shown as function of spacing distance d_δ and focal number $F_\#$.

5.2.3 Double Dipole

The double dipole is optimized as a function of both the spacing in the pixel and the lens focal number. The spacing distance between the dipoles is set to be equal to the distance between the delta gaps on the dipole ($d_s = d_\delta$), to make the array factor in both plane approximately equal. To visualize the optimization done, the spillover efficiency and the mutual coupling efficiency are shown in Fig. 5.7, all are averaged over the bandwidth 200 GHz to 600 GHz.

This figure shows that for highers focal numbers the average spillover efficiency gets poor, where for low focal numbers the average spillover efficiency is much better. For the spacing distance the influence is less strong.

The figure shows also that the average mutual coupling efficiency is very high (90% +) for almost all focal numbers above 0.9, below 0.7 the average mutual coupling efficiency drops drastically. The distance spacing has less impact on the result.

The spillover efficiency and the mutual coupling efficiency are combined to find the average total efficiency, this is shown in Fig. 5.8, averaged over the bandwidth 200 GHz

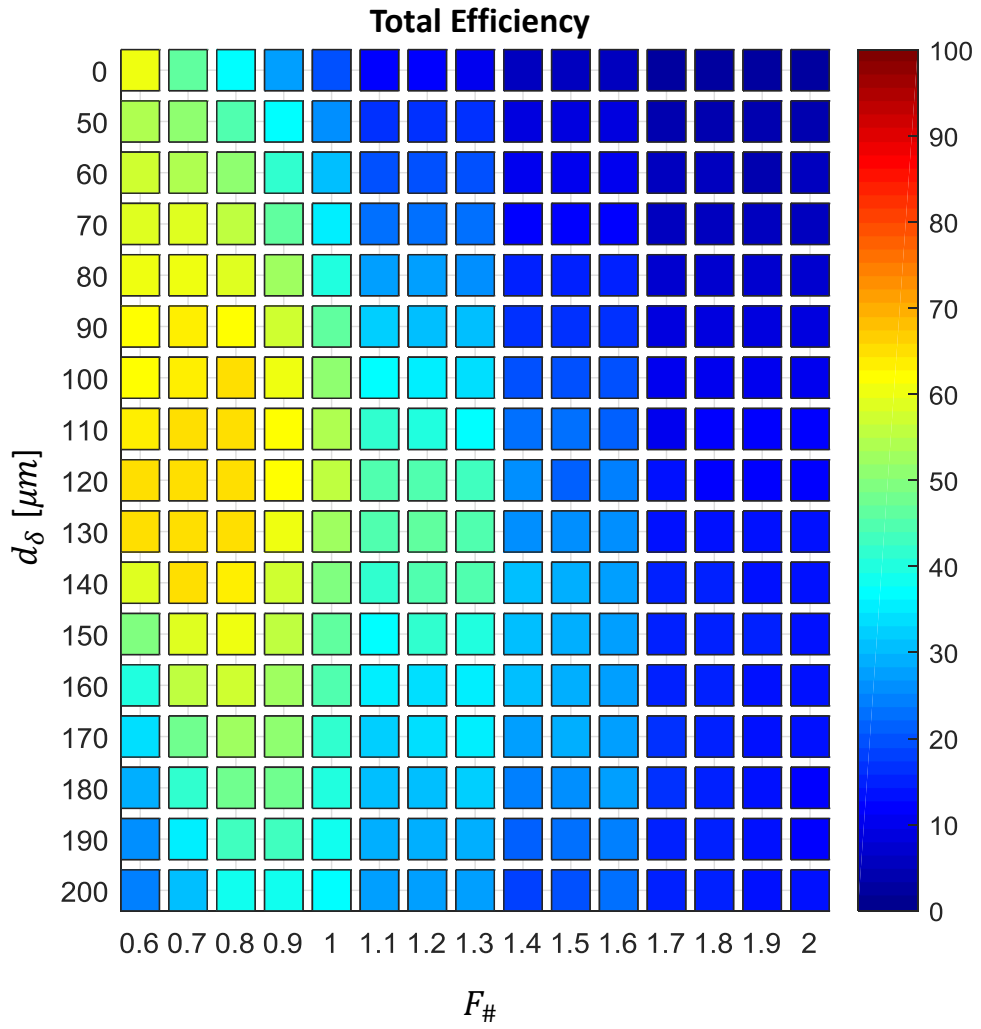

Figure 5.8: Overview of the average total efficiency of a double dipole ($w_s = 20\ \mu m$; $\delta = 15\ \mu m$; $N_p = 7$; $Z_l = 100\ \Omega$) over the bandwidth 200 GHz - 600 GHz. It is shown as function of spacing distance d_δ and focal number $F_\#$.

to 600 GHz.

The optimum in the total efficiency lies on $F_\# = 0.7$ and $d_\delta = 130\ \mu m$. The far field of this configuration are shown in Fig. 5.15. These figures show the problem of this configuration that the side lobe level is very high for higher frequencies, which are also within the lens aperture. This makes this configuration not preferable. The efficiencies of this configuration are shown in Fig. 5.10.

To solve the high side lobes, the parameters of the configuration are slightly changed

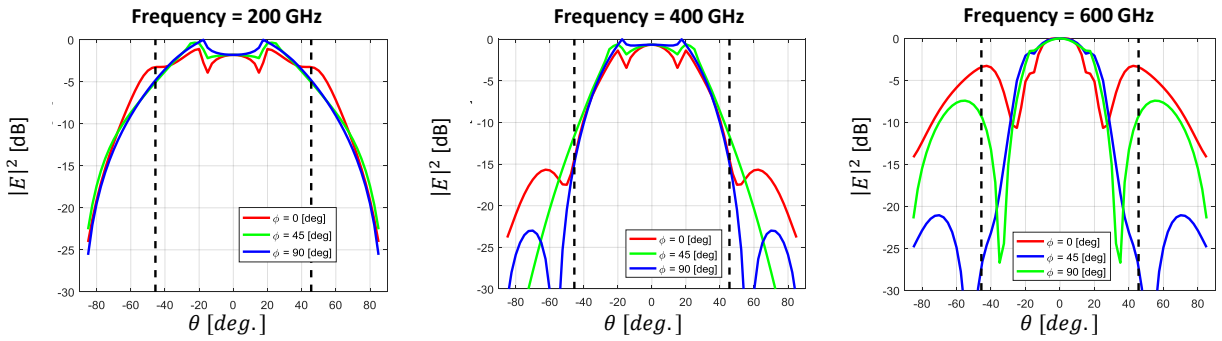

Figure 5.9: Overview of the far fields for the double dipole ($F_{\#} = 0.7$; $d_\delta = 130\ \mu m$; $w_s = 20\ \mu m$; $\delta = 15\ \mu m$; $N_p = 7$; $Z_l = 100\ \Omega$) for 200 GHz, 400 GHz and 600 GHz. The truncation angle is indicated by the black dashed lines.

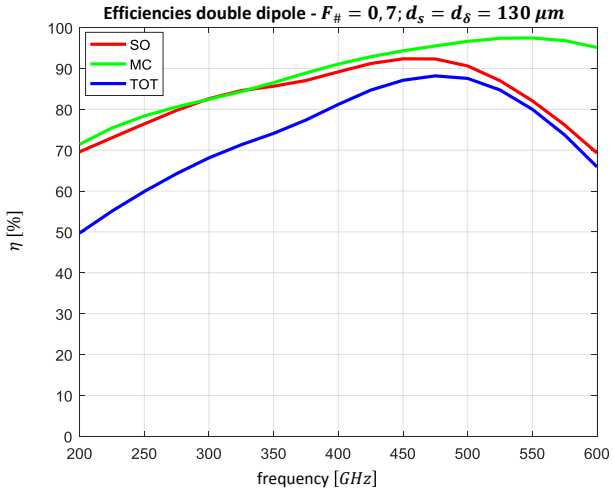

Figure 5.10: Overview of the efficiencies for the double dipole ($F_{\#} = 0.7$; $d_s = d_\delta = 130\ \mu m$; $w_s = 20\ \mu m$; $\delta = 15\ \mu m$; $N_p = 7$; $Z_l = 100\ \Omega$) over the bandwidth 200 GHz - 600 GHz. The spillover (SO), mutual coupling (MC) and total (TOT) efficiency are shown.

to $F_{\#} = 0.8$ and $d_\delta = 110\ \mu m$, Fig. 5.8 showed that the difference is a few procent w.r.t. the previous optimal. The far fields of the new optimum are found in Fig. 5.11, with much lower side lobes at higher frequencies and the side lobes also do not enter the lens aperture. The efficiencies for this configuration are shown in Fig. 5.12. This configuration is assumed to be the optimal for this structure.

For the optimal double dipole the average spillover efficiency is 71.3 %, the average mutual coupling efficiency is 92.5 % and the total average efficiency is 66.8 %.

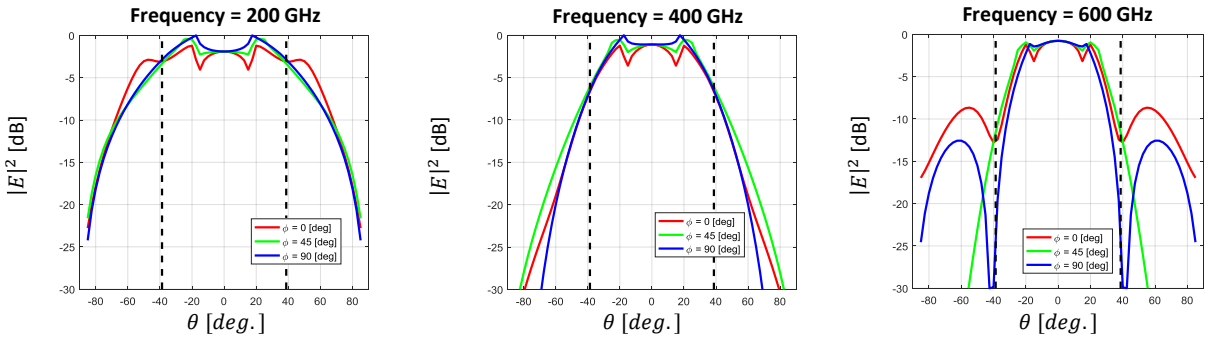

Figure 5.11: Overview of the far fields for the double dipole ($F_{\#} = 0.8$; $d_\delta = 110\ \mu m$; $w_s = 20\ \mu m$; $\delta = 15\ \mu m$; $N_p = 7$; $Z_l = 100\ \Omega$) for 200 GHz, 400 GHz and 600 GHz. The truncation angle is indicated by the black dashed lines.

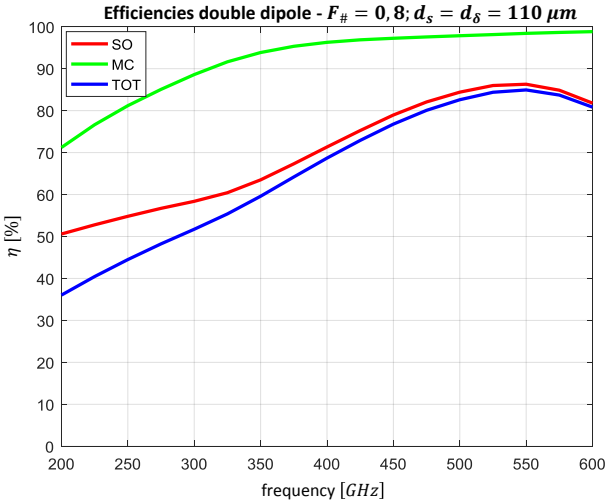

Figure 5.12: Overview of the efficiencies for the double dipole ($F_{\#} = 0.8$; $d_s = d_\delta = 110\ \mu m$; $w_s = 20\ \mu m$; $\delta = 15\ \mu m$; $N_p = 7$; $Z_l = 100\ \Omega$) over the bandwidth 200 GHz - 600 GHz. The spillover (SO), mutual coupling (MC) and total (TOT) efficiency are shown.

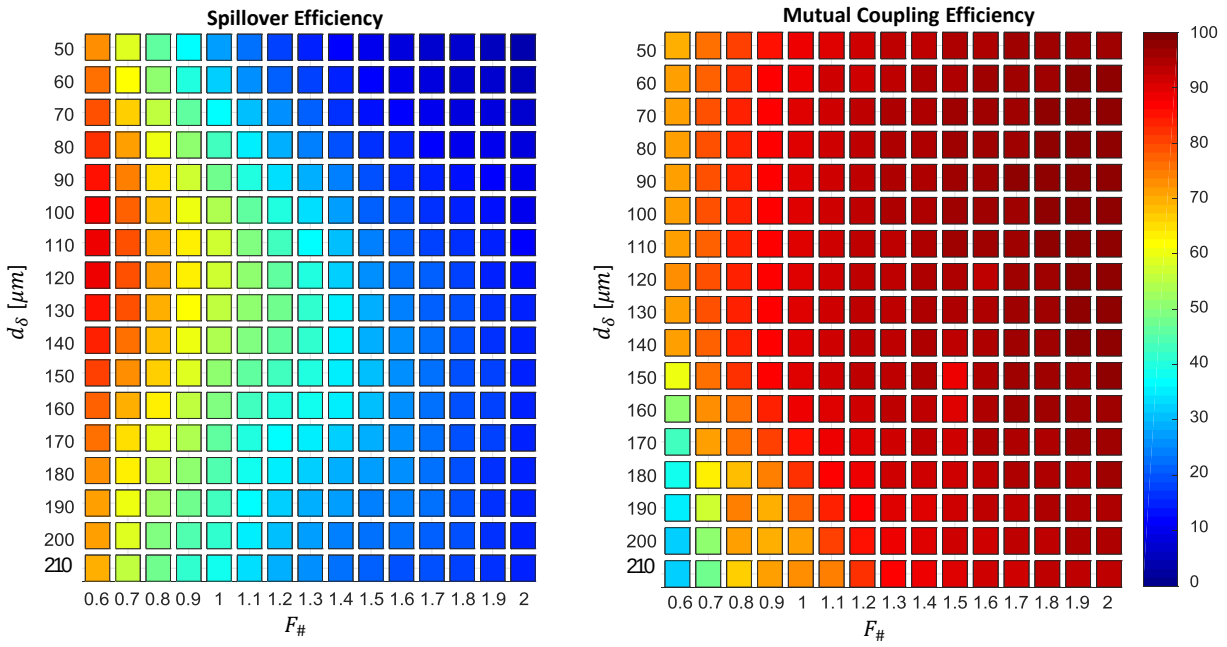

Figure 5.13: Overview of the average spillover and mutual coupling efficiency of a double slot ($w_s = 20$ μm; $\delta = 15$ μm; $N_p = 7$; $Z_l = 100$ Ω) over the bandwidth 200 GHz - 600 GHz. It is shown as function of spacing distance d_δ and focal number $F_\#$.

5.2.4 Double Slot

The double slot is optimized as a function of both the spacing in the pixel and the lens focal number. The spacing distance between the slots is set to be equal to the distance between the delta gaps on the slot ($d_s = d_\delta$), to make the array factor in both plane approximately equal. To visualize the optimization done, the spillover efficiency and the mutual coupling efficiency are shown in Fig. 5.13, all are averaged over the bandwidth 200 GHz to 600 GHz.

This figure shows that for highers focal numbers the average spillover efficiency gets poor, where for low focal numbers the average spillover efficiency is much better. For the spacing distance the influence is less strong.

The figure shows also that the average mutual coupling efficiency is very high (90 % +) for almost all focal numbers above 0.9, below 0.7. The distance spacing has less impact on the result.

The spillover efficiency and the mutual coupling efficiency are combined to find the average total efficiency, this is shown in Fig. 5.14, averaged over the bandwidth 200 GHz to 600 GHz.

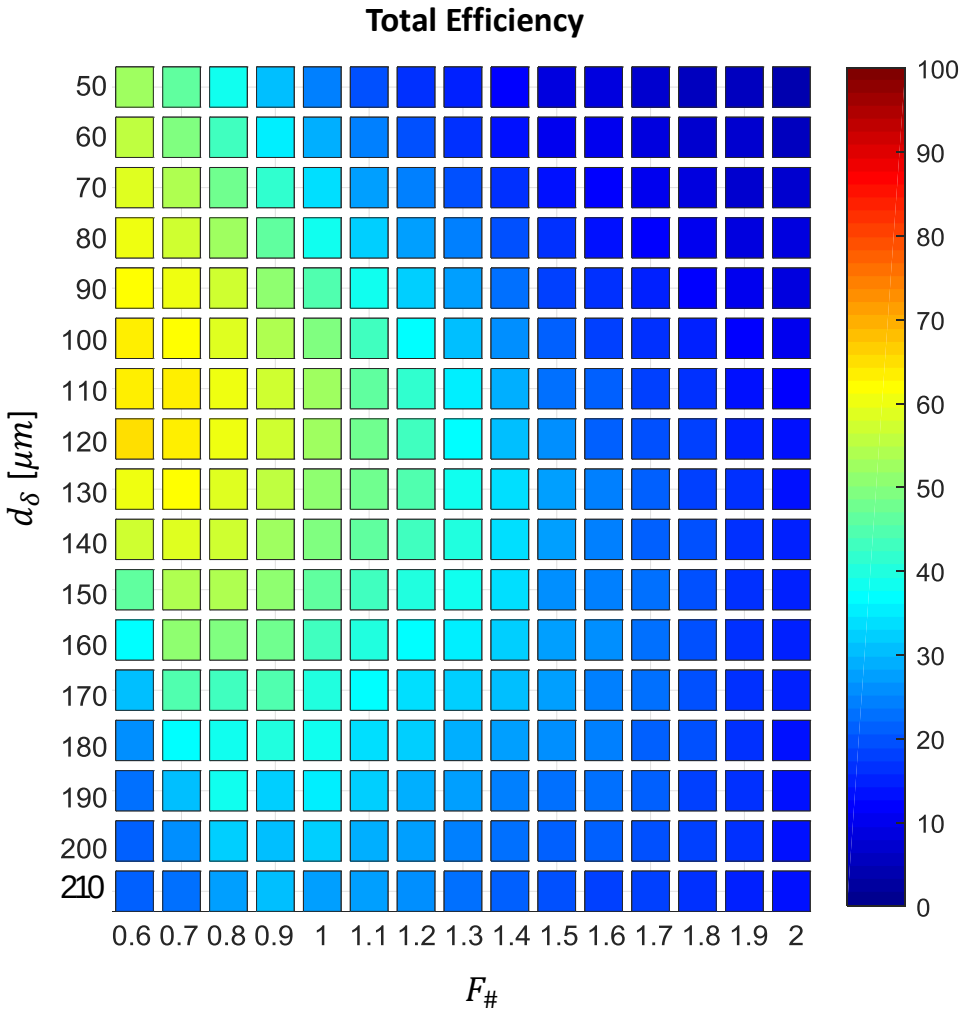

Figure 5.14: Overview of the average total efficiency of a double slot ($w_s = 20\ \mu m$; $\delta = 15\ \mu m$; $N_p = 7$; $Z_l = 100\ \Omega$) over the bandwidth 200 GHz - 600 GHz. It is shown as function of spacing distance d_δ and focal number $F_\#$.

The optimum in the total efficiency lies on $F_\# = 0.6$ and $d_\delta = 120\ \mu m$. The far field of this configuration are shown in Fig. 5.15 and the efficiencies over the bandwidth are shown in Fig. 5.16. These figures show the problem of this configuration that the side lobe level is very high for higher frequencies, which are also within the lens aperture. This makes the configuration not preferable.

To solve the high side lobes, the parameters of the configuration are slightly changed to $F_\# = 0.8$ and $d_\delta = 110\ \mu m$, Fig. 5.14 showed that the difference is a few procent w.r.t. the previous optimal. The far fields of the new optimum are found in Fig. 5.17 with much lower side lobes at higher frequencies and the side lobes also do not enter the lens aperture.

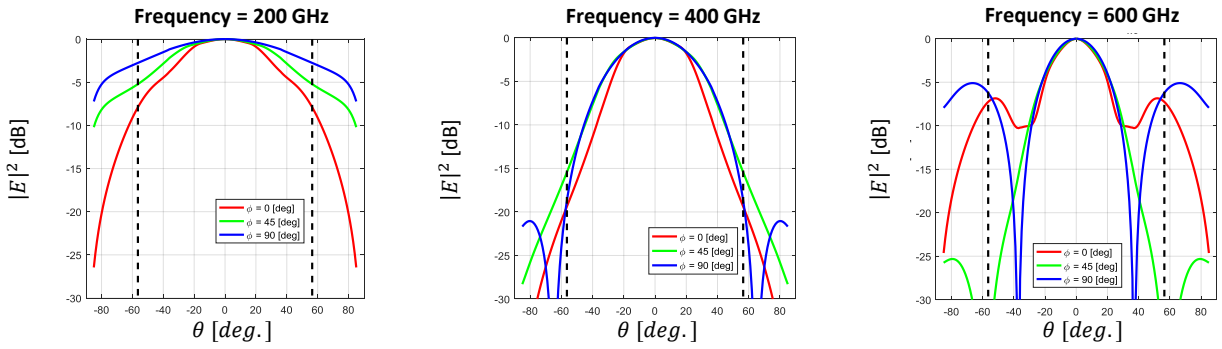

Figure 5.15: Overview of the far fields for the double slot ($F_{\#} = 0.6$; $d_\delta = 120\ \mu m$; $w_s = 20\ \mu m$; $\delta = 15\ \mu m$; $N_p = 7$; $Z_l = 100\ \Omega$) for 200 GHz, 400 GHz and 600 GHz. The truncation angle is indicated by the black dashed lines.

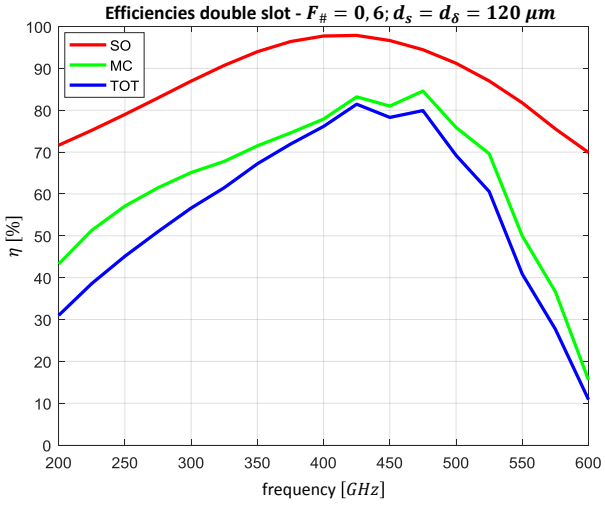

Figure 5.16: Overview of the efficiencies for the double slot ($F_{\#} = 0.6$; $d_s = d_\delta = 120\ \mu m$; $w_s = 20\ \mu m$; $\delta = 15\ \mu m$; $N_p = 7$; $Z_l = 100\ \Omega$) over the bandwidth 200 GHz - 600 GHz. The spillover (SO), mutual coupling (MC) and total (TOT) efficiency are shown.

The efficiencies over the operational bandwidth are shown in Fig. 5.18. This configuration is assumed to be the optimal for this structure.

For the optimal double slot the average spillover efficiency is 83.7 %, the average mutual coupling efficiency is 71.1 % and the total average efficiency is 61.1 %. From best to worst performance the structures are ordered as double dipole, double slot, single dipole and single slot.

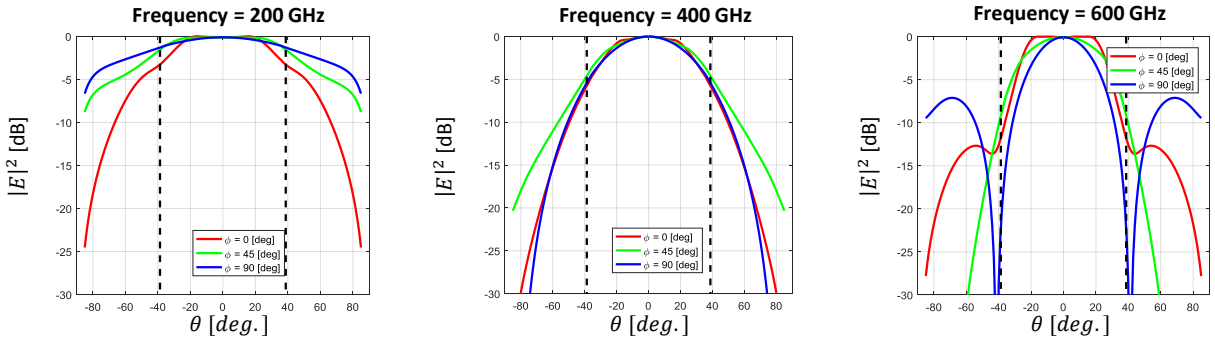

Figure 5.17: Overview of the far fields for the double slot ($F_{\#} = 0.8$; $d_\delta = 110\ \mu m$; $w_s = 20\ \mu m$; $\delta = 15\ \mu m$; $N_p = 7$; $Z_l = 100\ \Omega$) for 200 GHz, 400 GHz and 600 GHz. The truncation angle is indicated by the black dashed lines.

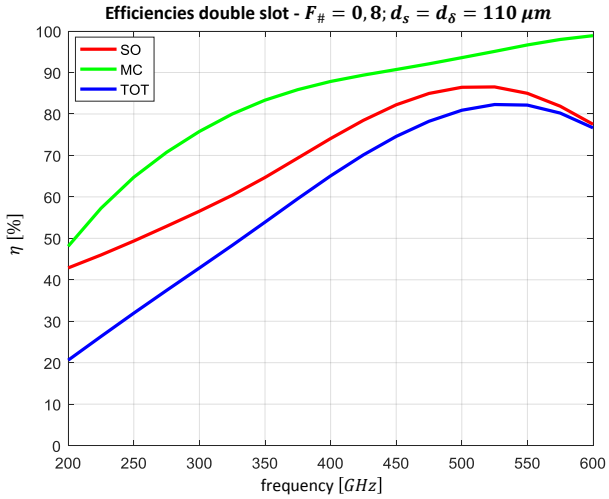

Figure 5.18: Overview of the efficiencies for the double slot ($F_{\#} = 0.8$; $d_s = d_\delta = 110\ \mu m$; $w_s = 20\ \mu m$; $\delta = 15\ \mu m$; $N_p = 7$; $Z_l = 100\ \Omega$) over the bandwidth 200 GHz - 600 GHz. The spillover (SO), mutual coupling (MC) and total (TOT) efficiency are shown.

5.2.5 Overview of Optimums

To give an overview of the optimum configuration per structure, the parameters are given in table 5.1 and the estimated performance is given in table 5.2

Table 5.1: Parameters that are used for every type of element to calculated the performance, with $w_s = 20$ μm; $\delta = 15$ μm.

Element type	$F_\#$	δ $[\mu m]$	w_s $[\mu m]$	d_s, d_δ $[\mu m]$
Single dipole	0.6	5	20	n.a.
Single slot	0.6	5	20	n.a.
Double dipole	0.8	5	20	110
Double slot	0.8	5	20	110

Table 5.2: Average efficiencies over the bandwidth from 200 GHz to 600 GHz for the optima from table 5.1.

Element type	$\bar{\eta}_{so}$	$\bar{\eta}_{mc}$	$\bar{\eta}_{tot}$
Single dipole	84.5 %	73.5 %	60.5 %
Single slot	68.0 %	77.7 %	53.3 %
Double dipole	71.3 %	92.5 %	66.8 %
Double slot	83.6 %	70.5 %	61.1 %

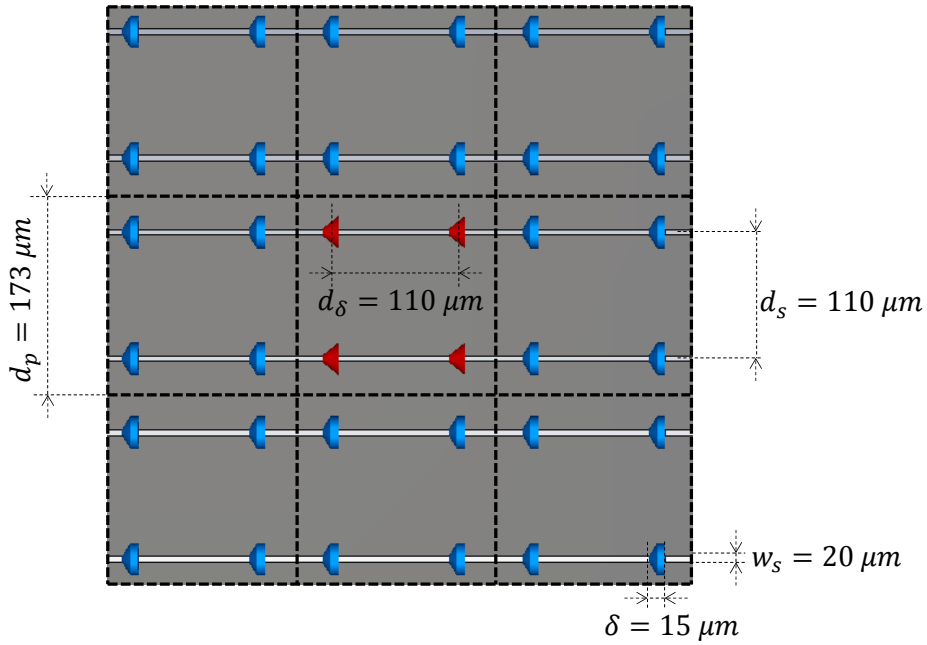

Figure 5.19: CST implementation of the optimal double dipole structure, where a 3 by 3 pixel array is shown with its geometric parameters. Light gray is the metal of the dipoles and dark gray is the SiO_2 substrate. The red ports indicate the central pixel, which are fed simultaneously, the blue ports are resistive elements to simulate the mutual coupling in the array.

5.3 Numerical Optimization

The design of the structures is continued in CST Microwave Studio. CST is used to calculated the rest of the considered efficiencies and also to see how the implementation of the structure influences the performance. First the double dipole is analyzed, since it was most efficient in the optimization.

Double Dipole

A screenshot from CST of the double dipole structure from the optimization is found in Fig. 5.19. This figure shows a part of the array of pixels (3 by 3 pixels are shown), here is seen that the delta gaps in the central pixel are closely placed to the delta gaps of the adjacent pixels.

In the analysis of this structure the implementation of the feeding network for the pixels is investigated. Since each pixel contains 4 delta gaps they need to be connected

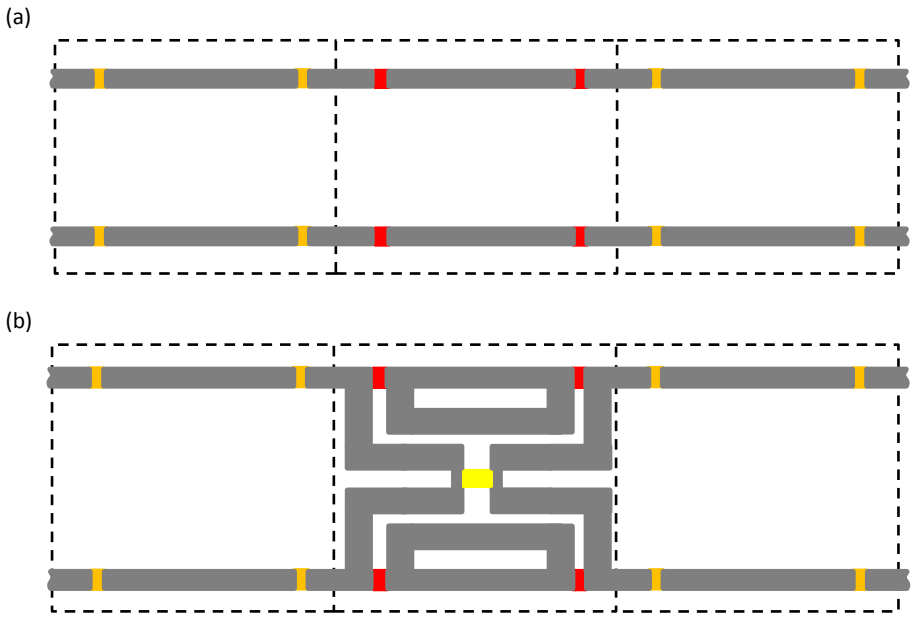

Figure 5.20: Schematic overview of the feeding network for a double dipole structure. In (a) it is modeled as 4 delta-gaps that are excited in phase with equal amplitude; in (b) a transmission line is added to excite the 4 gaps in the structure.

through a feeding network. A visualization of the feeding network is found in Fig. 5.20. It shows that a transmission line is used to excite the 4 gaps. The use of this transmission line lowers the efficiency with respect to the ideal delta gaps, since some power is dissipated in the transmission line.

Another limiting factor in this circuit is the radiation from the tranmission line. In Fig. 5.21 (a) the solution from the integral equations (solid lines) match the CST simulation (dashed lines) well. In this simulation no feeding network is used and all 4 ports of the central pixel are excited in phase and with equal amplitude. Fig. 5.21 (b) shows the far field while the feeding network is implemented. The CST simulation no longer matches the integral equation, since large side lobes are present which are almost 10 dB higher than expected in the integral equations.

The cause of the strong side lobes comes from the common mode radiation in the transmission line. Fig. 5.22 shows the field intensity present in the structure of an excited pixel. In this transmission line the current flows in the same direction in both lines, this makes common mode radiation occur, which change the radiation pattern of the structure.

These strong side lobe make the double dipole not suitable as a solution.

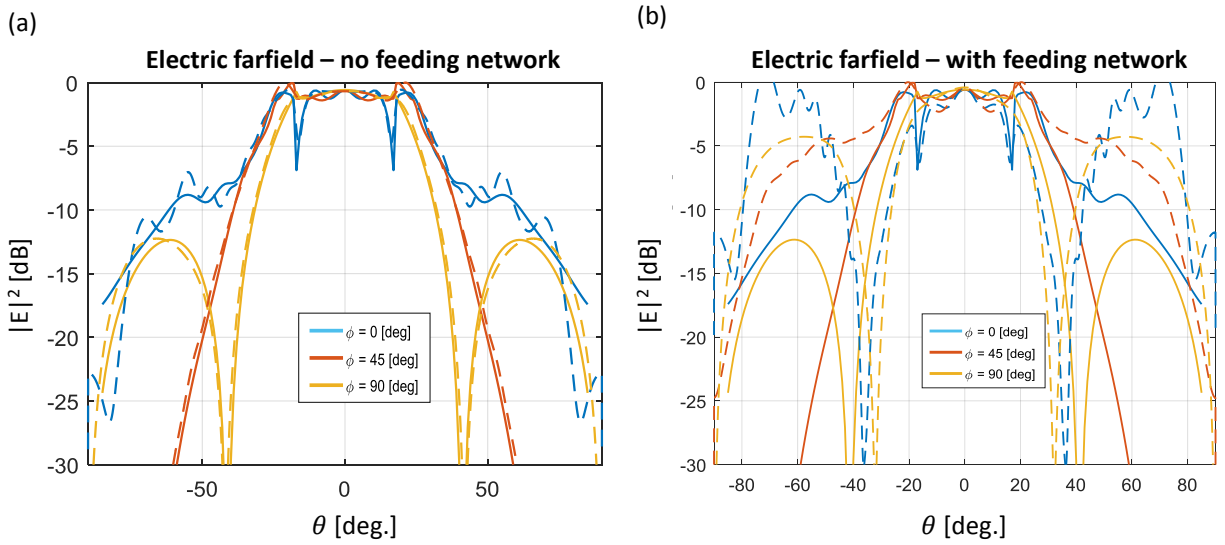

Figure 5.21: Far field of the double dipole structure, the solid lines are from the integral equations and the dashed lines are from the CST simulation. (a) is the far field without the feeding network; (b) is the far field with the implemented feeding network.

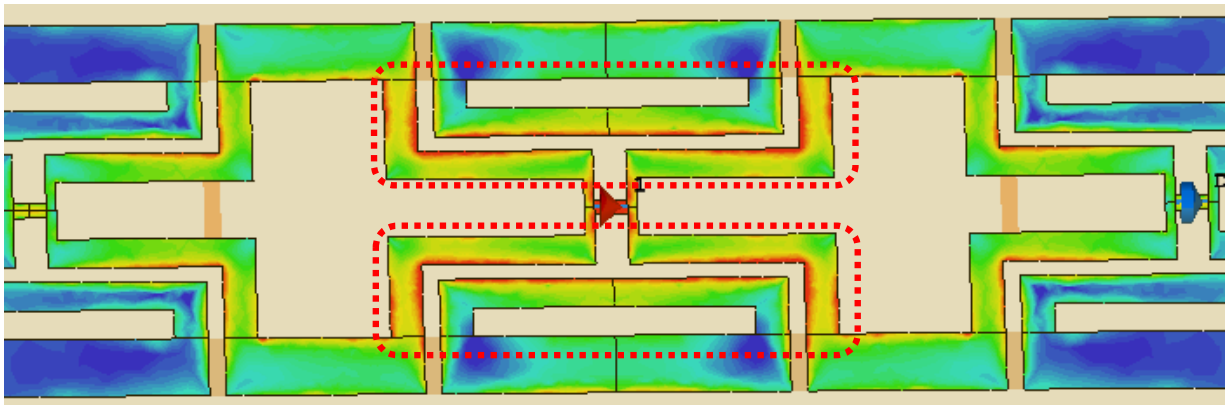

Figure 5.22: An intensity pattern on the structure of the double dipole with a feeding network. In the transmission line the red boxed parts indicate a strong common mode present there.

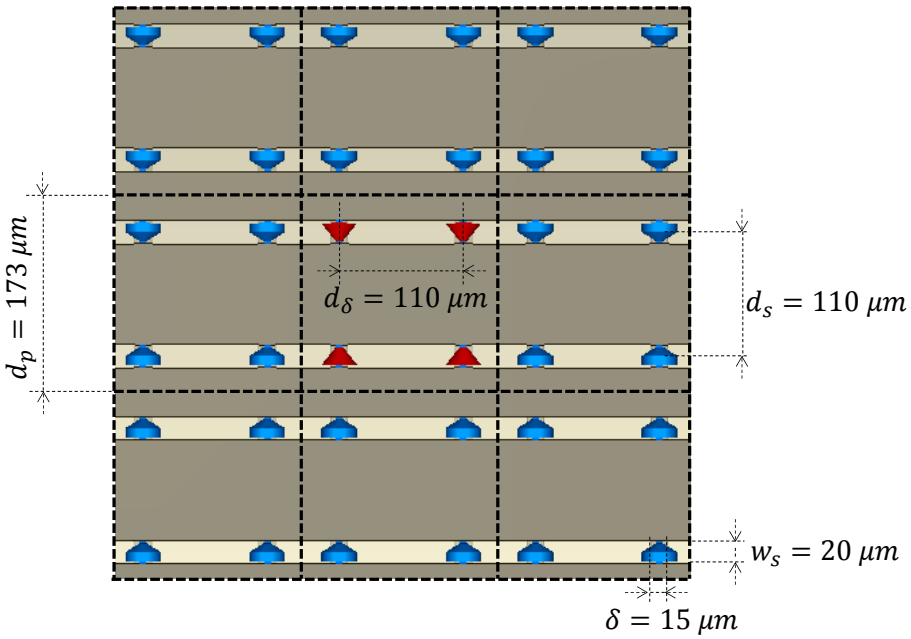

Figure 5.23: CST implementation of the optimal double slot structure, where a 3 by 3 pixel array is shown with its geometric parameters and dark gray indicates the metal of the slots and light gray is the SiO_2 substrate. The red ports indicate the central pixel, which are fed simultaneously, the blue ports are resistive elements to simulate the mutual coupling in the array.

Double Slot

The second best structure is the double slot. This is similarly implemented as the double dipole, a screenshot from CST of the double slot structure is shown in Fig. 5.23. This figure shows a part of the array of pixels (3 by 3 pixels are shown), here is seen that the delta gaps in the central pixel are closely placed to the delta gaps of the adjacent pixels.

In the optimization the structure is assumed to have only one row of pixels, so the mutual coupling of the simulation is expected to be higher since more other elements are present. The mutual coupling efficiency for the integral equations and the CST simulation are shown in Fig. 5.24. This shows that the difference in mutual coupling efficiency is more than 10% over the whole frequency band. This additional loss in efficiency cancels out the potential gain that could be achieved by using the double slot.

A feeding network for the double slot will introduce additional ohmic losses. This makes the double slot not suitable as a solution.

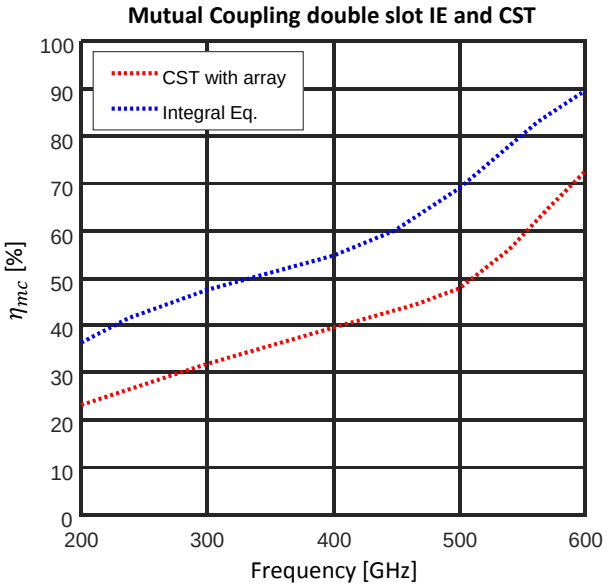

Figure 5.24: Mutual coupling efficiency for a double slot structure, without feeding network, from the integral equations and the CST simulation(3 rows of pixels).

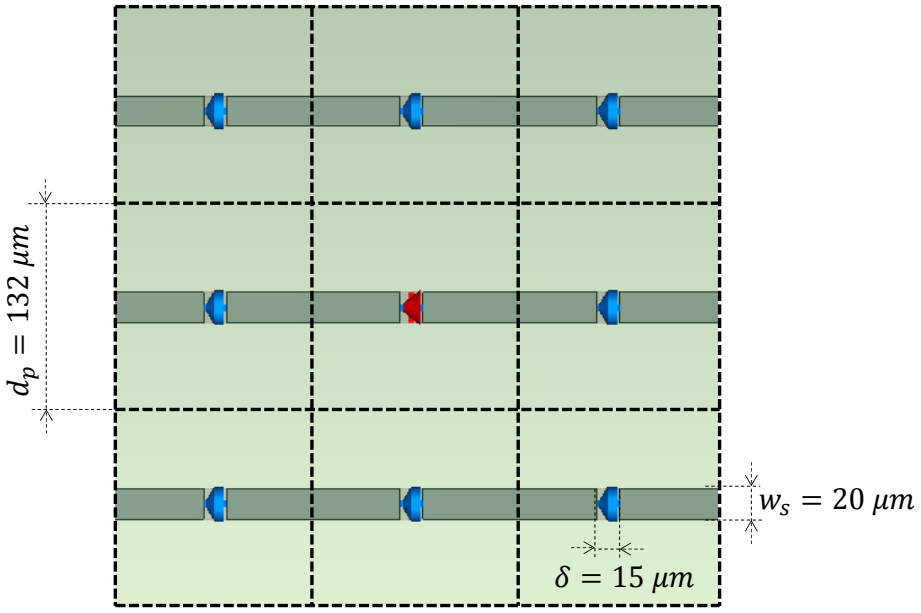

Figure 5.25: CST implementation of the optimal single dipole structure, where a 3 by 3 pixel array is shown with its geometric parameters. dark gray is the metal of the dipoles and light gray is the SiO_2 substrate.

Single Dipole

The third best option is the single dipole structure, a CST screenshot is found in Fig. 5.25. This figure shows a pixel array of 3 by 3 pixel with its geometric parameters. The dark gray indicated the metal of the dipoles and the light gray is the SiO_2 substrate. The central pixel is only one red port, the rest of the pixel are blue resistive ports.

The first benefit from using a single element structure is that the detectors can be connected to the delta gaps directly, without using a feeding network. Although the potential efficiency is expected to be lower than in the double element variant, the preference is for using the single element. Also the side lobes are not influenced by this implementation. CST is used to calculate the feed efficiency η_{feed} which is expressed as:

$$\eta_{feed}(f) = \eta_{so}(f)\eta_{mc}(f)\eta_{ohm}(f)\eta_{imp}(f) \tag{5.1}$$

with η_{so} the spillover efficiency, η_{mc} the mutual coupling efficiency, η_{ohm} the ohmic efficiency and η_{imp} the matching efficiency. The results can be found in Fig. 5.26, this show that the average feed efficiency over the bandwidth is 37.1 %. The coresponding input impedance is found in Fig. 5.27

It is assumed that the performance of the single dipole is comparable with the single slot, so the decision is made to use the single dipole.

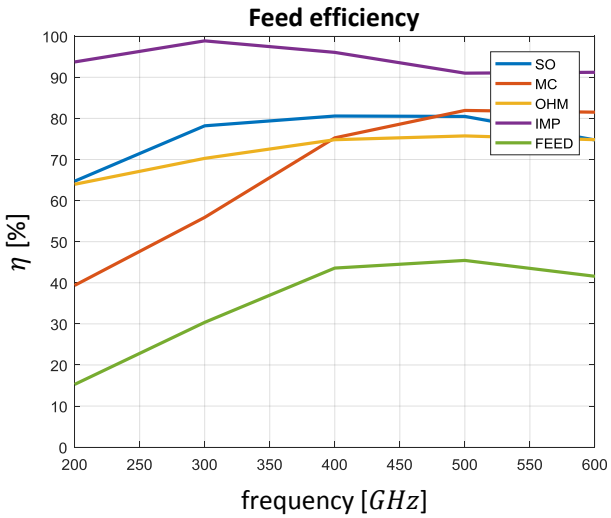

Figure 5.26: CST efficiency results from the implementation of a single dipole array, it shows the spillover efficiency (SO), the mutual coupling efficiency (MC), the ohmic effiency (OHM) and the matching efficiency (IMP). The average feed efficiency (FEED) over the bandwidth is 37.1%.

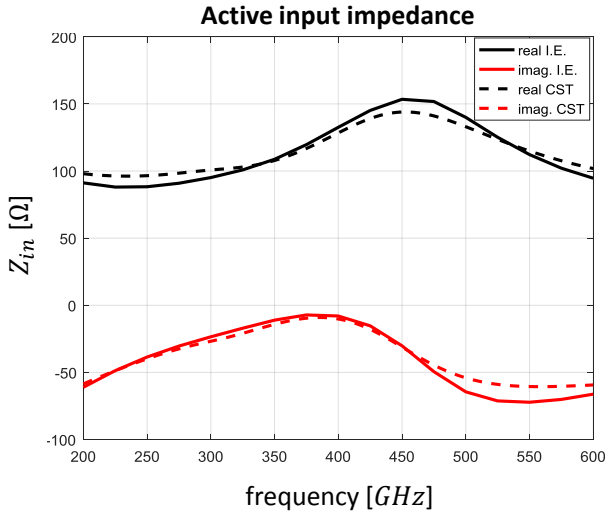

Figure 5.27: Active input impedance of the dipole structure found in the optimization, showing both the results from the integral equations (IE) and the results found in CST.

Tapered Single Dipole

To improve the design found further the influnce of tapering the dipoles is considered, this follows the geometry from Fig. 5.28.

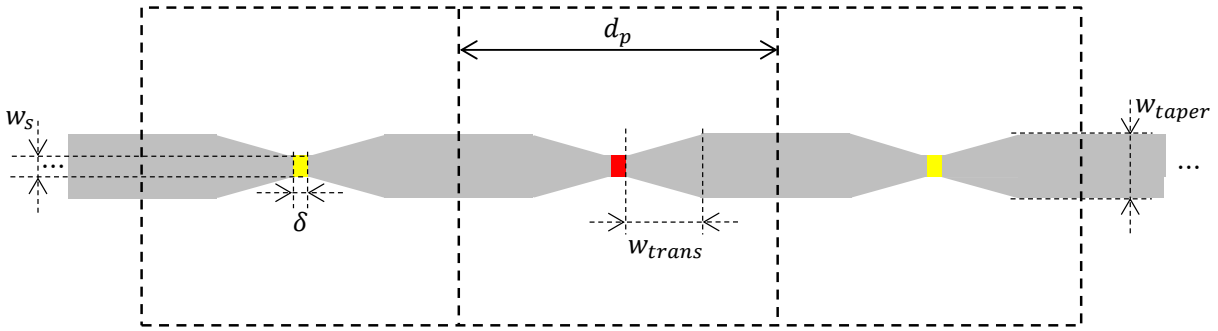

Figure 5.28: Geometry used for the tapering of the single dipole structure. with unit cell length d_p, delta gap width δ, dipole width w_s, tapering width w_{taper} and taper transition length w_{trans}.

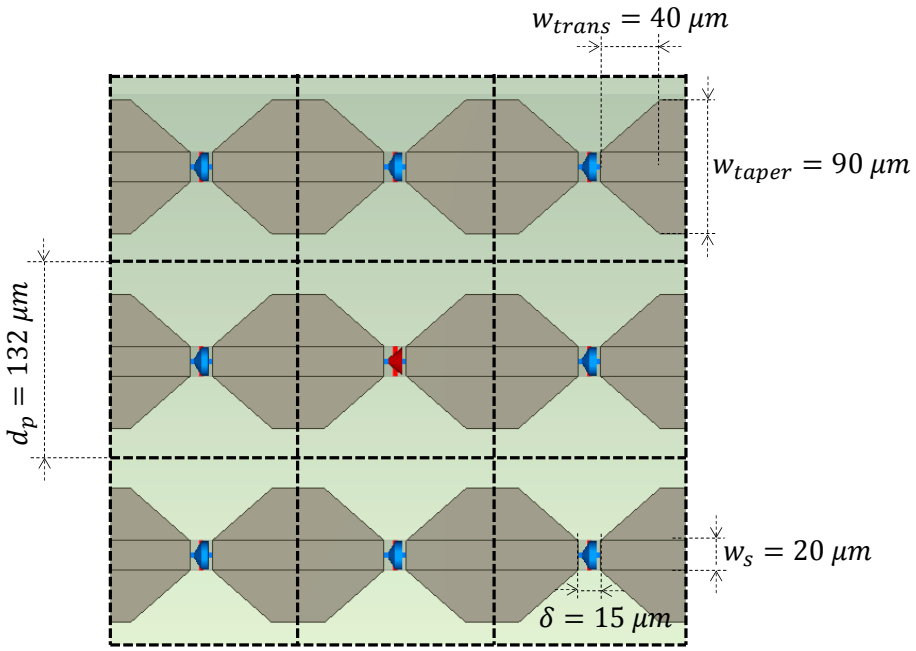

Figure 5.29: CST implementation of the optimal tapered single dipole structure, where a 3 by 3 pixel array is shown with its geometric parameters. dark gray is the metal of the dipoles and light gray is the SiO_2 substrate.

By tapering the dipole in the structure, the decay of the current along the dipole gets stronger, which improves the mutual coupling efficiency. However, a smaller current distribution also results in a less directive far field.
After optimizing the taper all found parameters are found in table 5.3, where the total efficiency is used to find the optimal solution. A screenshot of the array in CST is shown in Fig. 5.29.

An overview of all the efficiency terms is found in Fig. 5.30. This is the efficiency

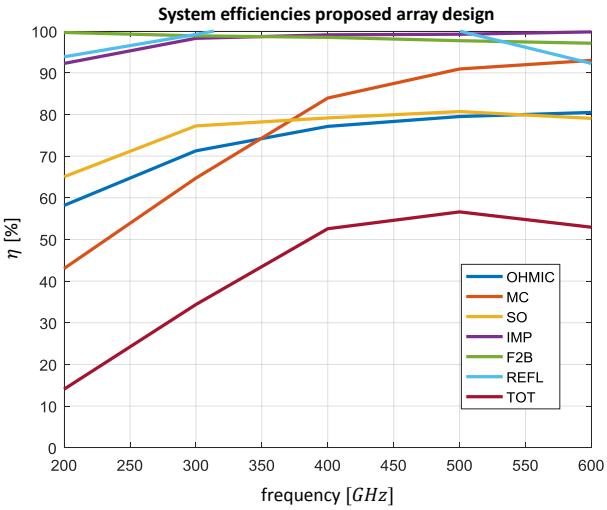

Figure 5.30: Efficiency terms present in the tapered array of dipole from table 5.3. The average system efficiency over the bandwidth is 44.3 %. It consists of the Ohmic efficiency (OHM), the mutual coupling efficiency (MC), the spillover efficiency (SO), the mismatching efficiency (IMP), the front-to-back efficiency (F2B), the reflection efficiency (REFL) and the system efficiency (TOT).

that is assumed in the rest of the performance analysis, the average system efficiency over the bandwidth is 44.3 %.

The parameters for the final design is found in table 5.3

Parameter	Value
Focal number $F_{\#}$	0.60
Unit cell length d_p	132 μm
dipole width w_s	20 μm
delta gap width δ	15 μm
Tapering width w_{taper}	90 μm
Transition length w_{trans}	40 μm
Average system eff $\bar{\eta}_{sys}$	44.3 %

Table 5.3: This table contains the parameters proposed for the tapered single dipole structure.

This array is simulated in CST to find the primary fields in Fig. 5.31. Then the automated physical optics (PO) is used to calculate the secondary field. In Chapter 3 it was explained that a 5 cm lens ($60\lambda_c$) will be used in this scenario. The radiated far field after such dielectric lens can be analyzed using in-house developed PO tools. In order to relax computational costs we will analyze a 8 mm lens.

The results of the secondary fields are show in Fig. 5.32. The active input impedance for

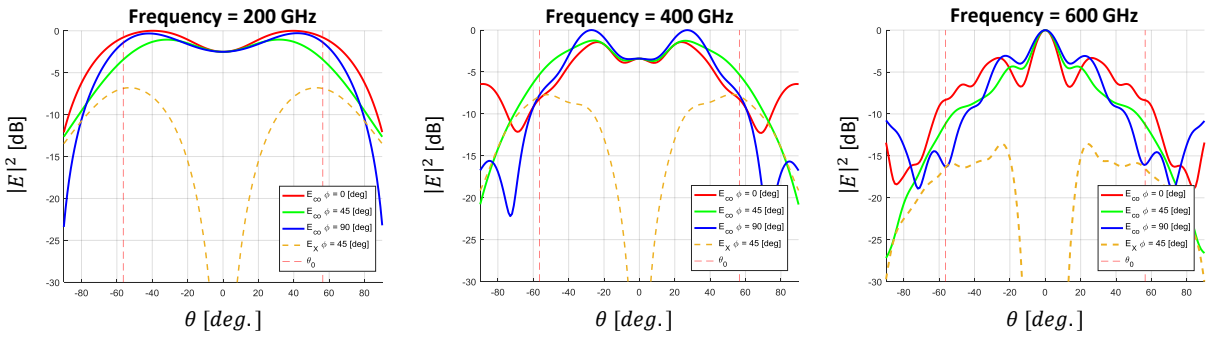

Figure 5.31: Primary fields for the tapered dipole structure for frequencies of 200 GHz, 400 GHz and 600 GHz.

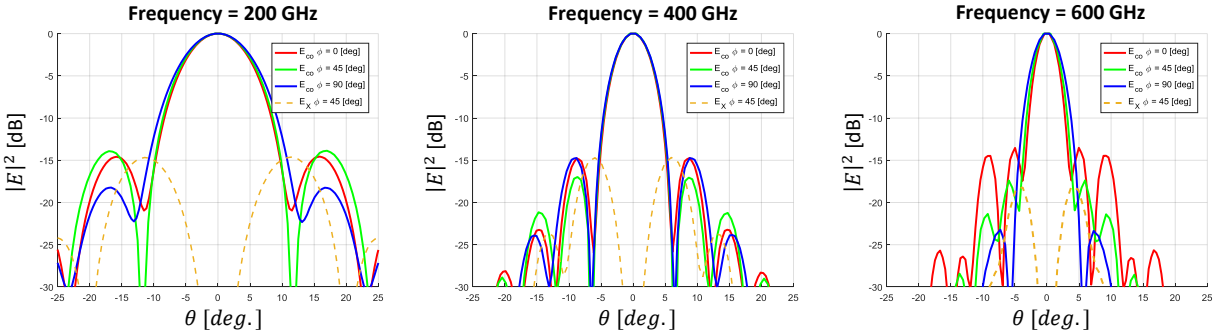

Figure 5.32: Secondary fields for the tapered dipole structure for frequencies of 200 GHz, 400 GHz and 600 GHz, calculated using a lens with a diameter of 8 mm.

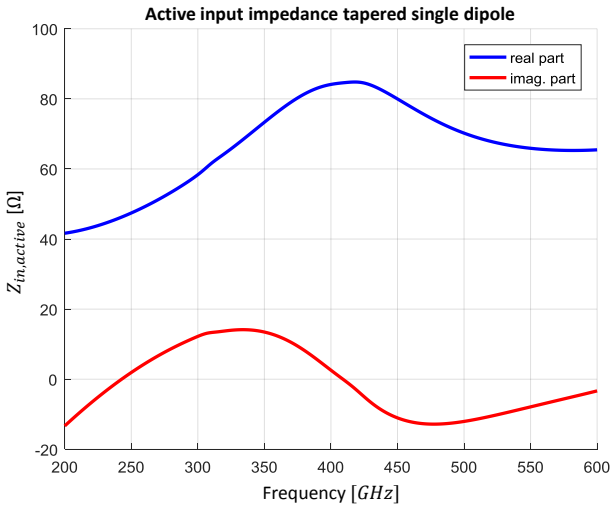

Figure 5.33: The active input impedance from the tapered dipole, simulated in CST.

the tapered dipole is found in Fig. 5.33.

Chapter 6

Array Performance in Pedestrian Detection

This chapter summarizes the performance of the final array design. Giving the performance in terms of radiation patterns and in sensitivity of the imager.

6.1 Sampling

In the previous chapter the final design for the array of connected dipoles is done. Using the system efficiencies and the radiation pattern from the simulations of the final design, the effective gain pattern can be calculated (Eq. (2.15)), it is shown in Fig. 6.1. This shows how the FoV looks for the 7 by 7 elements prototype, it also shows the cut for ϕ is 0 degrees of the center pixel and the two adjacent pixels. The crossing point of the effective gain patterns is at an angle of $\frac{\lambda_c}{2D}$ at a level of -2.5dB.

The effective gain pattern is the integrated directivity patterns weighted by the system efficiency over frequency, the radiation patterns for 200 GHz, 400 GHz and 600 GHz are shown in Fig. 6.2, 6.3 and 6.4 respectively. When the system efficiency would be uniform the effective gain pattern would be identical to the radiation pattern of the center frequency [17].The efficiency of the final design is shown in Fig. 5.30, which is not uniform but is higher for higher frequencies, due to this the effective gain pattern is more influenced by the higher frequency patterns, which results in a lower crossing point.

The effective bandwidth is calculated from Eq. (2.14) and with an operational bandwidth of 400 GHz and the average system efficiency of 44.3 %, the effective bandwidth is 177.2 GHz. To place this in the focus area indication from Fig. 1.3, this imager is placed close left under the circle indicating the focus area.

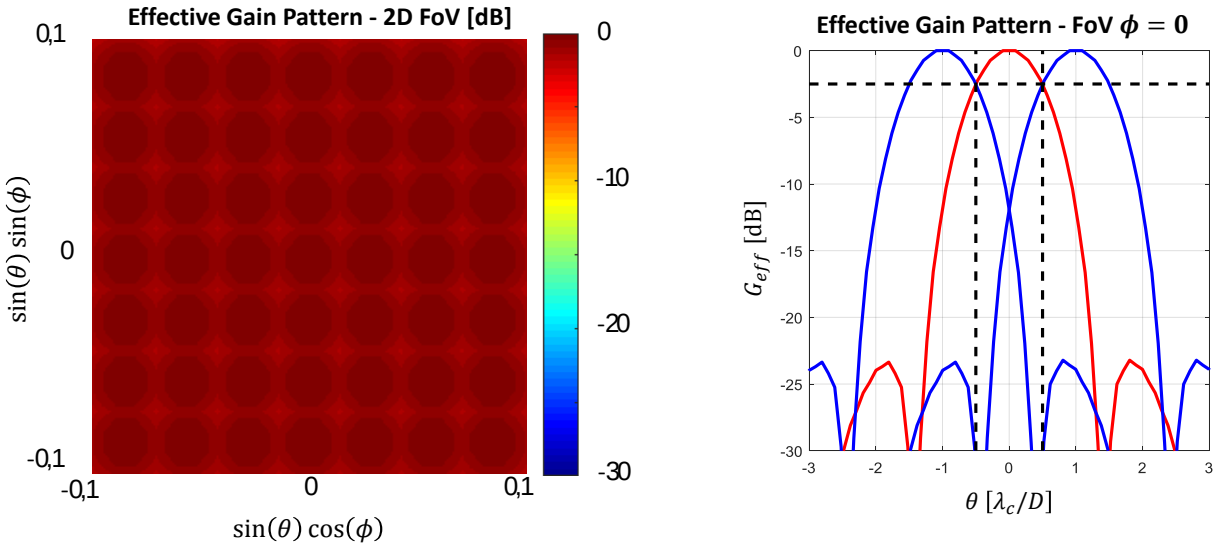

Figure 6.1: Effective gain pattern for the final design. Left: the FoV for the 7 by 7 prototype array as a 2D surface. Right: the FoV seen for ϕ is 0 degrees, for the center pixel and its adjacent pixels.

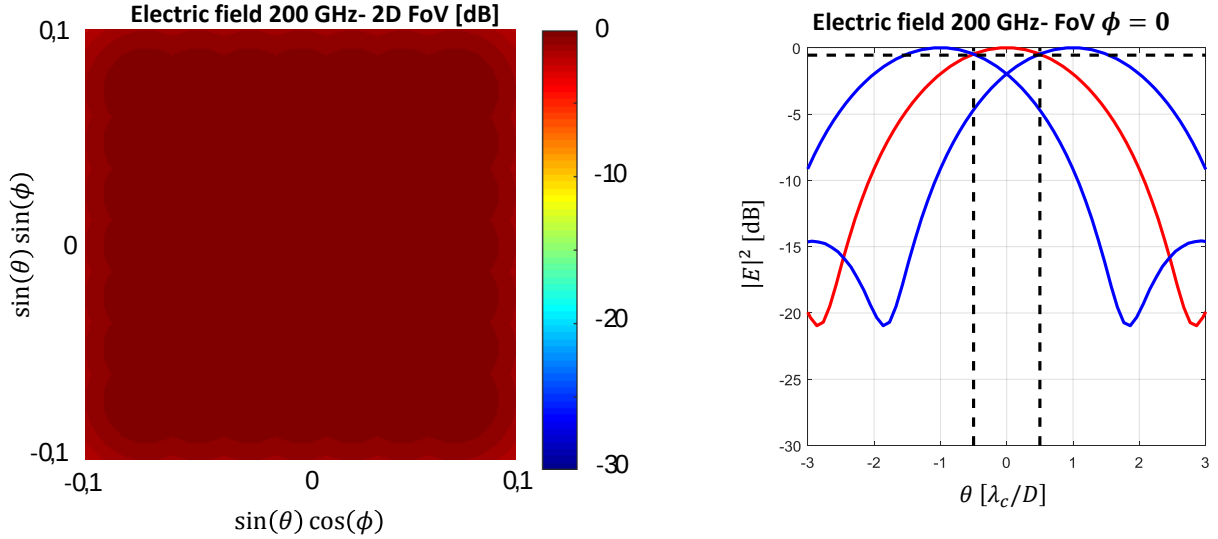

Figure 6.2: Electric field at 200 GHz for the final design. Left: the FoV for the 7 by 7 prototype array as a 2D surface. Right: the FoV seen for ϕ is 0 degrees, for the center pixel and its adjacent pixels.

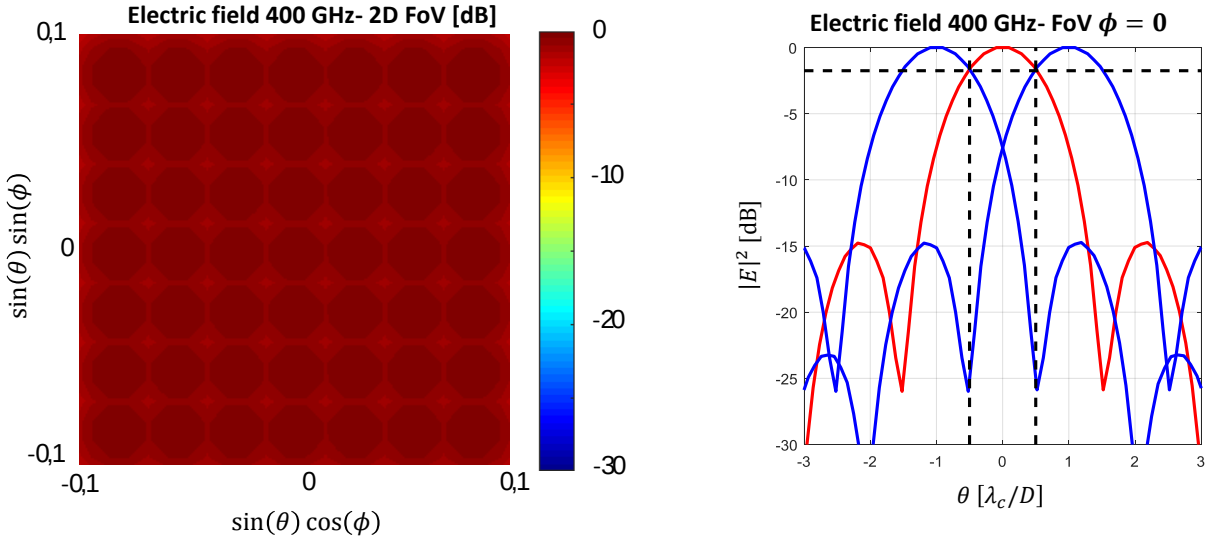

Figure 6.3: Electric field at 400 GHz for the final design. Left: the FoV for the 7 by 7 prototype array as a 2D surface. Right: the FoV seen for ϕ is 0 degrees, for the center pixel and its adjacent pixels.

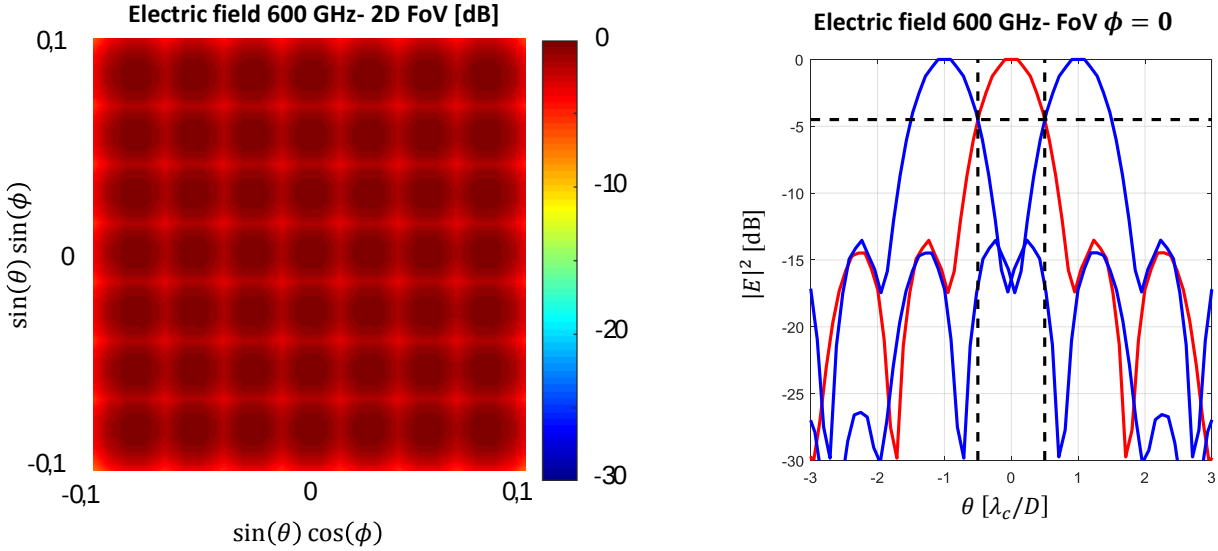

Figure 6.4: Electric field at 600 GHz for the final design. Left: the FoV for the 7 by 7 prototype array as a 2D surface. Right: the FoV seen for ϕ is 0 degrees, for the center pixel and its adjacent pixels.

6.2 Sensitivity

The sensitivity can be calculated from Eq. (2.19) and under the conditions found in the final design it is equal to 0.58 K at 10 Hz refresh rate, sufficient to meet the required sub-Kelvin sensitivity in the case of distributed sources without atmospheric attenuation. The NETD for scenarios with atmospheric attenuation taken into account is calculated

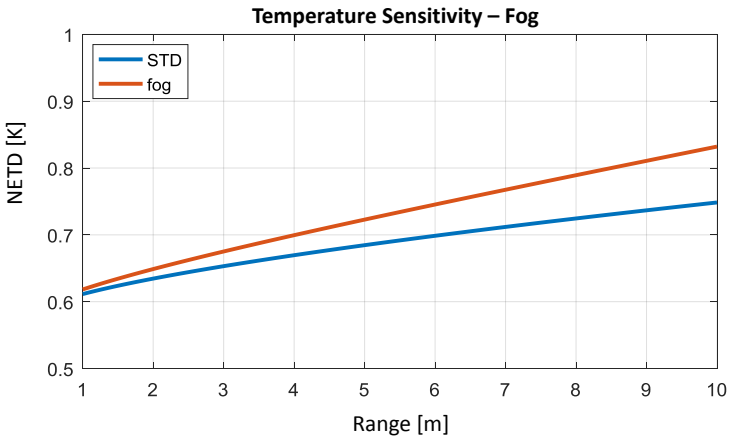

Figure 6.5: NETD as a function of distance under standard and fog conditions.

with Eq. (3.1) and is shown in Fig. 6.5, this shows that the NETD is sub-Kelvin for both standard and fog conditions, the average NETD is 0.73 K over the whole distance range for the fog conditions.

Now by also including the coupling efficiency, the pixel dependent NETD, is found in Fig. 6.6 for both the prototype and the full array. This shows a sufficient NETD to be able to detect the pedestrian at all distances as has been analyzed in Chapter 3.

This shows that the final design meets the requirements to have sub-Kelvin sensitivity at real-time refresh rate.

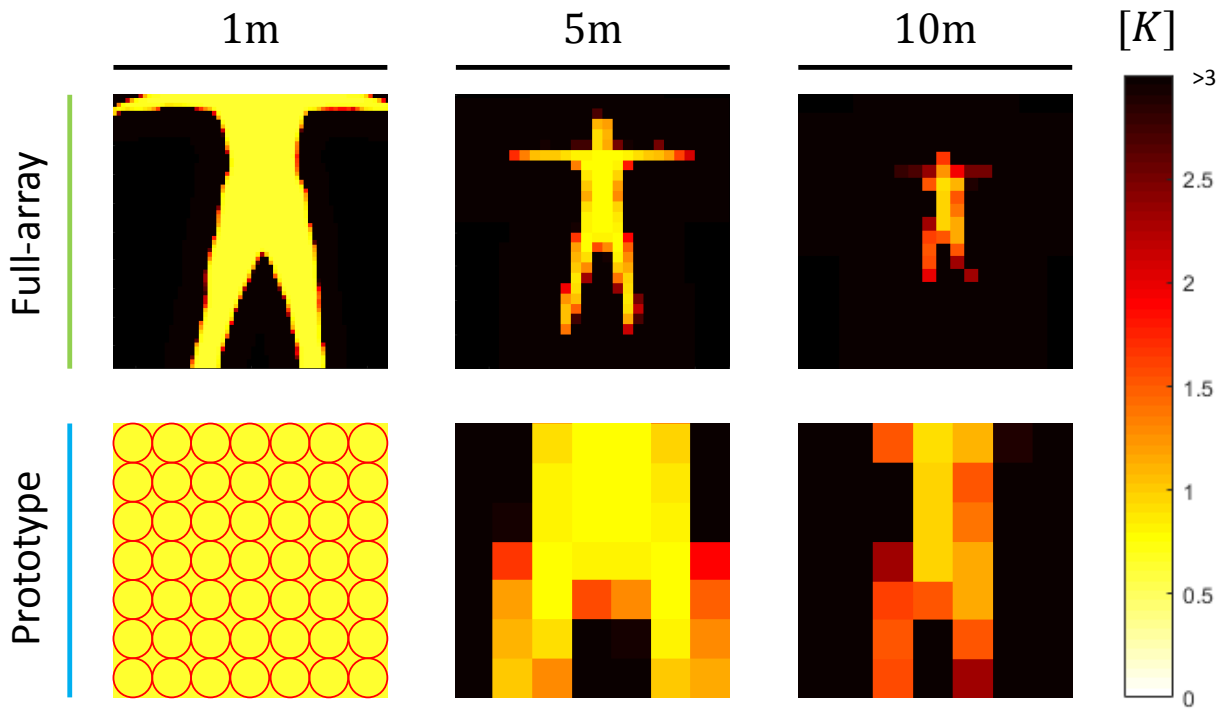

Figure 6.6: Sensitivity of the final design in detecting a pedestrian 1, 5 and 10 meters away and for both the prototype and the full array configuration.

Chapter 7

Conclusion and Future Work

7.1 Summary and Conclusion

The scope of this thesis was the development of the FPA for a low-cost, low-power and compact terahertz imager for pedestrian detection in automotive applications. An analysis and optimization of the FPA combined with the application is made to conclude with a proposed design and its expected performance.

Chapter 1 introduced the scope on THz imagers and what the benefits are of using them. A first mention is made on the performance of the system in terms of sensitivity. It is shown that the focus is around uncooled detectors with higher NEPs than cryogenically cooled detectors, which is compensated for by increasing the effective bandwidth. It is shown that with the effective bandwidth of a few hundred GHz and NEPs in the order of $pW/\sqrt{Hz}$ sub-Kelvin sensitivity at real time refresh rates can be achieved.

Chapter 2 clarified the figures of merits that are needed in passive terahertz imaging. It showed the imager is based on the detection of Back-Body radiation and that for this application the Rayleigh-Jeans limit applies. The received power is shown by explaining all efficiency terms that are taken into consideration. Different focal plane architectures are introduced that will imply tradeoffs between sensitivity and imaging resolution.

In chapter 3 the application was analyzed using a scenario of a pedestrian placed in front of a car under foggy atmospheric conditions. Also the influence on the sensitivity of the coupling between the source and the radiation pattern was explained. The requirements for scanning angle and detections are set, then the performance of typical sampling configurations is shown. From the expected sensitivity and angular resolution is concluded that the sampling of choice is field sampling ($1F_{\#}\lambda_c$). Also it is decided to make limited size prototype with less pixels instead of making an expensive full array design.

Chapter 4 then showed possible solutions for designing a broadband THz antenna for the FPA. The decision is made to design a connected array of elements and the quasi-analytical model used for the array optimization is derived for arrays of connected dipoles and connected slots.

In chapter 5 the optimization is explained. First the performance of the different structures in the previous chapter is analyzed using the derived analytical models. Then the array is implemented and optimized in CST to validate the complete array behavior. A proposal is made for the geometry of the array of connected dipoles and the performance is optimized further by tapering the dipoles, also the efficiency of the system is shown.

Chapter 6 showed the performance of the proposed array in effective gain pattern and sensitivity. It showed that the proposed FPA design results in sub-Kelvin sensitivity at real-time refresh rate. The design was able to achieve a average NETD of 0.73 K over the whole range for distributed sources at real-time refresh rate with foggy conditions, with an effective bandwidth of 172.2 GHz.

This thesis has been done a part of the TICAM research project. While being supervised by ir. Sven van Berkel, I performed an analysis of connected elements and used it to optimize it for the pedestrian detection application.

7.2 Future Work

The proposed design for the array of connected elements will be suitable for the first multi-pixel model of the TICAM. At the moment the single-pixel model is developed which means that still some effort has to be spend on making the transition towards prototype with multiple pixels possible. Extend research has to be done on manufacturing the array with detectors and how it is integrated on a system engineering level.
The techniques used in this thesis depend on the technology used, but changing the stratification could results in other geometric parameters than the ones found here.

Appendix A

CMOS Layer Topology

This appendix contains the information about the used simplified stratified CMOS technology. The exact stratification is not published.

A.1 Complete CMOS Layering

Figure A.1 contains a abstract overview of the layered stratification of the used complete CMOS technology; The exact stratification is not published.

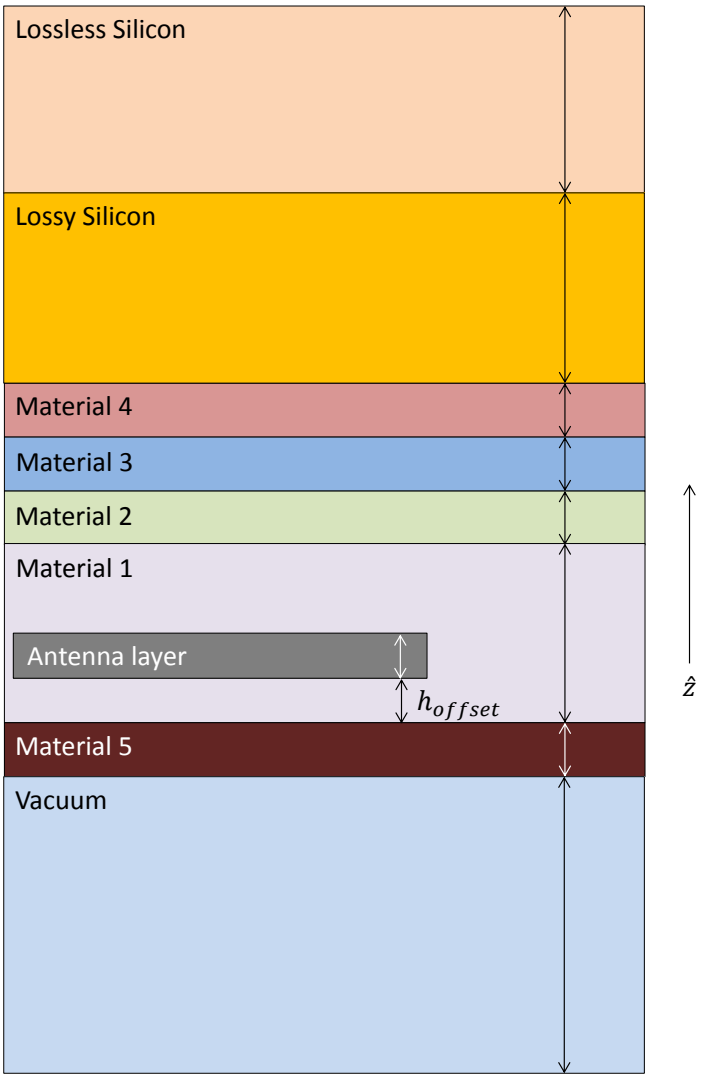

Figure A.1: The complete CMOS stratification used, with h_{offset} equal to 1.2 [μm].

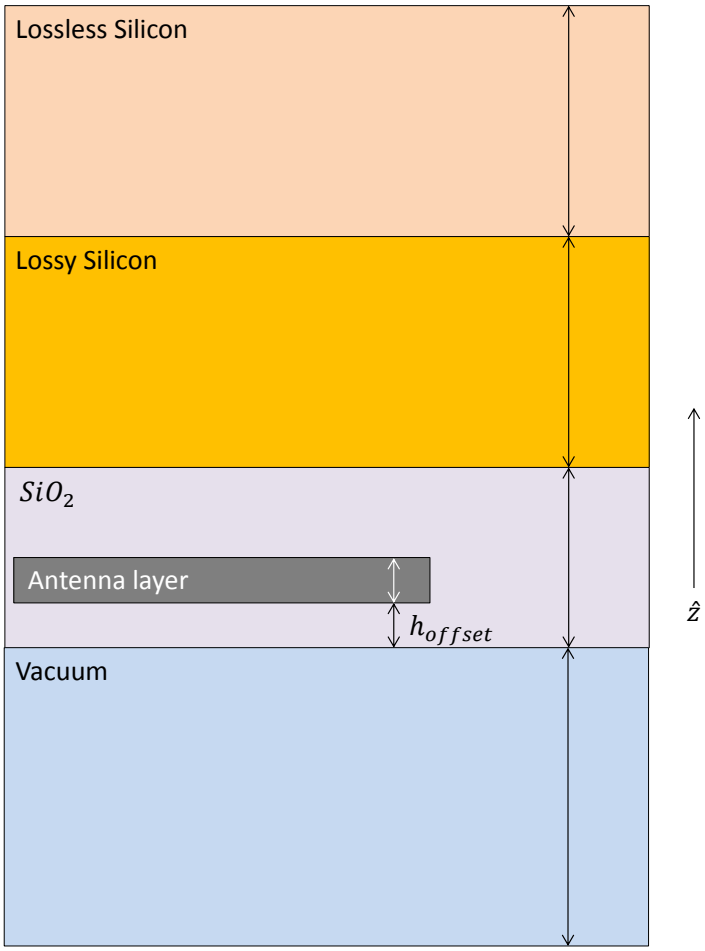

Figure A.2: The simplified CMOS stratification used, with h_{offset} equal to 1.2 $[\mu m]$.

A.2 Simplified CMOS Layering

Fig. A.2 contains a abstract overview of the simplified layered stratification of the used CMOS technology; table A.1 contains the parameters of the used materials.

Material name	Layer thickness $[\mu m]$	ϵ_r	Conductivity property
Antenna layer	2.8	n.a.	$\sigma = 3.53 * 10^7$ $[S/m]$
Lossy Silicon	150	11.9	$\sigma = 10$ $[S/m]$
Lossless Silicon	∞	11.9	n.a.
Vacuum	∞	1	n.a.
SiO_2	7.07	4.2	$\tan\delta = 0.002$ $[S/m]$

Table A.1: Parameters for the materials used in figure A.2.

Appendix B

Algebraical Steps for Connected Arrays

This chapter contains some algebraical steps done in the analysis of connected elements.

B.1 Longitudinal Green's Function for a Single Dipole

Rewriting Eq. (4.7) to find:

$$\vec{e}_{scat} = \int_{-\infty}^{\infty} i(x') \underbrace{\left(\int_{-\infty}^{\infty} g_{xx}^{EJ}(x-x', y-y') j_t(y') dy' \right)}_{d(x-x')} dx' \tag{B.1}$$

where $d(x-x')$ is the longitudinal spatial Green's function in the presence of the dipole; this can be calculated in the spectral domain. The transverse electric current distribution is expressed as:

$$j_t(y') = \frac{2}{w_s \pi} \frac{1}{\sqrt{1 - \left(\frac{2y'}{w_s}\right)}} \,. \tag{B.2}$$

To find the spectral form of $d(x-x')$, $D(k_x)$, the spatial Green's function is written as the double inverse Fourier transform of the spectral form and closing the integral in y' (with $FT\{j_t(y')\} = J_0\left(\frac{k_y w_s}{2}\right)$) to find:

$$d(x-x') = \frac{1}{2\pi} \int_{-\infty}^{\infty} \left(\frac{1}{2\pi} \int_{-\infty}^{\infty} G_{xx}^{EJ}(k_x, k_y) J_0\left(\frac{k_y w_s}{2}\right) dk_y \right) e^{-jk_x(x-x')} dk_x \tag{B.3}$$

which can be rewritten as $d(x-x') = \frac{1}{2\pi}\int_{-\infty}^{\infty} D(k_x)e^{-jk_x(x-x')}dk_x$ with:

$$D(k_x) = \frac{1}{2\pi}\int_{-\infty}^{\infty} G_{xx}^{EJ}(k_x,k_y)J_0\left(\frac{k_y w_s}{2}\right)dk_y\,. \tag{B.4}$$

B.2 Longitudinal Green's Function for a Double Dipole

Rewriting Eq. (4.27) observed for both dipoles gives:

$$\vec{e}_{scat} = \int_{-\infty}^{\infty} i(x') \underbrace{\left(\int_{-\infty}^{\infty}\sum_{n_s\in\{-1,1\}} g_{xx}^{EJ}(x-x',-\frac{d_s}{2}-y')j_t(y'-n_s\frac{d_s}{2})dy'\right)}_{d^-(x-x')} dx' \tag{B.5}$$

$$\vec{e}_{scat} = \int_{-\infty}^{\infty} i(x') \underbrace{\left(\int_{-\infty}^{\infty}\sum_{n_s\in\{-1,1\}} g_{xx}^{EJ}(x-x',\frac{d_s}{2}-y')j_t(y'-n_s\frac{d_s}{2})dy'\right)}_{d^+(x-x')} dx' \tag{B.6}$$

where $d^-(x-x')$ and $d^+(x-x')$ denote the longitudinal spatial Green's function observed at the lower and the upper dipole respectively; both can be calculated in the spectral domain. The transverse current distribution follows a edge-singular distribution (Eq. (B.2)), translated to the location of the dipoles. Starting with the lower dipole ($d^-(x-x')$), to find the spectral longitudinal Green's function, $D^-(k_x)$, the spatial GF is written as a double inverse Fourier transform (IFT) of the spectral form and closing the integral in y' (with $FT\{j_t(y')\} = J_0\left(\frac{k_y w_s}{2}\right)$) to find:

$$d^-(x-x') = \frac{1}{2\pi}\int_{-\infty}^{\infty}\left(\frac{1}{2\pi}\int_{-\infty}^{\infty}\sum_{n_s\in\{-1,1\}} G_{xx}^{EJ}(k_x,k_y)J_0\left(\frac{k_y w_s}{2}\right)e^{jk_y\left(n_s\frac{d_s}{2}+\frac{d_s}{2}\right)}dk_y\right)e^{-jk_x(x-x')}dk_x \tag{B.7}$$

which can be rewritten as $d^-(x-x') = \frac{1}{2\pi}\int_{-\infty}^{\infty} D^-(k_x)e^{-jk_x(x-x')}dk_x$ with:

$$D^-(k_x) = \frac{1}{2\pi}\int_{-\infty}^{\infty} G_{xx}^{EJ}(k_x,k_y)J_0\left(\frac{k_y w_s}{2}\right)\left[e^{jk_y d_s}+1\right]dk_y\,. \tag{B.8}$$

To continue with the upper dipole ($d^+(x-x')$), finds the spectral longitudinal Green's function $D^+(k_x)$, the spatial GF is written as a double inverse Fourier transform of the spectral form and closing the integral in y' (with $FT\{j_t(y')\} = J_0\left(\frac{k_y w_s}{2}\right)$) to find:

$$d^+(x-x') = \frac{1}{2\pi}\int_{-\infty}^{\infty}\left(\frac{1}{2\pi}\int_{-\infty}^{\infty}\sum_{n_s=-1/2}^{1/2} G_{xx}^{EJ}(k_x,k_y)J_0\left(\frac{k_y w_s}{2}\right)e^{jk_y\left(n_s d_s-\frac{d_s}{2}\right)}dk_y\right)e^{-jk_x(x-x')}dk_x \tag{B.9}$$

which can be rewritten as $d^+(x-x') = \frac{1}{2\pi}\int_{-\infty}^{\infty} D^+(k_x)e^{-jk_x(x-x')}dk_x$ with:

$$D^+(k_x) = \frac{1}{2\pi}\int_{-\infty}^{\infty} G_{xx}^{EJ}(k_x,k_y)J_0\left(\frac{k_y w_s}{2}\right)\left[1+e^{-jk_y d_s}\right]dk_y \tag{B.10}$$

which shows that the Green's functions are identical for both observations, $D^-(k_x) = D^+(k_x)$, concluding in the general expression for both dipoles:

$$D(k_x) = \frac{1}{2\pi}\int_{-\infty}^{\infty} G_{xx}^{EJ}(k_x,k_y)J_0\left(\frac{k_y w_s}{2}\right)\left[1+e^{-jk_y d_s}\right]dk_y\,. \tag{B.11}$$

B.3 Admittance Matrix for a Double Dipole

Starting with the α currents, combining Eq. (4.30) and (4.31) and close the integral in x to find:

$$\begin{aligned} i^{\alpha}_{\delta,n'_p} = \frac{1}{2\pi}\int_{-\infty}^{\infty}\frac{\mathrm{sinc}^2\left(\frac{k_x\delta}{2}\right)}{D(k_x)}e^{\frac{jk_x d_\delta}{2}}\Bigg(&-2V_0\left[e^{\frac{jk_x d_\delta}{2}}+e^{-\frac{jk_x d_\delta}{2}}\right] \\ &+ Z_l\sum_{n_p=-\frac{N_p-1}{2}}^{\frac{N_p-1}{2}}\left[i^{\alpha}_{\delta,n'_p}e^{-\frac{jk_x d_\delta}{2}}+i^{\beta}_{\delta,n'_p}e^{\frac{jk_x d_\delta}{2}}\right]e^{jk_x n_p d_p}\Bigg)e^{-jk_x n'_p d_p}dk_x\,. \end{aligned} \tag{B.12}$$

In this equation, four terms are distinguished: From the fed α gap to the observed current in the α gap of n'_p; From the fed β gap to the observed current in the α gap of n'_p; From the induced currents in the other α gaps to the observed current in the α gap of n'_p; From the induced currents in the other β gaps to the observed current in the α gap of n'_p. Written in formula form as:

$$i^{\alpha}_{\delta,n'_p} = V_0\left[Y^{\alpha\alpha}_{n'_p,0}+Y^{\alpha\beta}_{n'_p,0}\right] + Z_l\sum_{n_p=-\frac{N_p-1}{2}}^{\frac{N_p-1}{2}}\left[i^{\alpha}_{\delta,n_p}Y^{\alpha\alpha}_{n'_p,n_p}+i^{\beta}_{\delta,n_p}Y^{\alpha\beta}_{n'_p,n_p}\right] \tag{B.13}$$

with

$$Y^{\alpha\alpha}_{n'_p,n_p} = -\frac{1}{2\pi}\int_{-\infty}^{\infty}\frac{\mathrm{sinc}^2\left(\frac{k_x\delta}{2}\right)}{D(k_x)}e^{jk_x\left(n_p-n'_p\right)d_p}dk_x \tag{B.14}$$

$$Y^{\alpha\beta}_{n'_p,n_p} = -\frac{1}{2\pi}\int_{-\infty}^{\infty}\frac{\mathrm{sinc}^2\left(\frac{k_x\delta}{2}\right)}{D(k_x)}e^{jk_x d_\delta}e^{jk_x\left(n_p-n'_p\right)d_p}dk_x\,. \tag{B.15}$$

These steps are now repeated for the β currents. Combining Eq. (4.30) and (4.32) and close the integral in x to find:

$$i^{\beta}_{\delta,n'_p} = \frac{1}{2\pi}\int_{-\infty}^{\infty} \frac{\operatorname{sinc}^2\left(\frac{k_x\delta}{2}\right)}{D(k_x)} e^{-\frac{jk_xd_\delta}{2}} \Bigg(-2V_0\left[e^{\frac{jk_xd_\delta}{2}} + e^{-\frac{jk_xd_\delta}{2}}\right] + Z_l \sum_{n_p=-\frac{N_p-1}{2}}^{\frac{N_p-1}{2}} \left[i^{\alpha}_{\delta,n'_p} e^{-\frac{jk_xd_\delta}{2}} + i^{\beta}_{\delta,n'_p} e^{\frac{jk_xd_\delta}{2}}\right] e^{jk_xn_pd_p} \Bigg) e^{-jk_xn'_pd_p} dk_x\,. \tag{B.16}$$

In this equation, four terms are distinguished: From the fed α gap to the observed current in the β gap of n'_p; From the fed β gap to the observed current in the β gap of n'_p; From the induced currents in the other α gaps to the observed current in the β gap of n'_p; From the induced currents in the other β gaps to the observed current in the β gap of n'_p. Written in formula form as:

$$i^{\beta}_{\delta,n'_p} = V_0\left[Y^{\beta\alpha}_{n'_p,0} + Y^{\beta\beta}_{n'_p,0}\right] + Z_l \sum_{n_p=-\frac{N_p-1}{2}}^{\frac{N_p-1}{2}} \left[i^{\alpha}_{\delta,n_p} Y^{\beta\alpha}_{n'_p,n_p} + i^{\beta}_{\delta,n_p} Y^{\beta\beta}_{n'_p,n_p}\right] \tag{B.17}$$

with

$$Y^{\beta\alpha}_{n'_p,n_p} = -\frac{1}{2\pi}\int_{-\infty}^{\infty} \frac{\operatorname{sinc}^2\left(\frac{k_x\delta}{2}\right)}{D(k_x)} e^{-jk_xd_\delta} e^{jk_x\left(n_p-n'_p\right)d_p} dk_x \tag{B.18}$$

$$Y^{\beta\beta}_{n'_p,n_p} = -\frac{1}{2\pi}\int_{-\infty}^{\infty} \frac{\operatorname{sinc}^2\left(\frac{k_x\delta}{2}\right)}{D(k_x)} e^{jk_x\left(n_p-n'_p\right)d_p} dk_x\,. \tag{B.19}$$

Combining the terms from Eq. (B.14), (B.15), (B.18) and (B.19) to construct the admittance matrix as:

$$\boldsymbol{Y} = \begin{bmatrix} \boldsymbol{Y}^{\alpha\alpha} & \boldsymbol{Y}^{\alpha\beta} \\ \boldsymbol{Y}^{\beta\alpha} & \boldsymbol{Y}^{\beta\beta} \end{bmatrix} \text{ with } \quad \boldsymbol{Y}^{i,j} = \begin{bmatrix} Y^{ij}_{-\frac{N_p-1}{2},-\frac{N_p-1}{2}} & \cdots & Y^{ij}_{-\frac{N_p-1}{2},\frac{N_p-1}{2}} \\ \vdots & \ddots & \vdots \\ Y^{ij}_{\frac{N_p-1}{2},-\frac{N_p-1}{2}} & \cdots & Y^{ij}_{\frac{N_p-1}{2},\frac{N_p-1}{2}} \end{bmatrix}. \tag{B.20}$$

B.4 Longitudinal Green's Function for a Single Slot

Rewriting Eq. (D.8) to find:

$$\vec{h}_{scat} = \int_{-\infty}^{\infty} v(x') \underbrace{\left(\int_{-\infty}^{\infty} g_{xx}^{HM}(x-x', y-y') m_t(y') dy' \right)}_{d(x-x')} dx' \tag{B.21}$$

where $d(x-x')$ is the longitudinal spatial Green's function in the presence of the slot; this can be calculated in the spectral domain. The transverse magnetic current distribution is expressed as:

$$m_t(y') = -\frac{2}{w_s \pi} \frac{1}{\sqrt{1-\left(\frac{2y'}{w_s}\right)}} \,. \tag{B.22}$$

To find this spectral form of $d(x-x')$, $D(k_x)$, the spatial Green's function is written as the double inverse Fourier transform of the spectral form and closing the integral in y' (with $FT\{j_t(y')\} = J_0\left(\frac{k_y w_s}{2}\right)$) to find:

$$d(x-x') = \frac{1}{2\pi} \int_{-\infty}^{\infty} \left(\frac{1}{2\pi} \int_{-\infty}^{\infty} G_{xx}^{HM}(k_x, k_y) J_0\left(\frac{k_y w_s}{2}\right) dk_y \right) e^{-jk_x(x-x')} dk_x \tag{B.23}$$

which can be rewritten as $d(x-x') = \frac{1}{2\pi} \int_{-\infty}^{\infty} D(k_x) e^{-jk_x(x-x')} dk_x$ with:

$$D(k_x) = \frac{1}{2\pi} \int_{-\infty}^{\infty} G_{xx}^{HM}(k_x, k_y) J_0\left(\frac{k_y w_s}{2}\right) dk_y \,. \tag{B.24}$$

B.5 Longitudinal Green's Function for a Double Slot

Rewriting Eq. (D.28) observed for both slots gives:

$$\vec{h}_{scat} = \int_{-\infty}^{\infty} v(x') \underbrace{\left(\int_{-\infty}^{\infty} \sum_{n_s \in \{-1,1\}} g_{xx}^{HM}(x-x', -\frac{d_s}{2} - y') m_t(y' - n_s \frac{d_s}{2}) dy' \right)}_{d^-(x-x')} dx' \tag{B.25}$$

$$\vec{h}_{scat} = \int_{-\infty}^{\infty} v(x') \underbrace{\left(\int_{-\infty}^{\infty} \sum_{n_s \in \{-1,1\}} g_{xx}^{HM}(x-x', \frac{d_s}{2} - y') m_t(y' - n_s \frac{d_s}{2}) dy' \right)}_{d^+(x-x')} dx' \tag{B.26}$$

where $d^-(x-x')$ and $d^+(x-x')$ denote the longitudinal spatial Green's function observed at the lower and the upper slot respectively; both can be calculated in the spectral domain. The transverse current distribution follows a edge-singular distribution (Eq. (B.22)),

translated to the location of the slots. Starting with the lower slot ($d^-(x-x')$), to find the spectral longitudinal Green's function, $D^-(k_x)$, the spatial GF is written as a double inverse Fourier transform (IFT) of the spectral form and closing the integral in y' (with $FT\{m_t(y')\} = J_0\left(\frac{k_y w_s}{2}\right)$) to find:

$$d^-(x-x') = \frac{1}{2\pi}\int_{-\infty}^{\infty}\left(\frac{1}{2\pi}\int_{-\infty}^{\infty}\sum_{n_s\in\{-1,1\}} G_{xx}^{HM}(k_x,k_y)J_0\left(\frac{k_y w_s}{2}\right)e^{jk_y\left(n_s\frac{d_s}{2}+\frac{d_s}{2}\right)}dk_y\right)e^{-jk_x(x-x')}dk_x \tag{B.27}$$

which can be rewritten as $d^-(x-x') = \frac{1}{2\pi}\int_{-\infty}^{\infty} D^-(k_x)e^{-jk_x(x-x')}dk_x$ with:

$$D^-(k_x) = \frac{1}{2\pi}\int_{-\infty}^{\infty} G_{xx}^{HM}(k_x,k_y)J_0\left(\frac{k_y w_s}{2}\right)\left[e^{jk_y d_s}+1\right]dk_y\,. \tag{B.28}$$

To continue with the upper slot ($d^+(x-x')$), finds the spectral longitudinal Green's function, $D^+(k_x)$, the spatial GF is written as a double inverse Fourier transform of the spectral form and closing the integral in y' (with $FT\{m_t(y')\} = J_0\left(\frac{k_y w_s}{2}\right)$) to find:

$$d^+(x-x') = \frac{1}{2\pi}\int_{-\infty}^{\infty}\left(\frac{1}{2\pi}\int_{-\infty}^{\infty}\sum_{n_s\in\{-1,1\}} G_{xx}^{HM}(k_x,k_y)J_0\left(\frac{k_y w_s}{2}\right)e^{jk_y\left(n_s\frac{d_s}{2}-\frac{d_s}{2}\right)}dk_y\right)e^{-jk_x(x-x')}dk_x \tag{B.29}$$

which can be rewritten as $d^+(x-x') = \frac{1}{2\pi}\int_{-\infty}^{\infty} D^+(k_x)e^{-jk_x(x-x')}dk_x$ with:

$$D^+(k_x) = \frac{1}{2\pi}\int_{-\infty}^{\infty} G_{xx}^{HM}(k_x,k_y)J_0\left(\frac{k_y w_s}{2}\right)\left[1+e^{-jk_y d_s}\right]dk_y \tag{B.30}$$

which shows that the Green's functions are identical for both observations, $D^-(k_x) = D^+(k_x)$, concluding in the general expression for both slots:

$$D(k_x) = \frac{1}{2\pi}\int_{-\infty}^{\infty} G_{xx}^{HM}(k_x,k_y)J_0\left(\frac{k_y w_s}{2}\right)\left[1+e^{-jk_y d_s}\right]dk_y \tag{B.31}$$

B.6 Impedance Matrix for a Double Slot

Starting with the α voltages, combining Eq. (D.31) and (D.32) and close the integral in x to find:

$$\begin{aligned} v_{\delta,n'_p}^{\alpha} = \frac{1}{2\pi}\int_{-\infty}^{\infty}\frac{\mathrm{sinc}^2\left(\frac{k_x\delta}{2}\right)}{D(k_x)}e^{\frac{jk_x d_\delta}{2}}\Bigg(&-2I_0\left[e^{\frac{jk_x d_\delta}{2}}+e^{-\frac{jk_x d_\delta}{2}}\right] \\ &+Y_l\sum_{n_p=-\frac{N_p-1}{2}}^{\frac{N_p-1}{2}}\left[v_{\delta,n'_p}^{\alpha}e^{-\frac{jk_x d_\delta}{2}}+v_{\delta,n'_p}^{\beta}e^{\frac{jk_x d_\delta}{2}}\right]e^{jk_x n_p d_p}\Bigg)e^{-jk_x n'_p d_p}dk_x\,. \end{aligned} \tag{B.32}$$

In this equation, four terms are distinguished: From the fed α gap to the observed voltage in the α gap of n'_p; From the fed β gap to the observed voltage in the α gap of n'_p; From the induced voltages in the other α gaps to the observed voltage in the α gap of n'_p; From the induced voltages in the other β gaps to the observed voltage in the α gap of n'_p. Written in formula form as:

$$v^{\alpha}_{\delta,n'_p} = I_0 \left[Z^{\alpha\alpha}_{n'_p,0} + Z^{\alpha\beta}_{n'_p,0} \right] + Y_l \sum_{n_p=-\frac{N_p-1}{2}}^{\frac{N_p-1}{2}} \left[v^{\alpha}_{\delta,n_p} Z^{\alpha\alpha}_{n'_p,n_p} + v^{\beta}_{\delta,n_p} Z^{\alpha\beta}_{n'_p,n_p} \right] \tag{B.33}$$

with

$$Z^{\alpha\alpha}_{n'_p,n_p} = -\frac{1}{2\pi} \int_{-\infty}^{\infty} \frac{\operatorname{sinc}^2\left(\frac{k_x\delta}{2}\right)}{D(k_x)} e^{jk_x\left(n_p-n'_p\right)d_p} dk_x \tag{B.34}$$

$$Z^{\alpha\beta}_{n'_p,n_p} = -\frac{1}{2\pi} \int_{-\infty}^{\infty} \frac{\operatorname{sinc}^2\left(\frac{k_x\delta}{2}\right)}{D(k_x)} e^{jk_x d_\delta} e^{jk_x\left(n_p-n'_p\right)d_p} dk_x \,. \tag{B.35}$$

These steps are now repeated for the β voltages. Combining Eq. (D.31) and (D.33) and close the integral in x to find:

$$\begin{aligned} v^{\beta}_{\delta,n'_p} = \frac{1}{2\pi} \int_{-\infty}^{\infty} \frac{\operatorname{sinc}^2\left(\frac{k_x\delta}{2}\right)}{D(k_x)} e^{-\frac{jk_x d_\delta}{2}} \Bigg(& -2I_0 \left[e^{\frac{jk_x d_\delta}{2}} + e^{-\frac{jk_x d_\delta}{2}} \right] \\ & + Y_l \sum_{n_p=-\frac{N_p-1}{2}}^{\frac{N_p-1}{2}} \left[v^{\alpha}_{\delta,n'_p} e^{-\frac{jk_x d_\delta}{2}} + v^{\beta}_{\delta,n'_p} e^{\frac{jk_x d_\delta}{2}} \right] e^{jk_x n_p d_p} \Bigg) e^{-jk_x n'_p d_p} dk_x \,. \end{aligned} \tag{B.36}$$

In this equation, four terms are distinguished: From the fed α gap to the observed voltage in the β gap of n'_p; From the fed β gap to the observed voltage in the β gap of n'_p; From the induced voltages in the other α gaps to the observed voltage in the β gap of n'_p; From the induced voltages in the other β gaps to the observed voltage in the β gap of n'_p. Written in formula form as:

$$v^{\beta}_{\delta,n'_p} = I_0 \left[Z^{\beta\alpha}_{n'_p,0} + Z^{\beta\beta}_{n'_p,0} \right] + Y_l \sum_{n_p=-\frac{N_p-1}{2}}^{\frac{N_p-1}{2}} \left[v^{\alpha}_{\delta,n_p} Z^{\beta\alpha}_{n'_p,n_p} + v^{\beta}_{\delta,n_p} Z^{\beta\beta}_{n'_p,n_p} \right] \tag{B.37}$$

with

$$Z^{\beta\alpha}_{n'_p,n_p} = -\frac{1}{2\pi} \int_{-\infty}^{\infty} \frac{\operatorname{sinc}^2\left(\frac{k_x\delta}{2}\right)}{D(k_x)} e^{-jk_x d_\delta} e^{jk_x\left(n_p-n'_p\right)d_p} dk_x \tag{B.38}$$

$$Z^{\beta\beta}_{n'_p,n_p} = -\frac{1}{2\pi} \int_{-\infty}^{\infty} \frac{\operatorname{sinc}^2\left(\frac{k_x\delta}{2}\right)}{D(k_x)} e^{jk_x\left(n_p-n'_p\right)d_p} dk_x \,. \tag{B.39}$$

Combining the terms from Eq. (B.34), (B.35), (B.38) and (B.39) to construct the impedance matrix as:

$$\boldsymbol{Z} = \begin{bmatrix} \boldsymbol{Z}^{\alpha\alpha} & \boldsymbol{Z}^{\alpha\beta} \\ \boldsymbol{Z}^{\beta\alpha} & \boldsymbol{Z}^{\beta\beta} \end{bmatrix} \text{ with } \quad \boldsymbol{Z}^{i,j} = \begin{bmatrix} Z^{ij}_{-\frac{N_p-1}{2},-\frac{N_p-1}{2}} & \cdots & Z^{ij}_{-\frac{N_p-1}{2},\frac{N_p-1}{2}} \\ \vdots & \ddots & \vdots \\ Z^{ij}_{\frac{N_p-1}{2},-\frac{N_p-1}{2}} & \cdots & Z^{ij}_{\frac{N_p-1}{2},\frac{N_p-1}{2}} \end{bmatrix}. \tag{B.40}$$

Appendix C

Spectral Green's Functions for Stratified Media

This chapter explains how spectral Greens Functions are calculated for stratified media, first describing the methods used, then giving the spectral Green's functions to be complete. In this appendix is assumed that the sources are not along $\hat{z}$ and placed in the xy-plane.

C.1 Equivalent Circuits

The theory on forming an equivalent transmission line problem from stratified media is found in [43]. To solve the spectral Green's functions, first the equivalent transmission line has to be determined, consisting of finding the equivalent transmission line and determining the equivalent source.
To find the equivalent transmission line, every layer is transformed into a transmission line section, as in Fig. C.1. The transmission line have the characteristic impedance from the corresponding material Z with the local wavenumber k and the length of the transmission line h corresponds to the thickness of the layer. To determine what source is used in the equivalent problem, electric sources are modeled as current source, magnetic sources are modeled as a voltage source. Then depending on the structure used in terms of the presence of decoupling planes (i.e. slots), the transmission line source is separated for above and below, this is visualized in Fig. C.2. When considering a slot antenna compared to the dipole antenna, the upper and the lower half-space are decoupled due to the metal layer separating them.

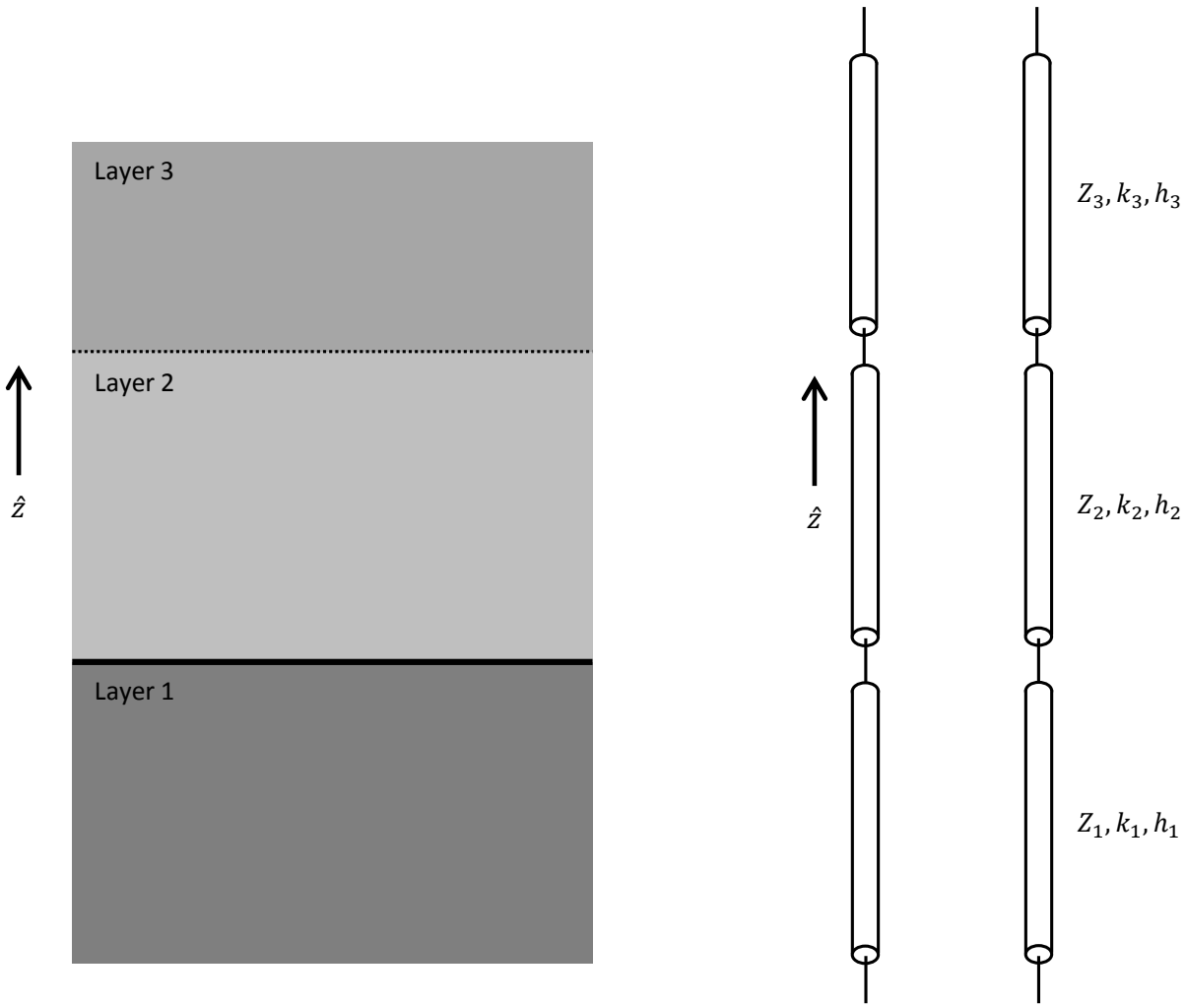

Figure C.1: Equivalent transmission line for a layered stratification of different mediums.

C.2 Calculating Potentials

To find the voltage and current potentials at the observation location, the first step is to calculate input impedance at the source location of the upper and lower half-space of the transmission line circuit. An infinite extended transmission line can be modeled as a load impedance equal to the characteristic impedance of the medium to the previous transmission line. This load can then be transformed to the beginning of the transmission line it is attached to by:

$$Z_{in} = Z_s \frac{Z_l + jZ_s \tan(h_i k_{zs})}{Z_s + jZ_l \tan(hk_{zs})} \tag{C.1}$$

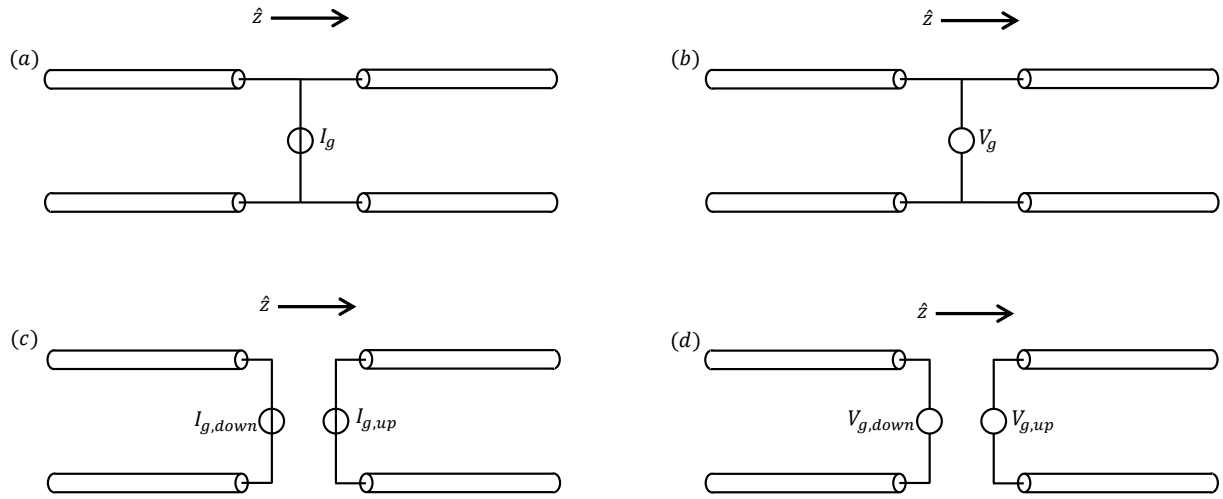

Figure C.2: Equivalent source for the equivalent transmission line problem for a: (a) electric source without decoupling plane; (b) magnetic source without decoupling plane; (c) electric source with decoupling plane; (d) magnetic source with decoupling plane.

where Z_s, k_{zs} and h are the characteristic impedance, the wave number and the height of the transmission line respectively; Z_l is the load impedance attached to the transmission line. This step can be repeated to transform the equivalent input impedance to the location of the source. This has to be done for the upper Z_{up} and the lower Z_{down} half plane.
These steps are done for both the trans-electric (TE) and trans-magnetic (TM) mode, which have different characteristic impedances for the media. Assuming medium i with characteristic impedance Z_i, the characteristic impedance for the TE-mode is $Z_i^{TE} = Z_i \frac{k_{zi}}{k_i}$ and for the TM-mode as $Z_i^{TE} = Z_i \frac{k_z}{k_{zi}}$. k_i is the wave number in medium i and $k_{zi} = \sqrt{k_i^2 - k_x^2 - k_y^2}$. Then the found potentials depend on the used source and the observed location , to calculate the potential at the source location, it can be seen in Fig. C.3. With this the first boundary condition at the location of the source is calculated.

When the observation location is not at the location of the source the potential needs to be calculated using the boundary conditions found. The potential found in each location is the summation of an upward going wave and a downward going wave as:

$$v(z) = V^+ \left(e^{-jk_z z} + \Gamma e^{jk_z z}\right) \tag{C.2}$$

$$i(z) = I^+ \left(e^{-jk_z z} + \Gamma e^{jk_z z}\right) \tag{C.3}$$

where Γ is the reflection coefficient between the two media (i and j) the wave is reflected from, calculated as:

$$\Gamma = \frac{Z_i - Z_j}{Z_i + Z_j} \tag{C.4}$$

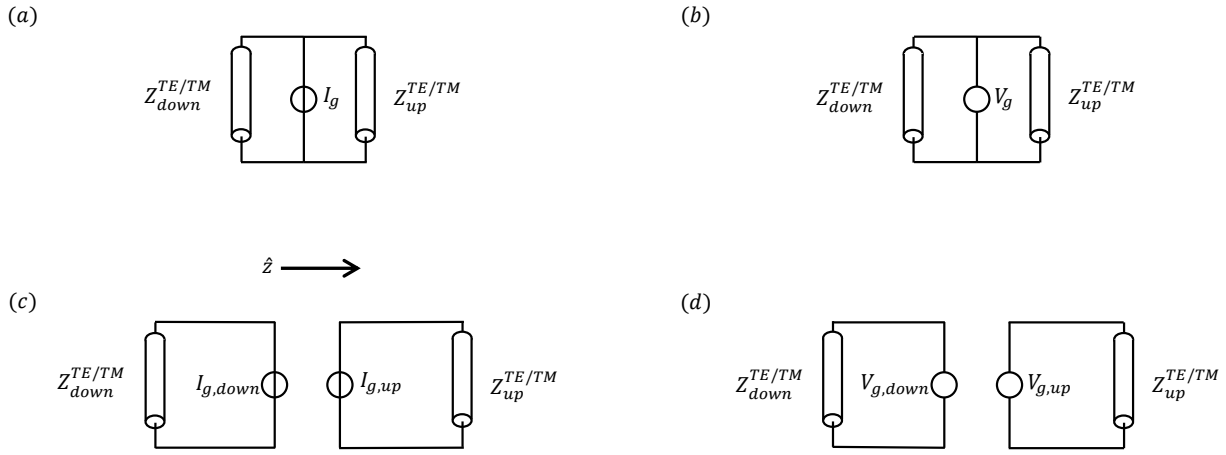

Figure C.3: Equivalent circuit at the source location a: (a) electric source without decoupling plane; (b) magnetic source without decoupling plane;(c) electric source with decoupling plane; (d) magnetic source with decoupling plane.

In the case a medium is infinitely extended, no reflected wave is present and Γ is equal to zero. Eq. (C.2) and (C.3) must be continuous on the boundaries between the media, using these boundaries conditions the potentials $i^{TE/TM}$ and $v^{TE/TM}$ can be calculated for the observation location. The are repeated for each medium layer until the layer in which the observation point is present is reached.

C.3 Spectral Green's Functions

The Green's functions for sources oriented along x or y and stratification along z can be used to calculate the electric or magnetic field:

$$\vec{f}(x,y,z) = \int\int \tilde{g}^{fc}(x,y,z;x',y',z')c(x',y',z')dx'dy' \tag{C.5}$$

where c donetes the type of current source, electric (j) or magnetic (m) and f the field component, electric (e) or magnetic (h). Where the Green's function can be generalized in the spectral domain as:

$$\tilde{g}^{fc}(x,y,z;x',y',z') = \frac{1}{(2\pi)^2}\int_{-\infty}^{\infty}\int_{-\infty}^{\infty}\tilde{G}^{fc}(k_x,k_y,z,z')e^{-jk_x(x-x')}e^{-jk_y(y-y')}dk_xdk_y\,. \tag{C.6}$$

The spectral green's function is a dyadic operation, since the sources are not oriented

along $\hat{z}$ here, the Green's function is a 3×2 dyad:

$$\tilde{G}^{fc}(k_x, k_y, z, z') = \begin{bmatrix} G_{xx}(k_x, k_y, z, z') & G_{xy}(k_x, k_y, z, z') \\ G_{yx}(k_x, k_y, z, z') & G_{yy}(k_x, k_y, z, z') \\ G_{zx}(k_x, k_y, z, z') & G_{zy}(k_x, k_y, z, z') \end{bmatrix}. \tag{C.7}$$

The expressions for the combinations between current sources and field components using the calculated potentials are given by:

$$\tilde{G}^{hm}(k_x, k_y, z, z') = \begin{bmatrix} \frac{-1}{k_\rho^2}\left(i^{TE}(k_\rho, z, z')k_x^2 + i^{TM}(k_\rho, z, z')k_y^2\right) & \frac{k_x k_y}{k_\rho^2}\left(i^{TM}(k_\rho, z, z') - i^{TE}(k_\rho, z, z')\right) \\ \frac{k_x k_y}{k_\rho^2}\left(i^{TM}(k_\rho, z, z') - i^{TE}(k_\rho, z, z')\right) & -\frac{-1}{k_\rho^2}\left(i^{TE}(k_\rho, z, z')k_y^2 + i^{TM}(k_\rho, z, z')k_x^2\right) \\ \frac{k_x}{k_{zs,i}Z_i^{TE}} v^{TE}(k_\rho, z, z') & \frac{k_y}{k_{zs,i}Z_i^{TE}} v^{TE}(k_\rho, z, z') \end{bmatrix} \tag{C.8}$$

$$\tilde{G}^{em}(k_x, k_y, z, z') = \begin{bmatrix} \frac{k_x k_y}{k_\rho^2}\left(v^{TM}(k_\rho, z, z') - v^{TE}(k_\rho, z, z')\right) & \frac{-1}{k_\rho^2}\left(v^{TM}(k_\rho, z, z')k_x^2 + v^{TE}(k_\rho, z, z')k_y^2\right) \\ \frac{1}{k_\rho^2}\left(v^{TM}(k_\rho, z, z')k_y^2 + v^{TE}(k_\rho, z, z')k_x^2\right) & \frac{k_x k_y}{k_\rho^2}\left(v^{TE}(k_\rho, z, z') - v^{TM}(k_\rho, z, z')\right) \\ -\frac{k_y Z_i^{TM}}{k_{zs,i}} i^{TM}(k_\rho, z, z') & \frac{k_x Z_i^{TM}}{k_{zs,i}} i^{TM}(k_\rho, z, z') \end{bmatrix} \tag{C.9}$$

$$\tilde{G}^{ej}(k_x, k_y, z, z') = \begin{bmatrix} \frac{-1}{k_\rho^2}\left(v^{TM}(k_\rho, z, z')k_x^2 + v^{TE}(k_\rho, z, z')k_y^2\right) & \frac{k_x k_y}{k_\rho^2}\left(v^{TE}(k_\rho, z, z') - v^{TM}(k_\rho, z, z')\right) \\ \frac{k_x k_y}{k_\rho^2}\left(v^{TE}(k_\rho, z, z') - v^{TM}(k_\rho, z, z')\right) & -\frac{-1}{k_\rho^2}\left(v^{TE}(k_\rho, z, z')k_y^2 + v^{TM}(k_\rho, z, z')k_x^2\right) \\ \frac{k_x}{k_{zs,i}} Z_i^{TM} i^{TM}(k_\rho, z, z') & \frac{k_y}{k_{zs,i}} Z_i^{TM} i^{TM}(k_\rho, z, z') \end{bmatrix} \tag{C.10}$$

$$\tilde{G}^{hj}(k_x, k_y, z, z') = \begin{bmatrix} \frac{k_x k_y}{k_\rho^2}\left(i^{TM}(k_\rho, z, z') - i^{TE}(k_\rho, z, z')\right) & \frac{-1}{k_\rho^2}\left(i^{TM}(k_\rho, z, z')k_y^2 + i^{TE}(k_\rho, z, z')k_x^2\right) \\ \frac{-1}{k_\rho^2}\left(i^{TM}(k_\rho, z, z')k_x^2 + i^{TE}(k_\rho, z, z')k_y^2\right) & \frac{k_x k_y}{k_\rho^2}\left(i^{TE}(k_\rho, z, z') - i^{TM}(k_\rho, z, z')\right) \\ \frac{k_y}{k_{zs,i}Z_i^{TE}} v^{TE}(k_\rho, z, z') & \frac{k_x}{k_{zs,i}Z_i^{TE}} v^{TE}(k_\rho, z, z') \end{bmatrix} \tag{C.11}$$

where i denotes the medium of observation and $k_\rho^2 = k_x^2 + k_y^2$

Appendix D

Connected Slot Analysis

This chapter explains the analysis of connected slots, similar that has been done in chapter 4.2.1 - 4.2.4 for dipoles.
First an analysis will be made of the surface currents present in a fed slot structure. Then a spectral analysis made from a single and double slot array.

D.1 Surface Currents

Before being able to solve Combined Magnetic Field Integral Equation for the slot, we have to use the equivalent principle that defines a problem with equivalent surface currents that flow on the slot. For this analysis the topology from Fig. D.1 is used. Where in Fig. D.1 (a) can be seen that the slot is fed on two location by an electric current, where this can be redefined using the equivalence theorem on surface around the slot, containing equivalent surface currents on a PEC (fig. 4.11 (b)).

Using the equivalent electric and magnetic currents to find the surface currents, respectively:

$$\vec{j}_s = \hat{n} \times \vec{h} \tag{D.1}$$

$$\vec{m}_s = -\hat{n} \times \vec{e} \tag{D.2}$$

where $\hat{n}$ is the normal on the surface S; $\vec{e}$ and $\vec{h}$ are the total electric field and total magnetic field present on the location of the surface.
On the metal of the slot, the metal is a perfect electric conductor (PEC), which makes the present electric field zero; no present magnetic surface currents. The magnetic field here will be non-zero, but when applying image theorem to remove the PEC, the image current cancels out the real current; no net magnetic current is present on the metal.

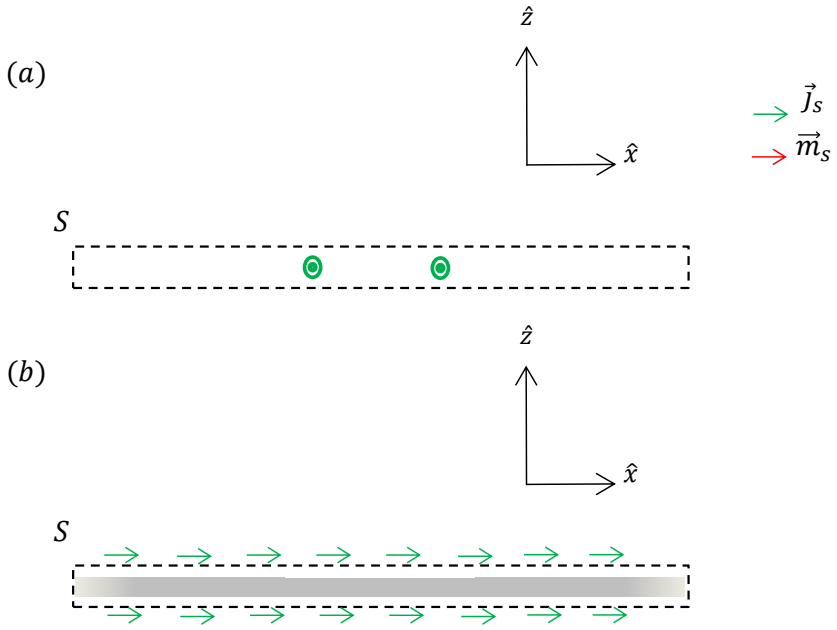

Figure D.1: Abstraction of a double fed slot with its equivalent surface currents. (a) Initial situation along the slot, fed on two location by an electric current. (b) Defined equivalent surface filled with PEC, S, along the slot, with equivalent electric and magnetic surface currents.

Observing *along the slot* sees that the electric field is continuous here; the equivalent magnetic surface currents on the upside and downside are equal but in opposite direction (Eq. (D.2)). Using $\hat{z} \times \left(\vec{h}^{+} - \vec{h}^{-}\right) = \vec{j}_{inc}$, and adding the current together as $m_s^{-} = -m_s^{+} = m_s$ then finds $\hat{z} \times (2m_s g_{metal}) = \vec{j}_{inc}$, where g_{metal} is the Green's function in the presence of the metal, which can be replaced by the free space Green's function by using the image theory to get $\hat{z} \times (4m_s g_{fs}) = \vec{j}_{inc}$. Concluding that only equivalent magnetic currents are present on the equivalent surface on the slot.

D.2 Single Slot Analysis

The analysis of the single fed slot follows the geometry given by Fig. D.2, were N_p is chosen to be always odd, designing the focal plane array having a unit cell in middle of the array and in the focus of the lens. For this slot the Magnetic Field Integral Equation (MFIE) is:

$$\vec{h}_{tot}(x, y, z) = \vec{h}_{scat}(x, y, z) + \vec{h}_{inc}(x, y, z) \tag{D.3}$$

where $\vec{h}_{tot}$ is the total magnetic field; $\vec{h}_{scat}$ is the scattered magnetic field and $\vec{h}_{inc}$ is the incident magnetic field. Assuming the slot is infinitely thin and observing at the z-location

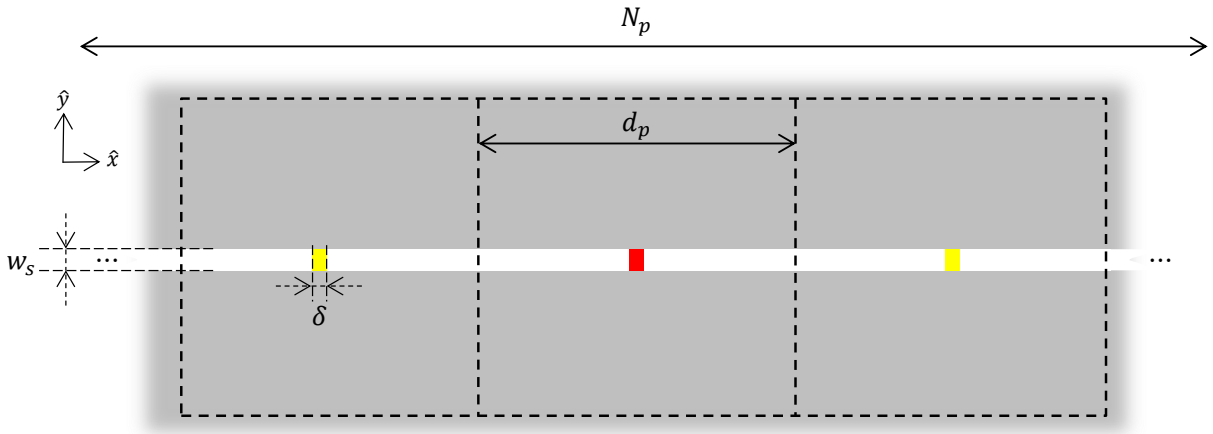

Figure D.2: Geometric configuration of the single slot with 1 delta-gap per unit cell. The distance d_p denotes the unit cell length, N_p is the total number of unit cells (odd), w_s is the width of the slot and δ is the width of the delta-gap feed.

of the micro strip ($z = 0$) becomes Eq. (D.3):

$$\vec{h}_{tot}(x, y) = \vec{h}_{scat}(x, y) + \vec{h}_{inc}(x, y)\,. \tag{D.4}$$

The slot is fed by a electric current source on the delta-gaps along $\hat{y}$:

$$\vec{j}_{inc} = \frac{I_0}{\delta}\mathrm{rect}_\delta\,(x)\,\hat{y}\,. \tag{D.5}$$

Using equivalence theorem ($\vec{j}_{inc} = \hat{n} \times \vec{h}_{inc} \equiv \vec{h}_{inc} = -\hat{n} \times \vec{j}_{inc}$) and the normal on the surface $\hat{n}$ being along $\hat{z}$ to write the incident magnetic field observed on the slot, assuming the slot is electrically narrow that the only relevant component is along $\hat{x}$, as:

$$\vec{h}_{inc}(x) = \frac{I_0}{\delta}\mathrm{rect}_\delta(x)\hat{x} \tag{D.6}$$

where I_0 is the feeding current. The total magnetic field is the product between the surface admittance (Y_l on the gaps and zero everywhere else) and the spatial surface voltage on the slot:

$$\vec{h}_{tot}(x) = \frac{Y_l}{\delta}\sum_{n_p=-(N_p-1)/2}^{(N_p-1)/2} v_{\delta,n_p}\mathrm{rect}_\delta(x - n_p d_p) \tag{D.7}$$

with v_{δ,n_p} is the average voltage on delta gap with index n_p. The scattered magnetic field is equal to the convolution of the spatial magnetic current distribution $m_x(x', y')$ (which is only along $\hat{x}$) and the spatial Green's Function (HM), g_{xx}^{HM} , as:

$$\vec{h}_{scat}(x) = \int_{-\infty}^{\infty}\int_{-\infty}^{\infty} g_{xx}^{HM}(x - x', y - y')m_x(x', y')dx'dy'\,. \tag{D.8}$$

The spatial magnetic current distribution is assumed to be the product of the longitudinal distribution, $v(x')$, and the transverse edge-singular distribution, $m_t(y')$, to find ,by following the steps from appendix B.4, the longitudinal spectral Green's function as:

$$D(k_x) = \frac{1}{2\pi}\int_{-\infty}^{\infty} G_{xx}^{HM}(k_x, k_y) J_0\left(\frac{k_y w_s}{2}\right) dk_y \,. \tag{D.9}$$

The calculation the spectral Green's Functions for stratified media is explained in appendix C. Using the identity from Eq. (4.9), to rewrite the MFIE from Eq. (D.4) as:

$$\int_{-\infty}^{\infty} V(k_x) D(k_x) e^{-jk_x x} dk_x = \int_{-\infty}^{\infty} \left(\operatorname{sinc}\left(\frac{k_x\delta}{2}\right)\left(-I_0 + Y_l \sum_{n_p=-(N_p-1)/2}^{(N_p-1)/2} v_{\delta,n_p} e^{jk_x n_p d_p}\right)\right) e^{-jk_x x} dk_x \tag{D.10}$$

where $V(k_x)$ is the voltage spectrum. Since this equation must be valid for every position x along the slot, the integrands has to be equal, finding the voltage spectrum as:

$$V(k_x) = \frac{\operatorname{sinc}\left(\frac{k_x\delta}{2}\right)}{D(k_x)}\left(-I_0 + Y_l \sum_{n_p=-(N_p-1)/2}^{(N_p-1)/2} v_{\delta,n_p} e^{jk_x n_p d_p}\right) . \tag{D.11}$$

By taking the inverse Fourier transform from this spectrum, the average voltage along gap n_p' can be found as:

$$v_{\delta,n_p'} = \frac{1}{\delta}\int_{n_p' d_p - \delta/2}^{n_p' d_p + \delta/2} v(x) dx = \frac{1}{\delta}\int_{n_p' d_p - \delta/2}^{n_p' d_p + \delta/2} \frac{1}{2\pi}\int_{-\infty}^{\infty} V(k_x) e^{-jk_x x} dk_x dx \tag{D.12}$$

$$v_{\delta,n_p'} = \frac{1}{2\pi}\int_{-\infty}^{\infty} \frac{\operatorname{sinc}^2\left(\frac{k_x\delta}{2}\right)}{D(k_x)}\left(-I_0 + Y_l \sum_{n_p=-(N_p-1)/2}^{(N_p-1)/2} v_{\delta,n_p} e^{jk_x n_p d_p}\right) e^{-jk_x n_p' d_p} dk_x \,. \tag{D.13}$$

Defining the mutual impedance from unit cell n_p to n_p' as:

$$Z_{n_p,n_p'} = -\frac{1}{2\pi}\int_{-\infty}^{\infty} \frac{\operatorname{sinc}^2\left(\frac{k_x\delta}{2}\right)}{D(k_x)} e^{-jk_x\left(n_p - n_p'\right)d_p} \tag{D.14}$$

substituted in Eq. (D.13):

$$v_{\delta,n_p'} = I_0 Z_{0,n_p'} - Y_l \sum_{n_p=-(N_p-1)/2}^{(N_p-1)/2} v_{\delta,n_p} Z_{n_p,n_p'} \,. \tag{D.15}$$

This can be written as a system of equations, calculating the voltage in each gap as:

$$\boldsymbol{I}\boldsymbol{v}_\delta = \boldsymbol{Z}\boldsymbol{i} - Y_l \boldsymbol{Z}\boldsymbol{v}_\delta \tag{D.16}$$

where $\boldsymbol{I}$ is an identity matrix of order N_p; $\boldsymbol{v}_\delta$ is the voltage vector; $\boldsymbol{Z}$ is the impedance matrix and $\boldsymbol{i}$ is the current vector (feeding), as:

$$\boldsymbol{v}_\delta = \begin{bmatrix} v_{\delta,-\frac{(N_p-1)}{2}} \\ \vdots \\ v_{\delta,\frac{(N_p-1)}{2}} \end{bmatrix} \tag{D.17}$$

$$\boldsymbol{Z} = \begin{bmatrix} Z_{-\frac{N_p-1}{2},-\frac{N_p-1}{2}} & \dots & Z_{-\frac{N_p-1}{2},\frac{N_p-1}{2}} \\ \vdots & \ddots & \vdots \\ Z_{\frac{N_p-1}{2},-\frac{N_p-1}{2}} & \dots & Z_{\frac{N_p-1}{2},\frac{N_p-1}{2}} \end{bmatrix} \tag{D.18}$$

$$\boldsymbol{i} = \begin{bmatrix} 0 \\ \vdots \\ I_0 \\ \vdots \\ 0 \end{bmatrix} \tag{D.19}$$

This system of equations can be solved for $\boldsymbol{v}_\delta$ as:

$$\boldsymbol{v}_\delta = [\boldsymbol{Z}^{-1} + Y_l \boldsymbol{I}]^{-1} \boldsymbol{i}\,. \tag{D.20}$$

The active input admittance of the port n_p is then defined as:

$$Y_{in,active} = \frac{i_{n_p}}{v_{\delta,n_p}} - Y_l\,. \tag{D.21}$$

The mutual coupling efficiency, η_{mc} , is the ratio between the power radiated by the fed unit cell, P_{rad}, and the total power P_{tot} (P_{rad} plus the power induced in all other present unit cells, P_{mc}):

$$\eta_{mc} = \frac{P_{rad}}{P_{rad} + P_{mc}}\,. \tag{D.22}$$

To calculated the power in all gaps, the circuits in Fig. D.3 are used. In Eq. (D.22) the radiated power is defined as:

$$P_{tot} = \frac{|v_{\delta,0}|^2}{2} Re\{Y_{0,act}\} \tag{D.23}$$

and the induced power as:

$$P_{mc} = Re\{Y_l\} \sum_{\substack{n_p = -\frac{N_p-1}{2} \\ n_p \neq 0}}^{(N_p-1)/2} \frac{|v_{\delta,n_p}|^2}{2} \tag{D.24}$$

To complete this analysis, now the same steps are performed for a double slot.

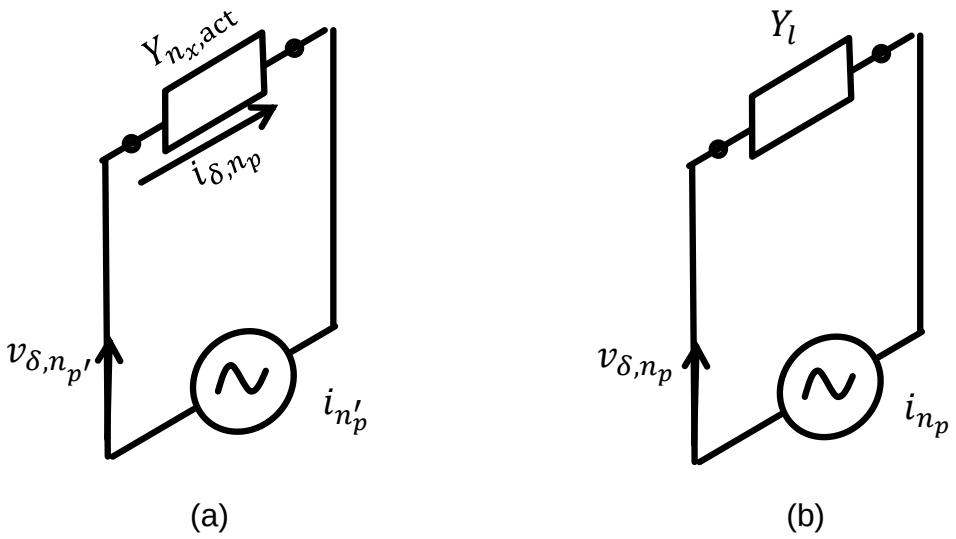

Figure D.3: Circuits that are used for the calculation of the power in the gaps of single slot: (a) The equivalent circuit for the fed delta-gap. (b) The equivalent circuit used for all non-fed delta-gaps.

D.3 Double Slot Analysis

The analysis of the double fed double slot follows the geometry given by Fig. D.4, were N_p is chosen to be always odd, designing the focal plane array having a pixel cell in middle of the array and in the focus of the lens. The distance between the slots, d_s, and the distance between the delta gaps on the same slot of the same unit cell, d_δ, are set to be equal.

For this configurations the MFIE is the same as for the single slot (Eq. (D.3)). Assuming the slots are infinitely thin and observing at the z-location of the micro strips ($z = 0$) the MFIE is equal to the one in Eq. (D.4).

The slots are fed by a electric current source on the delta-gaps along $\hat{y}$:

$$\vec{j}_{inc} = \frac{I_0}{\delta} \underbrace{\sum_{n_\delta \in \{-1,1\}} \mathrm{rect}_\delta \left(x + n_\delta \frac{d_\delta}{2} \right)}_{\text{double gap}} \underbrace{\sum_{n_s \in \{-1,1\}} \mathrm{rect}_{w_s} \left(y - n_s \frac{d_s}{2} \right)}_{\text{double slot}} \hat{y} \tag{D.25}$$

where I_0 is the feeding current. Using equivalence theorem ($\vec{j}_{inc} = \hat{n} \times \vec{h}_{inc} \equiv \vec{h}_{inc} = -\hat{n} \times \vec{j}_{inc}$) and the normal on the surface $\hat{n}$ being along $\hat{z}$ to write the incident magnetic field observed on the slots, assuming the slots are electrically narrow that the only relevant

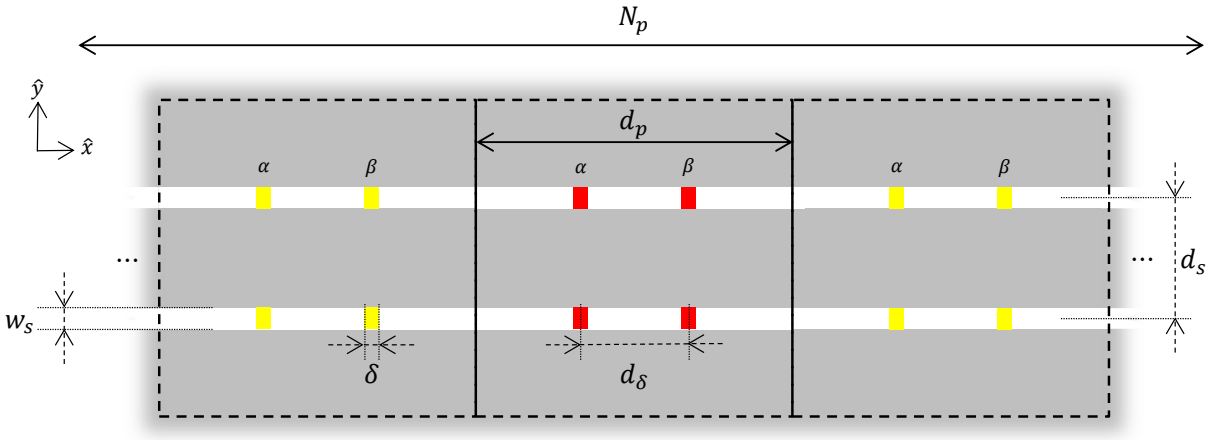

Figure D.4: Geometric configuration of the double slot with 2 delta-gap per unit cell per slot. The distance d_p denotes the unit cell length, N_p is the total number of unit cells (odd), w_s is the width of the slots and δ is the width of the delta-gap feeds, d_s is the distance between the slots and d_δ is the distance between the delta gaps on the same slot of the same unit cell.

component is along $\hat{x}$, as:

$$\vec{h}_{inc}(x) = \frac{I_0}{\delta} \sum_{n_\delta \in \{-1,1\}} \text{rect}_\delta \left(x + n_\delta \frac{d_\delta}{2} \right) \sum_{n_s \in \{-1,1\}} \text{rect}_{w_s} \left(y - n_s \frac{d_s}{2} \right) \hat{x} \,. \tag{D.26}$$

The total magnetic field is the product between the surface admittance (Y_l on the gaps and zero everywhere else) and the spatial magnetic surface current on the slots:

$$\vec{h}_{tot}(x) = \frac{Y_l}{\delta} \sum_{n_p=-(N_p-1)/2}^{(N_p-1)/2} \left[v^\alpha_{\delta,n_p} \text{rect}_\delta \left(x - n_p d_p + \frac{d_\delta}{2} \right) + v^\beta_{\delta,n_p} \text{rect}_\delta \left(x - n_p d_p - \frac{d_\delta}{2} \right) \right] \sum_{n_s \in \{-1,1\}} \text{rect}_{w_s} \left(y - n_s \frac{d_\delta}{2} \right) \tag{D.27}$$

with v^α_{δ,n_p} and v^β_{δ,n_p} is the average voltage in unit cell n_p of delta gap α and β respectively. The voltages are excited in phase and since only two slots are present, the voltages do not depend on the strip on which they are observed, but do depend on the unit cell.
The scattered magnetic field is equal to the convolution of the spatial magnetic current distribution $m_x(x', y')$ (which is only along $\hat{x}$) and the spatial Green's Function (HM), g^{HM}_{xx} , from both slots as:

$$\vec{h}_{scat}(x) = \sum_{n_s \in \{-1,1\}} \int_{-\infty}^{\infty} \int_{-\infty}^{\infty} g^{HM}_{xx}(x - x', y - y') m_x(x', y' - n_s \frac{d_s}{2}) dx' dy' \,. \tag{D.28}$$

The spatial current distribution is assumed to be the product of the longitudinal distribution, $v(x')$, and the transverse edge-singular distribution, $m_t(y')$, to find, by following the steps from appendix B.5, the longitudinal spectral Green's function as:

$$D(k_x) = \frac{1}{2\pi}\int_{-\infty}^{\infty} G_{xx}^{HM}(k_x,k_y) J_0\left(\frac{k_y w_s}{2}\right)\left[1+e^{-jk_y d_s}\right] dk_y\,. \tag{D.29}$$

The calculation the spectral Green's Functions for stratified media is explained in appendix C. To write the MFIE from Eq. (D.4) with Eq. (D.26), (D.27) and (D.28) and using the identity from Eq. (4.9) as:

$$\begin{aligned}\int_{-\infty}^{\infty} V(k_x)D(k_x)e^{-jk_x x}dk_x = \\ \int_{-\infty}^{\infty}\operatorname{sinc}\left(\frac{k_x\delta}{2}\right)\Bigg(-I_0\left[e^{-jk_x d_\delta}+e^{jk_x d_\delta}\right] \\ + Y_l\sum_{n_p=-(N_p-1)/2}^{(N_p-1)/2}\left[v_{\delta,n_p}^{\alpha}e^{-\frac{jk_x d_\delta}{2}}+v_{\delta,n_p}^{\beta}e^{\frac{jk_x d_\delta}{2}}\right]e^{jk_x n_p d_p}\Bigg)e^{-jk_x x}dk_x\end{aligned} \tag{D.30}$$

where $V(k_x)$ is the voltage spectrum. Since this integral must be valid for every position x along the slots the integrands must be equal to find the voltage spectrum as:

$$V(k_x) = \frac{\operatorname{sinc}\left(\frac{k_x\delta}{2}\right)}{D(k_x)}\left(-2I_0\cos\left(k_x d_\delta\right) + Y_l\sum_{n_p=-(N_p-1)/2}^{(N_p-1)/2}\left[v_{\delta,n_p}^{\alpha}e^{-\frac{jk_x d_\delta}{2}}+v_{\delta,n_p}^{\beta}e^{\frac{jk_x d_\delta}{2}}\right]e^{jk_x n_p d_p}\right)\,. \tag{D.31}$$

By taking the inverse Fourier transform from this spectrum, the average voltage along α and β gap n_p' can be found as:

$$v_{\delta,n_p'}^{\alpha} = \frac{1}{\delta}\int_{n_p' d_p-\frac{d_\delta}{2}-\delta/2}^{n_p' d_p-\frac{d_\delta}{2}+\delta/2} v(x)dx = \frac{1}{\delta}\int_{n_p' d_p-\frac{d_\delta}{2}-\delta/2}^{n_p' d_p-\frac{d_\delta}{2}+\delta/2}\frac{1}{2\pi}\int_{-\infty}^{\infty} V(k_x)e^{-jk_x x}dk_x dx \tag{D.32}$$

$$v_{\delta,n_p'}^{\beta} = \frac{1}{\delta}\int_{n_p' d_p+\frac{d_\delta}{2}-\delta/2}^{n_p' d_p+\frac{d_\delta}{2}+\delta/2} v(x)dx = \frac{1}{\delta}\int_{n_p' d_p+\frac{d_\delta}{2}-\delta/2}^{n_p' d_p+\frac{d_\delta}{2}+\delta/2}\frac{1}{2\pi}\int_{-\infty}^{\infty} V(k_x)e^{-jk_x x}dk_x dx\,. \tag{D.33}$$

The construction of the admittance matrix is found in appendix B.6. Using the equations found, a set systems of equations can be made:

$$\boldsymbol{I}\boldsymbol{v}_\delta = \boldsymbol{Z}\boldsymbol{i} - Y_l\boldsymbol{Z}\boldsymbol{v}_\delta \tag{D.34}$$

where $\boldsymbol{I}$ is an identity matrix of order $2N_p$; $\boldsymbol{v}_\delta$ is the voltage vector; $\boldsymbol{Z}$ is the impedance matrix and $\boldsymbol{i}$ is the current vector (feeding), as:

$$\boldsymbol{v_\delta} = \begin{bmatrix} \boldsymbol{v}_{\delta,\alpha} \\ \boldsymbol{v}_{\delta,\beta} \end{bmatrix} \text{ with } \quad \boldsymbol{v}_{\delta,\alpha} = \begin{bmatrix} v^{\alpha}_{\delta,-\frac{N_p-1}{2}} \\ \vdots \\ v^{\alpha}_{\delta,\frac{N_p-1}{2}} \end{bmatrix} \text{ and } \quad \boldsymbol{v}_{\delta,\beta} = \begin{bmatrix} v^{\beta}_{\delta,-\frac{N_p-1}{2}} \\ \vdots \\ v^{\beta}_{\delta,\frac{N_p-1}{2}} \end{bmatrix} \tag{D.35}$$

$$\boldsymbol{Z} = \begin{bmatrix} \boldsymbol{Z}^{\alpha\alpha} & \boldsymbol{Z}^{\alpha\beta} \\ \boldsymbol{Z}^{\beta\alpha} & \boldsymbol{Z}^{\beta\beta} \end{bmatrix} \text{ with } \quad \boldsymbol{Z}^{i,j} = \begin{bmatrix} Z^{ij}_{-\frac{N_p-1}{2},-\frac{N_p-1}{2}} & \cdots & Z^{ij}_{-\frac{N_p-1}{2},\frac{N_p-1}{2}} \\ \vdots & \ddots & \vdots \\ Z^{ij}_{\frac{N_p-1}{2},-\frac{N_p-1}{2}} & \cdots & Z^{ij}_{\frac{N_p-1}{2},\frac{N_p-1}{2}} \end{bmatrix} \tag{D.36}$$

$$\boldsymbol{i} = \begin{bmatrix} \boldsymbol{i}^{\alpha} \\ \boldsymbol{i}^{\beta} \end{bmatrix} \text{ with} \boldsymbol{i}^{\alpha} = \boldsymbol{i}^{\beta} \begin{bmatrix} 0 \\ \vdots \\ I_0 \\ \vdots \\ 0 \end{bmatrix} \tag{D.37}$$

This system of equations can be solved for $\boldsymbol{v}_\delta$ as:

$$\boldsymbol{v}_\delta = [\boldsymbol{Z}^{-1} + Y_l \boldsymbol{I}]^{-1} \boldsymbol{i}\,. \tag{D.38}$$

The active input admittance of the port n_p is then defined as:

$$Y_{in,active} = \frac{i_{n_p}}{v_{\delta,n_p}} - Y_l\,. \tag{D.39}$$

The mutual coupling efficiency, η_{mc} , is the ratio between the power radiated by the fed unit cell, P_{rad}, and the total power P_{tot} (P_{rad} plus the power induced in all other present unit cells, P_{mc}):

$$\eta_{mc} = \frac{P_{rad}}{P_{rad} + P_{mc}} \tag{D.40}$$

In Eq. (D.40) the total power is defined as:

$$P_{tot} = \frac{\left(|v^{\alpha}_{\delta,0}|^2 + |v^{\beta}_{\delta,0}|^2\right)}{2} Re\{Y_{in,active}\} \tag{D.41}$$

and the induced power as:

$$P_{mc} = Re\{Y_l\} \sum_{\substack{n_p = -\frac{N_p-1}{2} \\ n_p \neq 0}}^{(N_p-1)/2} \frac{\left(|v^{\alpha}_{\delta,n_p}|^2 + |v^{\beta}_{\delta,n_p}|^2\right)}{2} \tag{D.42}$$

D.4 Far Field of Slot Structures

To find the electric far field radiated by a slot structure, the asymptotic evaluation is used:

$$\vec{E}_{far}\left(\vec{r}_{obs}\right) = jk_{zs}\begin{bmatrix} G_{xx}^{EM}\left(k_{xs},k_{ys},z_{obs},z'\right) \\ G_{yx}^{EM}\left(k_{xs},k_{ys},z_{obs},z'\right) \\ G_{zx}^{EM}\left(k_{xs},k_{ys},z_{obs},z'\right) \end{bmatrix} V(k_{xs})M_t(k_{ys})e^{jk_{zs}|z_{obs}-z|}AF\frac{e^{-jkr}}{2\pi r} \tag{D.43}$$

where $\vec{r}_{obs}$ is the location of observation; $V(k_{xs})$ is the voltage spectrum (Eq. (D.11) for single slots and Eq. (D.31) for double slots); $M_t(k_{ys})$ is the transverse spectrum from the transverse edge-singular voltage distribution ($FT\{m_t(k_{ys})\} = J_0\left(\frac{k_{ys}w_s}{2}\right)$) and AF is the array factor along y (1 if a single slot is used; $2\cos\left(\frac{k_y d_s}{2}\right)$ when a double slot is used).

Appendix E

Validation

This chapter contains the validation done for different structure from the models derived for dipoles chapter 4 and for slots in appendix D.

E.1 Single Dipole

The verification is done using CST [24] for a single dipole structure with parameters: $F_{\#} = 0.6$; $w_s = 20\ \mu m$; $\delta = 15\ \mu m$ and $Z_l = 100\ \Omega$ using the stratification from appendix A.2 are show in Fig. E.1, E.2 and E.3 for respectively the far field, the active input impedance and the mutual coupling. For this simulation only one row of pixel is considered.

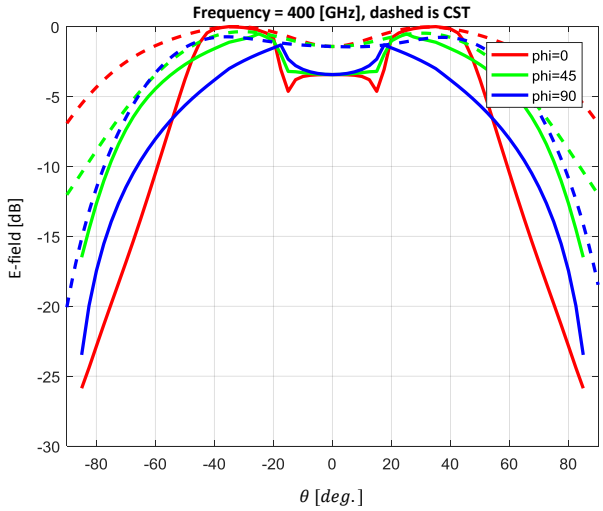

Figure E.1: Comparison between the integral equations and CST (the dashed lines) for the far field of a single dipole with $F_{\#} = 0.6$; $w_s = 20\ \mu m$; $\delta = 15\ \mu m$ and $Z_l = 100\ \Omega$ using the stratification from appendix A.2.

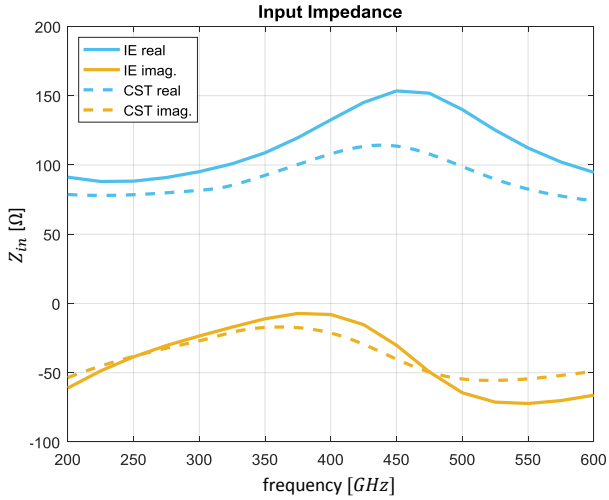

Figure E.2: Comparison between the integral equations and CST (the dashed lines) for the active input impedance of a single dipole with $F_{\#} = 0.6$; $w_s = 20\ \mu m$; $\delta = 15\ \mu m$ and $Z_l = 100\ \Omega$ using the stratification from appendix A.2.

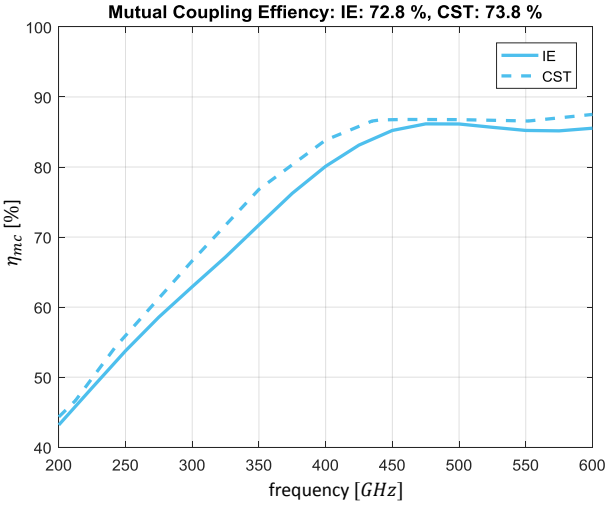

Figure E.3: Comparison between the integral equations and CST (the dashed lines) for the mutual coupling efficiency of a single dipole with $F_{\#} = 0.6$; $w_s = 20\ \mu m$; $\delta = 15\ \mu m$ and $Z_l = 100\ \Omega$ using the stratification from appendix A.2.

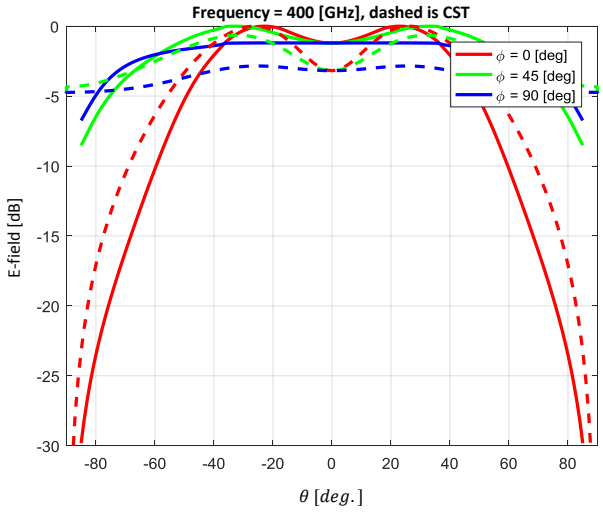

Figure E.4: Comparison between the integral equations and CST (the dashed lines) for the far field of a single slot with $F_{\#} = 0.6$; $w_s = 20\ \mu m$; $\delta = 15\ \mu m$ and $Z_l = 100\ \Omega$ using the stratification from appendix A.2.

E.2 Single Slot

The verification is done using CST [24] for a single slot structure with parameters: $F_{\#} = 0.6$; $w_s = 20\ \mu m$; $\delta = 10\ \mu m$ and $Z_l = 100\ \Omega$ using the stratification from appendix A.2 are show in Fig. E.4, E.5 and E.6 for respectively the far field, the active input impedance and the mutual coupling. For this simulation only one row of pixel is considered.

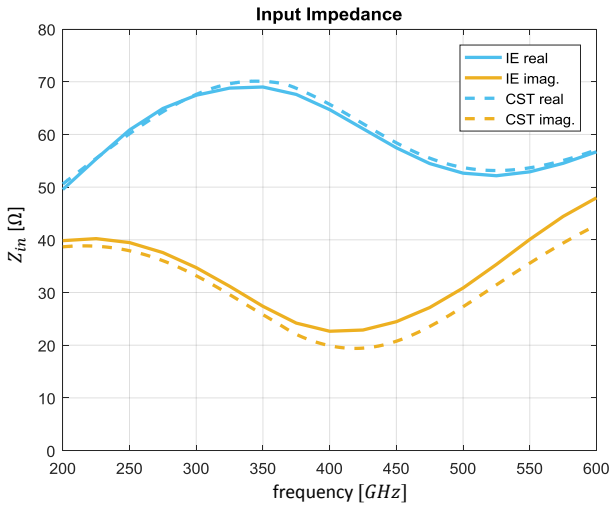

Figure E.5: Comparison between the integral equations and CST (the dashed lines) for the active input impedance of a single slot with $F_{\#} = 0.6$; $w_s = 20\ \mu m$; $\delta = 15\ \mu m$ and $Z_l = 100\ \Omega$ using the stratification from appendix A.2.

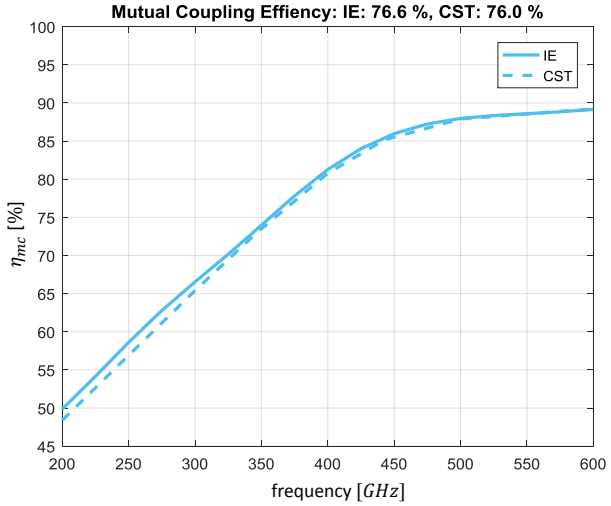

Figure E.6: Comparison between the integral equations and CST (the dashed lines) for the mutual coupling efficiency of a single slot with $F_{\#} = 0.6$; $w_s = 20\ \mu m$; $\delta = 15\ \mu m$ and $Z_l = 100\ \Omega$ using the stratification from appendix A.2.

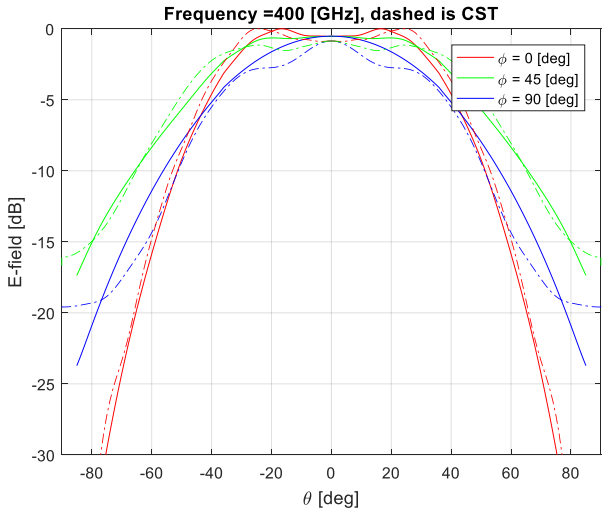

Figure E.7: Comparison between the integral equations and CST (the dashed lines) for the far field of a double slot with $F_{\#} = 1.5$; $w_s = 20\ \mu m$; $\delta = 10\ \mu m$; $d_\delta = d_s = 100\ \mu m$ and $Z_l = 100\Omega$ using the stratification from appendix A.2.

E.3 Double Slot

The verification is done using CST [24] for a double slot structure with parameters: $F_{\#} = 1.5$; $w_s = 20\ \mu m$; $\delta = 10\ \mu m$; $d_\delta = d_s = 100\ \mu m$ and $Z_l = 100\ \Omega$ using the stratification from appendix A.2 are show in Fig. E.7, E.8 and E.9 for respectively the far field, the active input impedance and the mutual coupling. For this simulation only one row of pixel is considered.

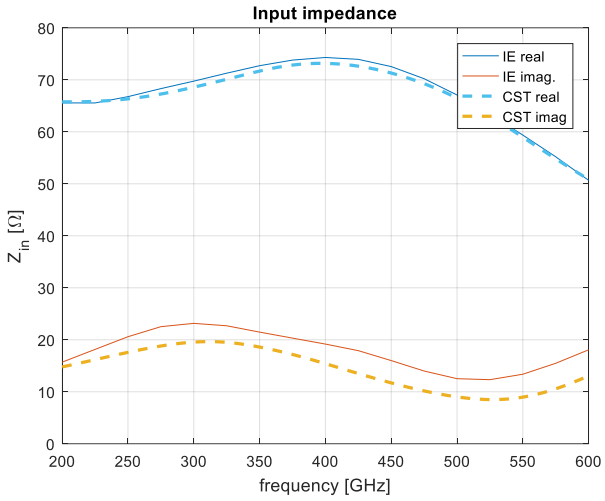

Figure E.8: Comparison between the integral equations and CST (the dashed lines) for the active input impedance of a double slot with $F_{\#} = 1.5$; $w_s = 20\ \mu m$; $\delta = 10\ \mu m$; $d_\delta = d_s = 100\ \mu m$ and $Z_l = 100\ \Omega$ using the stratification from appendix A.2.

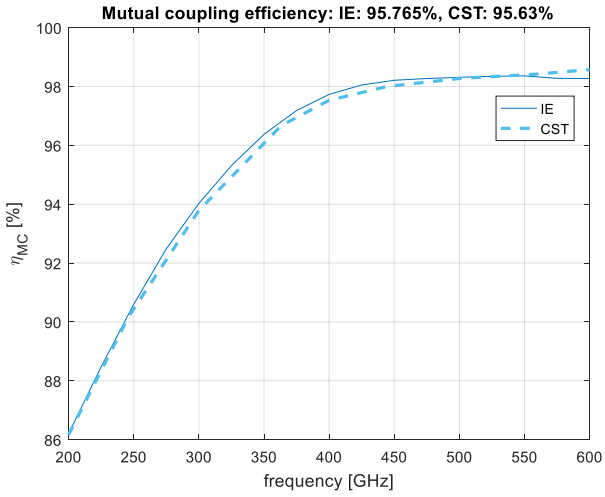

Figure E.9: Comparison between the integral equations and CST (the dashed lines) for the mutual coupling efficiency of a double slot with $F_{\#} = 1.5$; $w_s = 20\ \mu m$; $\delta = 10\ \mu m$; $d_\delta = d_s = 100\ \mu m$ and $Z_l = 100\ \Omega$ using the stratification from appendix A.2.

Bibliography

[1] J. Ziegler et al., "Making Bertha DriveAn Autonomous Journey on a Historic Route," in IEEE Intelligent Transportation Systems Magazine, vol. 6, no. 2, pp. 8-20, Summer 2014.

[2] P. A. Ioannou and C. C. Chien, "Autonomous intelligent cruise control", in IEEE Transactions on Vehicular Technology, vol. 42, no. 4, pp. 657-672, Nov 1993.

[3] M. Lu, K. Wevers and R. Van Der Heijden, "Technical feasibility of advanced driver assistance systems (ADAS) for road traffic safety," Transportation Planning and Technology, 28(3), pp.167-187, 2005.

[4] D.J. Fagnant, K. Kockelman. "Preparing a nation for autonomous vehicles: opportunities, barriers and policy recommendations," Transportation Research Part A: Policy and Practice, Elsevier, 77, pp.167-181, 2015.

[5] Rodrigo Benenson, Mohamed Omran, Jan Hendrik Hosang, and Bernt Schiele. "Ten years of pedestrian detection, what have we learned?," CoRR, abs/1411.4304, 2014.

[6] D. Geronimo, A. M. Lopez, A. D. Sappa and T. Graf, "Survey of Pedestrian Detection for Advanced Driver Assistance Systems," in IEEE Transactions on Pattern Analysis and Machine Intelligence, vol. 32, no. 7, pp. 1239-1258, July 2010.

[7] D. Belgiovane and C. C. Chen, "Micro-Doppler characteristics of pedestrians and bicycles for automotive radar sensors at 77 GHz," 2017 11th European Conference on Antennas and Propagation (EUCAP), Paris, 2017, pp. 2912-2916.

[8] Y. Luo, J. Remillard and D. Hoetzer, "Pedestrian detection in near-infrared night vision system," 2010 IEEE Intelligent Vehicles Symposium, San Diego, CA, 2010, pp. 51-58.

[9] U. Meis, M. Oberlander and W. Ritter, "Reinforcing the reliability of pedestrian detection in far-infrared sensing," IEEE Intelligent Vehicles Symposium, 2004, 2004, pp. 779-783.

[10] S. Nedevschi, S. Bota and C. Tomiuc, "Stereo-Based Pedestrian Detection for Collision-Avoidance Applications," in IEEE Transactions on Intelligent Transportation Systems, vol. 10, no. 3, pp. 380-391, Sept. 2009.

[11] D. M. Gavrila, "Sensor-based pedestrian protection," in IEEE Intelligent Systems, vol. 16, no. 6, pp. 77-81, Nov-Dec 2001.

[12] G. A. Siles, J. M. Riera and P. Garcia-del-Pino, "Atmospheric Attenuation in Wireless Communication Systems at Millimeter and THz Frequencies," in IEEE Antennas and Propagation Magazine, vol. 57, no. 1, pp. 48-61, Feb. 2015.

[13] A. Luukanen, R. Appleby, M. Kemp and N. Salmon, "Millimeter-wave and terahertz imaging in security applications," in Terahertz Spectroscopy and Imaging (pp. 491-520). Springer, Berlin, Heidelberg, 2012.

[14] B. Ferguson and X.C. Zhang, "Materials for terahertz science and technology,", Nature materials, 1(1), p.26, 2002.

[15] G. Chattopadhyay, "Technology, Capabilities, and Performance of Low Power Terahertz Sources," in IEEE Transactions on Terahertz Science and Technology, vol. 1, no. 1, pp. 33-53, Sept. 2011.

[16] R. Al Hadi et al., "A 1 k-Pixel Video Camera for 0.71.1 Terahertz Imaging Applications in 65-nm CMOS," in IEEE Journal of Solid-State Circuits, vol. 47, no. 12, pp. 2999-3012, Dec. 2012.

[17] S. L. van Berkel, O. Yurduseven, A. Freni, A. Neto and N. Llombart, "THz Imaging Using Uncooled Wideband Direct Detection Focal Plane Arrays," in IEEE Transactions on Terahertz Science and Technology, vol. 7, no. 5, pp. 481-492, Sept. 2017.

[18] A. Timofeev et al., "Optical and Electrical Characterization of a Large Kinetic Inductance Bolometer Focal Plane Array," in IEEE Transactions on Terahertz Science and Technology, vol. 7, no. 2, pp. 218-224, March 2017.

[19] Y. Kurita, G. Ducournau, D. Coquillat, A. Satou, K. Kobayashi, S. Boubanga Tombet, Y.M. Meziani, V.V. Popov, W. Knap, T. Suemitsu and T. Otsuji, "Ultrahigh sensitive sub-terahertz detection by InP-based asymmetric dual-grating-gate high-electron-mobility transistors and their broadband characteristics," Applied Physics Letters, 104(25), p.251114, 2014.

[20] J. J. A. Baselmans, et al. "A kilo-pixel imaging system for future space based far-infrared observatories using microwave kinetic inductance detectors," Astronomy & Astrophysics, 601, p.A89, 2017.

[21] M. Planck, *The theory of heat radiation.* Courier Corporation, 2013.

[22] M. J. Griffin, J. J. Bock, and W. K. Gear, "Relative performance of filled and feedhorn-coupled focal-plane architectures," *Applied Optics*, vol. 41, no. 31, pp. 6543-6554, 2002.

[23] G. Rieke, *Detection of Light: from the Ultraviolet to the Submillimeter.* Cambridge University Press, 2003.

[24] CST Computer Simulation Technology AG, CST microwave studio - 3d em simulation software, 2016. [Online]. Available: `https://www.cst.com/products/cstmws`.

[25] W. K. Kahn, "Ideal efficiency of a radiating element in an infinite array," *IEEE Trans. Antennas Propag.*, vol. AP-15, no. 4, Jul. 1967.

[26] J. F. Johansson, "Millimeter-wave imaging theory and experiments," Onsala Space Observatory, Onsala, Sweden, Res. Rep. no. 151, 1986.

[27] W. S. Holland, E. I. Robson, W. K. Gear, C. R. Cunningham, J. F. Lightfoot, T. Jenness, R. J. Ivison et al. "SCUBA: a commonuser submillimeter camera operating on the James Clerk Maxwell Telescope." Monthly Notices of the Royal Astronomical Society 303, no. 4 : 659-672, 1999.

[28] S.L. van Berkel, E. S. Malotaux, D. Cavallo, M. Spirito, A. Neto and N. Llombart, "Wideband Single Pixel Radiometer in 28nm CMOS Technology for Low-Cost Imaging Applications", EUCAP Conference Proceedings, 2018.

[29] S.L. van Berkel, E. S. Malotaux, D. Cavallo, M. Spirito, A. Neto and N. Llombart, "Wideband single pixel radiometer in CMOS", IRMMW-THz Conference Proceedings, 2017.

[30] A. D. Semenov et al., "Terahertz Performance of Integrated Lens Antennas With a Hot-Electron Bolometer," in IEEE Transactions on Microwave Theory and Techniques, vol. 55, no. 2, pp. 239-247, Feb. 2007.

[31] J. M. Edwards, R. O'Brient, A. T. Lee and G. M. Rebeiz, "Dual-Polarized Sinuous Antennas on Extended Hemispherical Silicon Lenses," in IEEE Transactions on Antennas and Propagation, vol. 60, no. 9, pp. 4082-4091, Sept. 2012.

[32] O. Yurduseven, N. Llombart Juan and A. Neto, "A Dual-Polarized Leaky Lens Antenna for Wideband Focal Plane Arrays," in IEEE Transactions on Antennas and Propagation," vol. 64, no. 8, pp. 3330-3337, Aug. 2016.

[33] O. Yurduseven, D. Cavallo, A. Neto, G. Carluccio and M. Albani, "Parametric analysis of extended hemispherical dielectric lenses fed by a broadband connected array of leaky-wave slots," in IET Microwaves, Antennas & Propagation, vol. 9, no. 7, pp. 611-617, 5 15 2015.

[34] A. Neto, "UWB, Non Dispersive Radiation From the Planarly Fed Leaky Lens Antenna Part 1: Theory and Design," in IEEE Transactions on Antennas and Propagation, vol. 58, no. 7, pp. 2238-2247, July 2010.

[35] G. C. Trichopoulos, H. L. Mosbacker, D. Burdette and K. Sertel, "A Broadband Focal Plane Array Camera for Real-time THz Imaging Applications," in IEEE Transactions on Antennas and Propagation, vol. 61, no. 4, pp. 1733-1740, April 2013.

[36] A. J. Alazemi, H. H. Yang and G. M. Rebeiz, "Double Bow-Tie Slot Antennas for Wideband Millimeter-Wave and Terahertz Applications," in IEEE Transactions on Terahertz Science and Technology, vol. 6, no. 5, pp. 682-689, Sept. 2016.

[37] R.C. Hansen, "Linear connected arrays [coupled dipole arrays],"in IEEE Antennas and Wireless Propagation Letters, vol. 3, pp. 154-156, 2004.

[38] D. Cavallo, A. Neto and G. Gerini, "PCB Slot Based Transformers to Avoid Common-Mode Resonances in Connected Arrays of Dipoles," in IEEE Transactions on Antennas and Propagation, vol. 58, no. 8, pp. 2767-2771, Aug. 2010.

[39] D. Cavallo, A. Neto and G. Gerini, "Green's Function Based Equivalent Circuits for Connected Arrays in Transmission and in Reception," in IEEE Transactions on Antennas and Propagation, vol. 59, no. 5, pp. 1535-1545, May 2011.

[40] D. Cavallo, W. H. Syed and A. Neto, "Connected-Slot Array With Artificial Dielectrics: A 6 to 15 GHz Dual-Pol Wide-Scan Prototype," in IEEE Transactions on Antennas and Propagation, vol. 66, no. 6, pp. 3201-3206, June 2018.

[41] O. Yurduseven, D. Cavallo and A. Neto, "Wideband Dielectric Lens Antenna With Stable Radiation Patterns Fed by Coherent Array of Connected Leaky Slots," in IEEE Transactions on Antennas and Propagation, vol. 62, no. 4, pp. 1895-1902, April 2014.

[42] D. Cavallo and A. Neto, "A Connected Array of Slots Supporting Broadband Leaky Waves," in IEEE Transactions on Antennas and Propagation, vol. 61, no. 4, pp. 1986-1994, April 2013.

[43] L. Felsen, and N. Marcuvitz, "Radiation and scattering of waves". IEEE PRESS, 1994.